

Syracuse University

SURFACE at Syracuse University

Dissertations - ALL

SURFACE at Syracuse University

Summer 7-16-2021

Optical Printing of Multiscale Hydrogel Structures

Zheng Xiong

Syracuse University

Follow this and additional works at: <https://surface.syr.edu/etd>



Part of the [Biomedical Engineering and Bioengineering Commons](#)

Recommended Citation

Xiong, Zheng, "Optical Printing of Multiscale Hydrogel Structures" (2021). *Dissertations - ALL*. 1373.
<https://surface.syr.edu/etd/1373>

This Dissertation is brought to you for free and open access by the SURFACE at Syracuse University at SURFACE at Syracuse University. It has been accepted for inclusion in Dissertations - ALL by an authorized administrator of SURFACE at Syracuse University. For more information, please contact surface@syr.edu.

Abstract

Hydrogel has been a promising candidate to recapitulate the chemical, physical and mechanical properties of natural extracellular matrix (ECM), and they have been widely used for tissue engineering, lab on a chip and biophotonics applications. A range of optical fabrication technologies such as photolithography, digital projection stereolithography and laser direct writing have been used to shape hydrogels into structurally complex functional devices and constructs. However, it is still greatly challenging for researchers to design and fabricate multiscale hydrogel structures using a single fabrication technology.

To address this challenge, the goal of this work is the design and develop novel multimode optical 3D printing technology capable of printing hydrogels with multiscale features ranging from centimeter to micrometer sizes and in the process transforming simple hydrogels into functional devices for many biomedical applications. Chapter 2 presents a new multimode optical printing technology that synergistically combined large-scale additive manufacturing with small-scale additive/subtractive manufacturing. This multiscale fabrication capability was used to (i) align cells using laser induced densification in Chapter 3, (ii) develop diffractive optics based on changes in refractive indices in Chapter 4, (iii) print diffractive optical elements in Chapter 5, and (iv) digitally print complex microfluidic devices and other 3D constructs in Chapter 6. Overall, this work open doors to a new world of fabrication where multiscale functional hydrogel structures are possible for a range biomedical application.

OPTICAL PRINTING OF MULTISCALE HYDROGEL STRUCTURES

By

ZHENG XIONG

B.S., Changchun University of Science and Technology, 2011

M.S., University of Chinese Academy of Sciences, 2016

DISSERTATION

Submitted in partial fulfillment of the requirements for the degree of Doctor of

Philosophy in Bioengineering

Syracuse University

July 2021

Copyright © Zheng Xiong 2021

All Rights Reserved

Acknowledgements

First and foremost, I would like to extend the utmost gratitude to my advisor, Dr. Pranav Soman, for his fully support and guidance over past 5 years. It has been an enjoyable journey to work with him throughout the entire time at Syracuse and to innovate what I believe the unique 3D printing technologies in the world. He has been not only an advisor on training me with academic thinking, but a great friend on communicating with me about life. I would also like to thank Dr. Soman for providing me the great opportunity as the PI on NSF-SBIR grant to leading a cross-functional team for commercializing our 3D printing technology.

I would extend special appreciation to Dr. Puskal Kunwar who serves as my mentor introducing me into ultrafast laser field and took endless hours to develop my personal and professional skills. I also thank members of the Soman lab that have become not only my coworkers, but also my closest friends. Specifically, Alex Filip, Haiyan Li, Zhe Zhang, Yin Zhu, Kairui Zhang, Rafael Ramos, Griffin Smith, Arun Poudel, Zachary Geffert, John Collins, Dr. Stephen Sawyer, Dr. Ameya Narkar, thank you for the patience to discuss with me so that make failed experiments getting back smoothly. I would like to acknowledge Alex Filip and Kairui Zhang for selflessly assisting the lab whenever in need.

I would next like to thank the dissertation committee members, Dr. Zhao Qin, Dr. Zhen Ma, Dr. Heidi Hehnly, Dr. Alison Patteson, Dr. Samuel Herberg, Dr. Mary Beth Monroe, and Dr. Era Jain for spending the time to review my PhD work and provide valuable feedback on my dissertation. To all the behind-the-scenes personnel, Lynore de la Rosa, Karen Low, Eric

Finkelstein, Amy Forbes, and Jason Markle, thank you for organizing everything that keeps our department and labs running.

I would also like to acknowledge all my friends, both past and in present, in Syracuse Biomaterials Institute, Syracuse University, Syracuse Chinese Christian Church, and Chinese American Friendship Association. My PhD program cannot be successful without your support as a second home in Syracuse.

Lastly, I want to show deeply grateful to my family. Mom and dad, thank you very much for all the support throughout my academic journey. To my lovely wife, Cuixia, your patience, kindness, and support have saved my sanity throughout this process. This has been a dream goal through my life. Appreciate your selflessly scarification on your career and choosing to be with me through the whole journey. Thank you for bringing me lovely boy William. Thank you for coming to my life with never-ending happiness. I cannot love you more.

Table of Contents

Acknowledgements	iv
Table of Contents	vi
List of Figures.....	xi
List of Table	xxvi
CHAPTER 1: Introduction	1
1.1 Hydrogels.....	1
1.2 Fabrication of Multiscale Hydrogel Structures.....	2
1.2.1 Fabrication via Photolithography.....	2
1.2.2 Fabrication via Digital Projection Stereolithography	4
1.2.3 Fabrication via Laser Direct Writing	7
1.3 Scope of the Dissertation	9
1.4 References.....	11
CHAPTER 2: Hybrid laser printing of three-dimensional, multiscale, multi-material hydrogel structures	24
2.1 Abstract	24
2.2 Introduction.....	26
2.3 Design of hybrid laser printer	28

2.4. Additive/subtractive mode of Hybrid laser printer	30
2.5 Additive/additive mode of Hybrid laser printer	41
2.6 Multi-material printing mode of Hybrid laser printer.....	43
2.7. Discussion.....	48
2.7.1. Comparison of HLP with existing fabrication techniques	48
2.7.2. Comparison of HLP with existing laser based hybrid methods.....	49
2.7.3. HLP can fabricate hollow micro-features at any depth within a 3D structure.....	50
2.7.4. HLP as compared to current light-based multi-scale fabrication methods	50
2.7.5. HLP as compared to current light based multi-material fabrication methods	51
2.8 Conclusion	53
2.9. Experimental Section	53
2.10 Supporting Information.....	58
2.11 References	63
 CHAPTER 3: Femtosecond laser induced densification within cell-laden hydrogels	
results in cellular alignment	68
3.1 Abstract	68
3.2 Introduction.....	69
3.3 Materials and Methods.....	70

3.3.1 Synthesis of GelMA, LAP photoinitiator, and prepolymer preparation.	70
3.3.2 Characterization of mechanical properties of GelMA constructs.	71
3.3.3 Cell culture.....	72
3.3.4 Femtosecond laser writing setup.....	74
3.3.5 Fs-laser modifications within cell-laden GelMA.....	75
3.3.6 Quantification of cellular viability and alignment	76
3.4 Results.....	77
3.4.1 Laser induced material modifications within partially crosslinked GelMA.	77
3.4.2 Influence of fs-laser induced densification on cell behavior.	80
3.4.3 Design flexibility of densification induced cell alignment method.....	84
3.5 Discussion.....	91
3.6 Conclusion	94
3.7 Supplemental Information	95
3.8 References.....	98
 CHAPTER 4 : Embedded diffractive volume grating by femtosecond laser induced	
densification.....	105
4.1 Abstract	105
4.2 Introduction.....	106

4.3 Methods.....	107
4.4 Results and Discussion	109
4.5 Conclusion	118
4.6 References.....	119
CHAPTER 5: Hydrogel-based diffractive optical elements (hDOEs) using rapid digital photopatterning.....	124
5.1 Abstract	124
5.2 Introduction.....	126
5.3.Results.....	128
5.3.1 Digital projection photolithography setup	128
5.3.2 Design of DOEs using simulated computer-generated holography.....	129
5.3.3 Optical and mechanical characterization of PEGDA.....	131
5.3.4 Diffraction grating	132
5.3.5 Dammann grating (Beam Splitter).....	135
5.3.6 Fresnel zone plate	137
5.3.7 Fork-shaped grating	140
5.3.8 Computer generated hologram (CGH) of arbitrary user-defined pattern	142
5.3.9 Robustness characterization of the printed hDOEs	144

5.4. Discussion	146
5.5. Conclusion	149
5.6. Experimental Section	150
5.7 Supporting Information.....	154
5.8. References.....	164
CHAPTER 6 : Fabrication of multiscale hydrogel constructs using multiscale DMD-SLA/HLP technology	173
6.1 Abstract	173
6.2 Introduction.....	174
6.3 Multiscale stereolithography System.....	176
6.4 3D Microfluidic Chips	178
6.5 References.....	182
CHAPTER 7: Dissertation Summary	185
VITA.....	187

List of Figures

Figure 1.1 (a) Process flow of photolithography; (b) Micrographs of PEGDA hydrogel cell culture scaffold. (i) SEM image of high-density square-shape cell culture microwells with $30 \times 30 \mu\text{m}$; (ii) SEM image of high-density microcylinder with diameter $50 \mu\text{m}$. (c) SEM images of various microstructures on silk hydrogel that can show diffraction color at the macroscale. (i) $2 \mu\text{m}$ lines; (ii) $5 \mu\text{m}$ posts; (iii) $10 \mu\text{m}$ squares. Scale bar: $10 \mu\text{m}$. Reproduced from with permission from literatures [34,39,40,44].

Figure 1.2 (a) Schematic of a digital projection stereolithography system: (1) Ultraviolet (UV) light shines on the (2) DMD chip, which generates user-defined light pattern according to the (3) image flowing from computer. The light pattern is then projected through the (4) projection lens and imaged on the photopolymerizable hydrogels to fabricate 3D structures layer by layer manner using (5) motorized stage. (b) SEM images of (i) convex features (domes, wells etc.); (ii) 3D log-piles model and (iii) confocal fluorescence image of cell penetration. (c) Printed microfluidics devices. (i) SEM image of first printed micromixer using digital projection stereolithography; (ii) gradient generator; (iii) high-density dilution mixer pumps. Reproduced from with permission from literatures [72,74,75,78,81].

Figure 1.3 (a) Schematic of a single-photon laser direct writing setup. (b) Fabricated multilayer hydrogel cellular culture scaffold. (c) Schematic of a two-photon laser writing setup. (d) Fabricated (i) NPR and PPR hydrogel structures and (ii) time resolved cellular studies. (e) SEM

image of (i) fabricated hydrogel based diffractive micro-optics and (ii) imaging robustness under various PH solution. Reproduced from with permission from literatures [21,51,88,92,93].

Figure 1.4 Scope of the dissertation.

Figure 2.1. (A) Schematic of femtosecond laser-based additive-subtractive/additive-additive HLP machine. [FS-femtosecond laser, SHG-second harmonic generator, I-isolator, BS-beam splitter, P-polarizer, HWP-half waveplate, SHT-shutter, L-lens, PH-pin hole, FM-mirror in a flip mount, D-diffuser, DMD-digital micromirror device, DM- dichroic mirror, CM-camera, OL-objective, S-sample, SH-sample holder, ST-stage, TF-Teflon film]. Small dashed box: Schematic showing sample holder (SH) with teflon film (TF) and elevating stage (ST). Enlarged dashed box: Process flow of HLP showing one sequence of additive crosslinking and subtractive ablation steps.

Figure 2.2. (A) Schematic showing key parameters in HLP. Ablation z-range and dead-zone are two key parameters, which are highlighted in the figure by curly bracket. Please note that the additive and subtractive processes are sequential processes, although they are depicted in the same figure for simplicity. (B) Plot of dead-zone thickness as the function of exposure time and laser power. As for an instance, PEGDA slab crosslinked using crosslinking laser power of (P_{add}) of 150 mW and exposure time (t_{add}) of 20 s (marked by black arrow) results in dead-zone of 30 μm . (C) Schematic cartoon showing lines ablated at different penetration depths and plot of ablated linewidth as a function of laser penetration depths and laser powers. Results shows a decreasing linewidth trend with increasing laser penetration depth. Red marks in the

plot represent the upper limit of ablation z-range. (D) Plot of ablated linewidth as a function of scanning speeds and laser powers. Plot shows a decreasing linewidth trend with decreasing laser dose. For all of the studies in this figure, 90% PEGDA and 1% LAP was used as material for fabrication.

Figure 2.3. (A) Diagram showing slicing of an stl model of Mayan pyramid to create a stack of digital masks. (B) Key steps in the HLP process to print a Mayan pyramid with embedded cube frame. Iteration of additive and subtractive steps are involved to print a complete ‘cube inside pyramid’ structure (C) Side, top and isometric views of ‘cube inside pyramid’ structure in 90% PEGDA, 1% LAP and the image is recorded by an HIROX digital optical microscope. For additive step laser power of 200 mW and laser wavelength of 400 nm was used, while laser power of 1200 mW, scanning speed of 100 μ m/s and laser wavelength of 800 nm was used for subtractive steps. The height of the pyramid is 6 mm. The cube is 600 μ m³, embedded 2 mm from the bottom of the pyramid. (red arrow points to the embedded cube).

Figure 2.4. Printing user-defined two-well PEGDA chips with interconnecting in-plane and out-of-plane microchannels. (A) In-plane channels: side and top views of channels with zig-zag and square-wave configurations are depicted. Perfusion of Rhodamine B through zig-zag channels is demonstrated. (B) Out-of-plane channels: Side, isometric and top views of 3D channels spanning multiple crosslinked layers are depicted. White dotted box highlights the zig-zag ablated channels. For all of the studies in this figure, 10% PEGDA and 1% LAP was used for fabricating the structures.

Figure 2.5. (A) Brightfield image of a 4-well PEGDA chips with inter-well microchannels is depicted. Fluorescent images showing actin (green) and nucleus (blue). MLO-Y4 cells seeded in neighboring wells communicate with each other by extending cell processes within the ablated channels. White arrows point the communication channels with a diameter of 5 μm (B) Brightfield image of a 4-well PEGDA chips with inter-well microchannels is depicted. Seeded osteosarcoma Saos-2 cells migrate within the ablated channels. White arrows show the migration channels with a diameter of 7 μm . For all the studies in this figure, 10% PEGDA and 1% LAP was used for fabricating the open-well chips.

Figure 2.6. HLP's capability of additive-additive multiscale printing (A) Schematic depicting sequential additive steps of DMD based printing (CLIP) and multiphoton polymerization (MPP). Three woodpile structures were printed in different depth using MPP. (B) Corresponding DMD masks and wood pile structures. (C) HIROX digital optical microscopy image depicting three woodpile structures fabricated at different z-planes and xy spatial locations. Three different woodpile structure marked by 1, 2 and 3 correspond to the zoomed images to the left. Structure was printed using 10% PEGDA and 1% LAP with laser power of 200 mW and exposure time of 5 seconds in additive CLIP step. While high resolution MPP fabrication was performed using laser power of 400 mW and scanning speed of 100 $\mu\text{m/s}$.

Figure 2.7. (A) Syringe pump system for multiscale, multimaterial fabrication. Three different inlets and three outlets were used for exchange of printing material. Nitrogen/water inlets and two water outlets were meant for washing and drying steps. (B) Side view of the fluid chamber, which depicts 5 inlets/5 outlets and fabrication area. Cross-section view (at marked green

dotted line) shows the sloped floor design that facilitates easy exchange of prepolymer solutions during printing.

Figure 2.8. (A) Schematic depicting digital mask and multicolored Mayan pyramid fabricated using multimaterial additive printing of three colored 90% PEGDA, 1% LAP prepolymer solutions. (B) Ying and yang structure printed using four different colored 90% PEGDA, 1% LAP. (C) Multiscale printing of multimaterial structure using two commonly used hydrogel (GelMA and PEGDA). The outer thick wall colored in pink is printed with 15% GELMA, 0.5% LAP using DMD based fabrication. Similarly, the DMD based approach is used to print intersecting lines using 50% PEGDA, 1% LAP. Further logpile structure shown inside the black square box is printed using MPP based DLW approach using 90% PEGDA, 1% LAP. (D) Additive and subtractive multimaterial approach of fabrication is demonstrated using 90% PEGDA, 0.5% LAP (colored in green) and 50% PEGDA, 0.5% LAP (colored in red). Insets shows the zoomed version of ablated lines using MPA.

Figure S2.1. Photographs showing the sample holder and stage used in Hybrid laser printing.

Figure S2.2. A) Four well microfluidic chips fabricated in 10% GelMA and 0.25% LAP using HLP. Rectangular wells were printed using a crosslinking laser wavelength (λ_{add}) of 365 nm, crosslinking laser power (P_{add}) of 200 mW and exposure time (t_{add}) of 25 s. In subtractive mode of HLP, ablation wavelength(λ_{sub}) of 730 nm, ablation laser power (P_{sub}) of 1000 mW and

scanning speed (v_{sub}) of 100 $\mu\text{m/s}$ was used. Image was recorded using HIROX microscope.

B) Optical microscopy image of wall between the wells with embedded microchannels.

Figure S2.3. Imaging of woodpile structure fabricated at different depth (at the interval of 200 μm) of the three dimensional multiscale structure. A) Woodpile structure 1 is at focus, whereas woodpile structure 2 and 3 are out of focus B) Woodpile structure 2 is at focus and woodpile structure 1 and 3 are out of focus C) Woodpile structure 3 is at focus and wood pile structure 1 and 2 are out of focus.

Figure S2.4. Plot depicting the linewidth of the ablated features, which are shown in the Figure 2.7D. A laser power of the 1300 mW was kept constant and the scanning speed was varied from the 50 $\mu\text{m/s}$ to 150 $\mu\text{m/s}$ to ablate feature in 90% PEGDA, 0.5% LAP (marked in green) and 50% PEGDA, 0.5% LAP (marked in red).

Figure 3.1. (A) The schematic of process flow of femtosecond (fs) laser writing and associated material modifications within partially crosslinked gelatin methacrylate (GelMA). With increasing laser dosage, partially crosslinked GelMA go from densification to ablation to unstable regimes. (B) Brightfield and fluorescence images (top views and cross-section views) of fs-laser written features at the center of GelMA construct. (i, iv, vi, viii) represent densification, while (ii, v, vii, ix) represent ablation and (iii) represents unstable bubble formation. (C) Material modification phase diagram of modification width vs laser dosage for different UV exposure times (from 5-60s). (D) Relationship between laser penetration depth and modified line width.

Figure 3.2. (A) Schematic of experimental design; cell-laden GelMA was partially crosslinked using a UV exposure time of 5s, followed by laser writing of densified line patterns at the center of the samples. (B) Characterization of cell viability 24hrs after fabrication using a live (green)-dead (red) assay. (Line spacing-50 μ m, dashed white lines) (C) Fluorescence images showing nuclei (blue) and actin (green) morphology of HUVECs around un-patterned and patterned regions on (i) Day 1, (ii) Day 3 and (iii) Day 5. (D) Plot of nuclear alignment vs days in culture for patterned regions for a line spacing of 50 μ m. (D) Plot of nuclear shape index vs days in culture for patterned regions for line spacing of 50 μ m. (Scale bar: 100 μ m) (Error bars: Mean \pm SD; *** $p < 0.001$; ** $p < 0.01$; * $p < 0.05$) Controls shows un-patterned results on Day 5.

Figure 3.3. (A) Fluorescence images showing nuclei (blue) morphology and actin (green) morphology of HUVECs around patterned regions for a lined spacing of 50, 100 and 200 μ m on Day 5. Controls shows un-patterned results on Day 5 (B) Quantification of changes in nuclear alignment as a function of line spacing on Day 5. (C) Quantification of changes in shape index as a function of line spacing on Day 5. (Scale bar: 100 μ m) (Error bars: Mean \pm SD; *** $p < 0.001$; ** $p < 0.01$; * $p < 0.05$)

Figure 3.4. (A) Fluorescence images showing morphology of mouse IDG-SW3 osteoblasts, mouse C3H-10T1/2 fibroblasts, and hiPSCs-MSCs around un-patterned (control) and patterned regions on Day 5. (B) Characterization of changes in nuclear alignment between un-patterned and patterned regions for all cell types (line spacing=50 μ m; Day 5). Dashed square: IDG-SW3 were encapsulated on Day 0, cultured for 24 hrs, before introducing densified line patterns on Day 1, and immunostaining was performed on Day 5. For all other cells, densified lines were

written on Day 0, and immunostaining was performed on Day 5. (C) Plot of nuclear shape index of different cell types for a pattern spacing of 50 μ m. (Scale bar: 100 μ m) (Error bars: Mean \pm SD; *** $p < 0.001$; ** $p < 0.01$; * $p < 0.05$)

Figure 3.5. (A) Schematic of the 0° and 90° line pattern design and representative brightfield (i) and fluorescence images (ii) showing alignment of 10T1/2 cells in the vicinity of patterns (line spacing=50 μ m; Day 5). (B) Plots of (i) nuclear alignment and (ii) nuclear shape index for cells in the vicinity of patterns within 10T1/2-laden GelMA as compared to cells from the un-patterned regions. (C) Representative brightfield (i) and fluorescence image (ii) showing cellular alignment around user-defined concentric-circle patterns (spacing=50 μ m; Day 5) within 10T1/2-laden GelMA. (Scale bar: 100 μ m) (Error bars: Mean \pm SD; *** $p < 0.001$; ** $p < 0.01$; * $p < 0.05$)

Figure 3.6. (A) Schematic and representative fluorescence images captured at different z-planes within 10T1/2-laden GelMA. (B) Schematic of a line patterns written in two distinct layers. Fluorescence images from (i) layer 1 (80 μ m from the top surface), and (ii, iii) layer 2 (160 μ m from the top surface). (iv) Plot shows differences in nuclei alignment between layers 1 and 2 from un-patterned and patterned regions. (Error bars: Mean \pm SD; *** $p < 0.001$; ** $p < 0.01$)

Figure SI-3.1: The experimental setup was integrating the femtosecond laser with an inverted microscope. The inset shown the steps of laser modification including (1) cell-laden prepolymer (2) partially crosslinking (3) laser processing.

Figure SI-3.2 (A) Real-time changes in storage modulus for GelMA samples with varying UV exposure times, and (B) elastic modulus of partially crosslinking GelMA samples (UV time=2.5s, 5s, 10s, 20s, and 40s) and fully crosslinked GelMA samples (60s) after one day of incubation in DI water.

Figure SI-3.3 Absorption spectrum of GelMA prepolymer mixed with LAP photoinitiator.

Figure SI-3.4 Quantification of nuclei alignment after additions of CytoD (inhibitor of actin dynamics), at different time points during active cell culture. (A)-(i) D0-D3: CytoD was added on Day 0, and image was obtained on Day 3, (A)-(ii) D3-D6: CytoD was added on Day 3 and image was obtained on Day 6. (B) Plots of nuclear alignment after addition of actin dynamics inhibitor. (C) Nuclear shape index after addition of actin dynamics inhibitor, CytoD. (Scale bar: 100 μ m) (Error bars: Mean \pm SD; *** p<0.001; ** p<0.01)

Figure SI-3.5 Complex user-defined patterns can be densified within GelMA samples.

Figure SI-3.6 (A) Cellular alignment within 7% GelMA and (B) 10% GelMA under the same UV irradiation time of 30s (Scale bar: 50 μ m)

Figure 4.1 Characterization of PEGDA hydrogels with different concentration. (A) Optical transparency and (B) absorption spectrum in visible spectrum. (C) Refractive index. The refractive index is increased from 1.35 to 1.48 with the concentration increasing of hydrogel. (D) Mechanical stability. With increasing concentration, the elastic modulus and the swelling ratio is increased, while no changes in the optical transparency.

Figure 4.2 (A) Schematic of femtosecond laser processing and (B) associated material modification within (i) partially crosslinked PEGDA hydrogel. With increasing laser dosage, the partially crosslinked hydrogel goes from (ii) densification to (iii) ablation. (C) The phase contrast images (top-view) of the fs-laser written features inside the PEGDA hydrogel. Material modification phase diagram of line width versus laser dosage under different (D) fabrication speed and (E) laser power.

Figure 4.3 (A) Schematic of fs laser 3D writing inside hydrogel. n is the refractive index of hydrogels. Δn is the refractive index change due to laser induced densification. (B) Sketch of grating diffracting using He-Ne laser beam of 632.8 nm. Phase contrast images of diffraction grating at (C) top view and (D) side view. (E) Optical photograph of grating's diffraction pattern. (F) Intensity ratio between 0th diffraction order and 1st diffraction order and theoretical calculation of corresponding refractive index change. Scale bar 10 μ m

Figure 4.4 Different diffraction gratings including (A) 2D linear grating (B) square grating and (C) circular grating are fabricated inside hydrogel by laser induced densification. The bright field illustrates clear microfeatures within partially crosslinked hydrogel. The confocal images of diffraction elements using Rhodamine B staining presents the density difference of the embedded microstructures. The optical photograph of the patterns captured at far field shows the diffraction property of these microstructures. Scale bar: 50 μ m

Figure 5.1. Schematic of digital projection photolithography setup that consists of illumination optics, DMD, beam splitter, projection lens, CMOS camera and sample mount. The digital

mask for customized diffractive optics, generated using MATLAB algorithm (Section 2.2), was fed to the DMD to generate virtual digital mask for UV light modulation via the DMD. Inset shows the setup for hydrogel film; Prepolymer solution is sandwiched between methacrylated coverslip and silanized microscope slide with PDMS spacer for thickness control.

Figure 5.2. Generic process flow to generate customized digital mask based on defined inputs.

Here, 1D diffraction grating is chosen as a case study.

Figure 5.3. Optical and mechanical characteristics of PEGDA hydrogels with varying prepolymer concentrations. (A) Optical transmission spectrum of PEGDA hydrogels. Inset shows photographs of PEGDA hydrogels in cuvette. (B) Refractive indices (RI) of crosslinked (solid) and uncrosslinked (dashed) PEGDA. (C) Elastic modulus of crosslinked PEGDA samples.

Figure 5.4. Photo-patterning of 1D and 2D diffraction/transmission grating and characterization of their optical properties. (A) Designed patterns. The fabricated grating microstructures were characterized using bright-field microscopy (B), phase contrast microscopy (C) and SEM (D). (E) 2D views of grating diffraction pattern using 632.8 nm He-Ne laser at normal incidence illumination. Scale bar for A-D: 50 μm .

Figure 5.5. Photo-patterning of PEGDA DG device and its optical characterization. (A) Designed mask pattern of 5×5 DG. The fabricated structure was characterized using bright-field microscopy (B) and phase contrast microscopy (C). (D) SEM image shows the close-up

view of the micro-structure. (E) Beam splitting performance and intensity cross-section (dotted lines in E) of individual beams along X and Y axis (F). Scale bar A-D: 20 μm .

Figure 5.6. Photo-patterning of FZP in PEGDA and characterization of its optical properties.

(A) Designed digital mask of FZP. Images of FZP fabricated from PEGDA were obtained using bright-field microscopy (B) and SEM (C). (D) Image of light focusing by FZP using He-Ne laser. (E) Intensity cross section of focal spot along X direction (dashed line in D). (F) Imaging performance of FZP using a capital letter ‘H’. (G) Theoretical and experimental results of primary and secondary focusing lengths. Inset shows the imaging performance for different focus lengths. Scale bar: 100 μm .

Figure 5.7. Photo-patterning of fork grating and characterization of its optical properties. (A)

Generation of digital mask of fork grating by simulating the interference between the optical beams carrying vortex phase and a tilted plane wave. The fabricated fork grating was characterized using bright-field (B) and phase contrast microscopy (C). (D) SEM image. (E) Optical characterization of diffraction pattern (0^{th} and 1^{st} diffraction orders) of fork grating using He-Ne laser. (F) Donut beam of fork grating at the focus and (G) its cross-section of intensity profile in X direction. Scale bar A-D and F: 100 μm .

Figure 5.8. Photo-patterning of CGH in PEGDA and characterization of its optical properties.

(A) Desired reconstructed pattern of ‘Syracuse University (SU) Logo’. (B) Generation of digital mask of CGH using the GS algorithm. The CGH of SU logo is interfered with the tilted plane wave to obtain the digital mask for DMD. The fabricated CGH samples were

characterized using bright field (C), phase contrast microscopy (D), and SEM (E). (F) The reconstructed diffraction pattern of CGH using He-Ne laser. Scale bar C-E: 20 μm .

Figure S5.1 Setup to test the optical performance of hDOEs using He-Ne laser. The diffractive optical element was directly illuminated by coherent laser source. An imaging screen was used to capture the diffraction patterns.

Figure S5.2 Setup to test imaging performance of hDOEs under bright-field microscope. The target, letter 'H', was illuminated by bright-field illumination source and imaged by diffractive optics, Fresnel Zone Plate. The image was captured by a CCD camera with objective. A filter was used to block non-visible spectrum.

Figure S5.3 Schematic of 1D grating mask design based on two beams holographic interference.

Figure S5.4 Schematic of 2D grating design.

Figure S5.5 One period of transmission function of 1D binary DG.

Figure S5.6 Schematic of mask design of 2D DG.

Figure S5.7 Schematic of mask design of FZP based on the interference between spherical and plane waves.

Figure S5.8 Schematic of mask design of FG based on the interferences between wave with spiral phase and plane waves.

Figure S5.9 Schematic of mask design of CGH based on the interference between Fourier pattern of object and plane wave.

Figure S5.10 Testing the effect of water evaporation on ‘as printed’ Damman grating DOEs

Figure S5.11 Testing the robustness of the Dammann grating DOEs under repeated dehydration and rehydration processes

Figure S5.12 Testing the durability of the Dammann grating DOEs under femtosecond laser irradiation (Wavelength: 800nm, Pulse duration: 140fs, Repetition rate: 80MHz, Power: 1W).

Figure 6.1 Multiscale microstereolithography module. The novel multiscale system, which consists of multiscale light engine, resin vat and Z stage, upgrades CLIP in original HLP system with higher resolution down to 10 μm and fast/largescale fabrication.

Figure 6.2 Printed 3D models (Mayan pyramid and Empire building). (A) 3D CAD models are printed using multiscale system and (B) imaged under digital microscope and (C) under SEM.

Figure 6.3 Printed 3D microfluidic models (square and spiral channel). (A) 3D CAD models are printed using multiscale system and (B) imaged under digital microscope. Green and red dye flowing inside the microchannels. Scale bar: 500 μm .

Figure 6.4 Printed 3D microfluidic chips (microchannel and Alveoli). (A) 3D CAD models are printed using multiscale system and (B) imaged under digital microscope. Green and red dye flowing inside the microchannels.

Figure 6.5 Printed 3D microfluidic insert. (A) 3D CAD models are printed using multiscale system and (B) imaged under digital microscope.

List of Table

Table S2.1. HLP can print centimeter-scale 3D structures with micrometer resolution and high design flexibility (FDM-Fused Deposition Modeling; MJM-Multijet modeling; SLA-Stereolithography; DMD-Digital Micromirror Device; CLIP-Continuous liquid interface production; MPP-Multi-photon polymerization; MPA-Multi-photon ablation).

CHAPTER 1: Introduction

1.1 Hydrogels

Hydrogels consists of three-dimensional hydrophilic polymer networks, which can be cross-linked through physical or chemical reactions [1]. Typically, physically cross-linked hydrogels are formed by non-covalent bonding, while chemically cross-linked hydrogels are polymerized by free radical initiated via thermal or photo radiation. Hydrogels have been demonstrated as a suitable materials family to recapitulate the natural extracellular matrix (ECM) found in biological tissues and organs due to their ability to tune their chemical, physical and biological properties [2–8]. This makes them a promising material for many applications such as implantable artificial muscles, cell scaffolds [9], and tissue organs [10,11], although shaping hydrogels into complex multiscale functional structures remains a difficult challenge in the field. Most tissues within the human body, such as articular cartilage [12], muscle [13], and skin [14], have well-defined hierarchical and anisotropic structures spanning in size from nanometer to centimeters. This biological complexity is difficult to recapitulate using hydrogels, which are typically soft and homogenous [15]. Design of new functional hydrogels with features at sub-cellular or cellular sizes have also been demonstrated to modulate fundamental cellular behavior such as cell adhesion, alignment, proliferation, spreading and differentiation [16–21]. Moreover, new areas of research such as biophotonics, microfluidics and lab-on-a-chip (LOC) [22–32] also require new methods to process hydrogels into multiscale functional components, which is currently challenging.. For instance, although basic optical functions such as focusing, reflection and diffraction have been realized using hydrogel materials

[23,26,33–36], more work needs to be done to develop optically-functional hydrogel devices. Additionally, as compared to conventional PDMS microfluidic devices, hydrogel microfluidic devices exhibit better properties such as low-protein adsorption, easy methods to functionalize biomolecules, and in-situ biosensing capabilities; this could form the basis for next-generational multi-functional devices [24,37]. Here we review some key strategies to fabricate multiscale functional hydrogels for some common applications such as scaffolds for cell culture and single cell biology, and optical and microfluidic devices.

1.2 Fabrication of Multiscale Hydrogel Structures

1.2.1 Fabrication via Photolithography

Photolithography has been successfully used to pattern hydrogel structures [26,38–43]. As a widely used microfabrication technology, this technique is regularly used for polymers and hydrogels with photosensitive groups (e.g. acrylate). In a typical process flow, [38], the prepolymer solution is spin-coated on a substrate (glass or silicon) followed by selective UV exposure using a physical mask to generate micro-/nano-patterns. The polymers at the exposed regions are crosslinked, while the unexposed regions are washed away by a developer solution (Fig. 1.1a). Figure 1.1b shows representative examples of microstructures made using Poly (ethylene glycol) diacrylate (PEGDA) hydrogel using this method. User-defined hydrogel structures including spheres, cylinders and cubes can be created by changing the shape/pattern of the photomask [41]. For instance, Bryant et al. used multiple photomasks and generated porous poly (HEMA) hydrogel scaffold [44]. The shape or size of the pores could be changed

based on the design of the photomask, and such multilayer hydrogel microstructures can be used for cell culture [45]. Ramendra et al. presented photolithography to achieve microstructures made out of silk proteins, fibroin and sericin for hydrogels with optical properties [34]. By photolithography, silk protein photoresists are fabricated in periodic 2D patterns (Fig. 1.1c). The iridescent colors are generated in these periodic patterns from Bragg diffraction. The photolithography of silk proteins can be utilized to produce custom patterns on various substrates including flexible sheets over large areas.

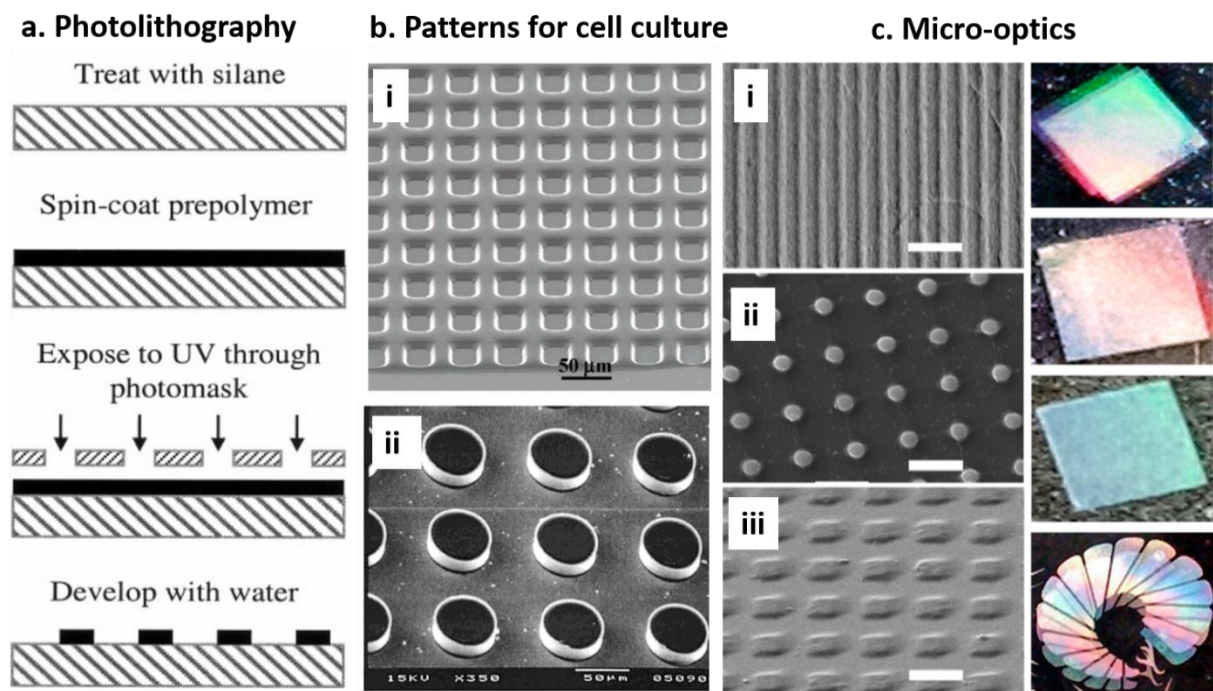


Figure 1.1 (a) Process flow of photolithography; (b) Micrographs of PEGDA hydrogel cell culture scaffold. (i) SEM image of high-density square-shape cell culture microwells with $30 \times 30 \mu\text{m}$; (ii) SEM image of high-density microcylinder with diameter $50 \mu\text{m}$. (c) SEM images of various microstructures on silk hydrogel that can show diffracted colors at the

macroscale. (i) 2 μm lines; (ii) 5 μm posts; (iii) 10 μm squares. Scale bar: 10 μm . Reproduced from with permission from literatures [34,40,41,45].

One limitation of this technique is the inability to generate 3D structures or patterns. To fabricate 3D hydrogel structures, advanced photolithographic techniques such as “digital projection stereolithography or SLA” [25,27,46–49] and “direct laser writing” [23,47,50,51] have been developed, as described in the subsequent sections.

1.2.2 Fabrication via Digital Projection Stereolithography

Digital projection stereolithography (SLA), also called projection printing, is a 3D printing technology, which uses a digital micro-mirror device or a digital mask (DMD, Texas Instruments Inc.) instead of the physical mask used in conventional photolithography [25,27,42,43,52–68]. The system shown in Fig. 1.2a is one type of the projection printing system [46,64,69–74]. In this setup, the uniform UV illumination is spatially modulated by a DMD chip to generate customized patterns. The DMD consists of an array of aluminum micromirrors, capable of directing light by tilting with two angles of either $+12^\circ$ or -12° , which corresponds to two states: “on” or “off”. The modulated light pattern passes through the projection lens and then is transferred onto a prepolymer solution inside the vat. To fabricate 3D hydrogel structures, a 3D computer-aided design (CAD) model is sliced into a series of digital masks which are projected sequentially on the DMD. DMD-modulated light patterns are used to crosslink the photopolymer in a layer-by-layer fashion by lowering the Z stage. By

tuning key process parameters such as the stage velocity, light intensity, and layer-height, the system can generate customized hydrogel structures, such as spiral domes, microwells and pyramids (Fig. 1.2b-i). Figure 1.2b-ii presents a 3D structure with hexagonal geometry made using gelatin methacrylate (GelMA) hydrogel [75]. Figure 1.2b-iii shows cells migrating and proliferating within a GelMA (10%v/v) scaffold. This method has been used by many groups to generate customized cellular scaffolds with tunable mechanical properties by modulating the prepolymer concentration and the internal design or geometry.

Another application of SLA is the printing of microfluidic devices using a biocompatible and transparent hydrogel. This method involves additive crosslinking of a microchannel followed by removal unreacted polymer from the channel. Figure 1.2 c presents the capability of SLA in fabricating a range of microfluidic devices capable of (i) such as superior mixing by splitting, combing, and rearranging the flowlines [76] (Fig. 1.2c-i), immunomagnetic separation of cells or bacteria by using helical channels [77,78], and generating precise gradient of solutions [79] (Fig. 1.2c-ii), emulsion droplet generators [79–81], a dilution mixer pump for DNA analysis [37] (Fig. 1.2c-iii) and an insert for oxygen control for a 24-well dish, etc. [82].

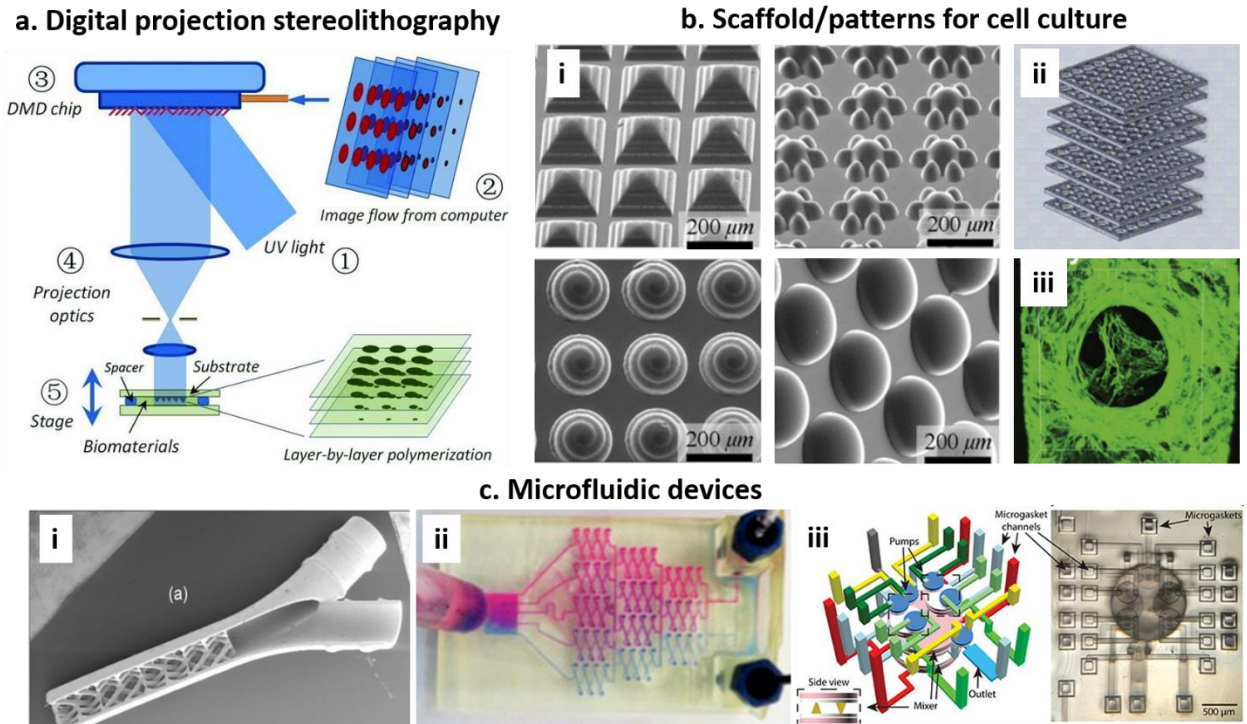


Figure 1.2 (a) Schematic of a digital projection SLA system: (1) Ultraviolet (UV) light shines on the (2) DMD chip, which generates user-defined light pattern according to the (3) image flowing from computer. The light pattern is then projected through the (4) projection lens and imaged on the photopolymerizable hydrogels to fabricate 3D structures layer by layer manner using (5) motorized stage. (b) SEM images of (i) convex features (domes, wells etc.); (ii) 3D log-piles model and (iii) confocal fluorescence image of cell penetration. (c) Printed microfluidics devices. (i) SEM image of first printed micromixer using digital projection SLA; (ii) gradient generator; (iii) high-density dilution mixer pumps. Reproduced from with permission from literatures [37,73,75,76,79].

These examples demonstrate the versatility of digital projection SLA for fabricating customized 3D hydrogel structures with various features and mechanical properties. However,

the resolution of enclosed channels is limited to few 100 micrometers with commonly used SLA or DMD-SLA systems. With the use of customized optics and optimized resin properties, few researchers have demonstrated a channel resolution of $\sim 20\ \mu\text{m}$, although channels below $10\ \mu\text{m}$ has been challenging with this method.

1.2.3 Fabrication via Laser Direct Writing

The high-resolution printing and processing capabilities of laser-based direct writing [47,48,83–86] has been used to shape hydrogels in user-defined 3D shapes. Generally, a 3D model is converted into a series of 2D layers, and each layer is made up of a point matrix. The laser direct-writing system, according to these point coordinates, serially scans the laser beam using an XYZ stage and fabricates these 3D structures (Fig.1.3a) [52,87] [88–90]. In this method, focused laser beam penetrates the liquid hydrogel and polymerizes it into a solid gel. The feature size can be controlled by the exposure energy and the scanning speed. After the first layer of point matrix is printed, the motorized stage is moved down, and a new layer of hydrogel is solidified or crosslinked based on the design of point matrix in the second layer. Regularly, laser 3D printing systems use a focused UV laser to induce single-photon polymerization of hydrogels [87]. Chan et al. employed this for fabricating 3D hydrogel structures to assess cell viability and culture a heterogeneous cell distribution long term (Fig. 1.3b-i). Mapili et al. demonstrated a multilayer cellular culture scaffold using a PEGDA hydrogel functionalized with heparin or RGD-peptide sequences introduced within the hydrogel to facilitate cell adhesion (Fig. 1.3b-ii) [91].

Two-photon or multiphoton processing (TPP or MPP) is another type of laser based direct-writing technology. A near-infrared (NIR) femtosecond laser beam is tightly focused within hydrogel and induces nonlinear two-photon or multiphoton absorption (Fig. 1.3c). Compared to the single photon process, TPP can achieve polymerization in a smaller region. In one study, TPP was used to investigate the interaction of single cell with ‘movable’ topographic features that are unattached to the underlying substrate. Zhang et al. showed that cell proliferation, orientation, and motility vary between ‘movable’ negative (NPR) or positive Poisson's ratio (PPR) constructs (Fig. 1.3d-i) [17]. between negative (Fig. 1.3d-ii). In another application, Sun et al. reported using TPP to fabricate soft diffractive micro-optics using bovine serum albumin hydrogel as the building block [23]. This novel diffractive optics demonstrates distinctive optical properties under varying pH conditions and the ability to have flexible or stretchable properties. (Fig. 1.3e)

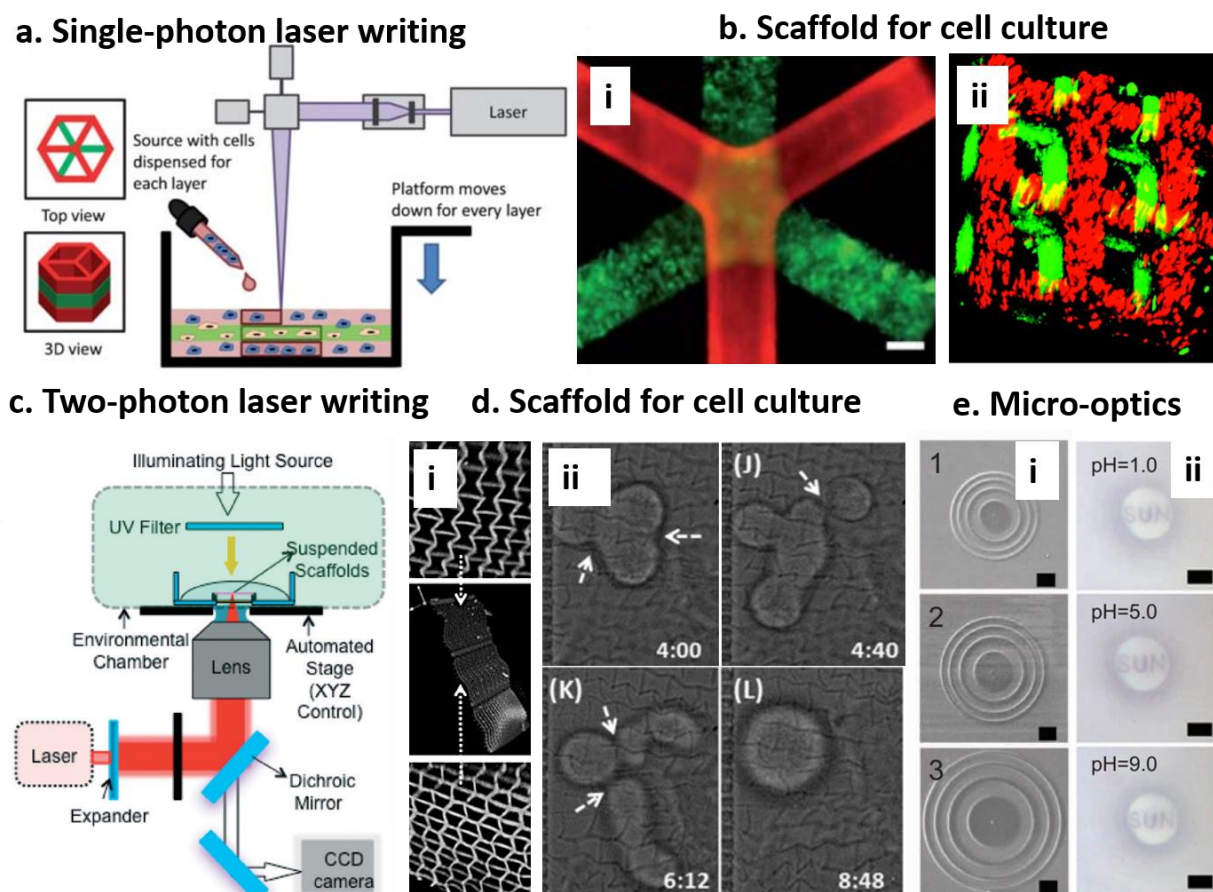


Figure 1.3 (a) Schematic of a single-photon laser direct writing setup. (b) Fabricated multilayer hydrogel cellular culture scaffold. (c) Schematic of a two-photon laser writing setup. (d) Fabricated (i) NPR and PPR hydrogel structures and (ii) time resolved cellular studies. (e) SEM image of (i) fabricated hydrogel based diffractive micro-optics and (ii) imaging robustness under various PH solution. Reproduced from with permission from literatures [17,23,52,87,91].

1.3 Scope of the Dissertation

Current fabrication technology is limited in terms of printing resolution, range and design flexibility. This is an even greater fabrication challenge when it comes to shaping soft hydrogels

into functional constructs or devices towards target biomedical applications. Thus, the overarching goal of this work is to develop new technologies capable of printing multiscale 3D hydrogel structures with superior design flexibilities and continue to utilize the unique properties of hydrogel materials for applications in tissue engineering, biophotonics, and microfluidics.

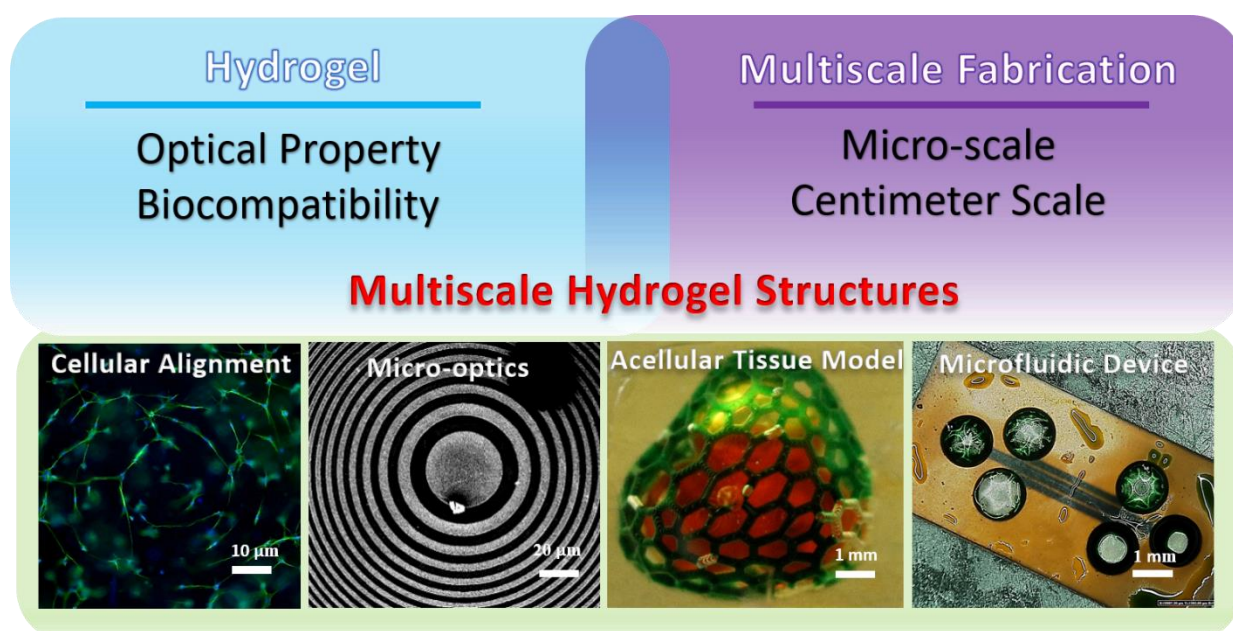


Figure 1.4 Scope of the dissertation

This introduction, Chapter 1, set the background about various optics based micromanufacturing technologies. Chapter 2 will describe the design and development of a new technology coined as hybrid laser printing technology (HLP) and its capability to achieve multiscale and multi-material hydrogel structures. Chapter's 3 and 4 will describe the discovery of a new phenomenon coined as 'laser induced densification', and its applications with cell-laden hydrogels and diffractive optical devices. Chapter 5 will describe the design and development of a new digital patterning methods by using custom holographic elements

generated from computer-generated. Chapter 6 will discuss ongoing work related to a new multiscale DMD-SLA platform capable of rapidly printing multiscale hydrogel structures. Lastly, chapter 7 will summarize the work presented in this dissertation.

1.4 References

- [1] Gong J P 2006 Friction and lubrication of hydrogels—its richness and complexity *Soft Matter* **2** 544–52
- [2] Xia L-W, Xie R, Ju X-J, Wang W, Chen Q and Chu L-Y 2013 Nano-structured smart hydrogels with rapid response and high elasticity *Nat. Commun.* **4** 1–11
- [3] Sun T L, Kurokawa T, Kuroda S, Ihsan A Bin, Akasaki T, Sato K, Haque M A, Nakajima T and Gong J P 2013 Physical hydrogels composed of polyampholytes demonstrate high toughness and viscoelasticity *Nat. Mater.* **12** 932–7
- [4] Peppas N A and Langer R 1994 New challenges in biomaterials *Science (80-.).* **263** 1715–20
- [5] Osada Y, Okuzaki H and Hori H 1992 A polymer gel with electrically driven motility *Nature* **355** 242–4
- [6] Chen G and Hoffman A S 1995 Graft copolymers that exhibit temperature-induced phase transitions over a wide range of pH *Nature* **373** 49–52
- [7] Campbell M, Sharp D N, Harrison M T, Denning R G and Turberfield A J 2000 Fabrication of photonic crystals for the visible spectrum by holographic lithography

- [8] Rowley J A, Madlambayan G and Mooney D J 1999 Alginate hydrogels as synthetic extracellular matrix materials *Biomaterials* **20** 45–53
- [9] Kaneko D, Gong J P and Osada Y 2002 Polymer gels as soft and wet chemomechanical systems—an approach to artificial muscles *J. Mater. Chem.* **12** 2169–77
- [10] Langer R and Vacanti J P 1993 Tissue engineering *Science (80-.)*. **260** 920–6
- [11] Stock U A and Vacanti J P 2001 Tissue engineering: current state and prospects *Annu. Rev. Med.* **52** 443–51
- [12] Ng K W, Wang C C, Mauck R L, Kelly T N, Chahine N O, Costa K D, Ateshian G A and Hung C T 2005 A layered agarose approach to fabricate depth-dependent inhomogeneity in chondrocyte-seeded constructs *J. Orthop. Res.* **23** 134–41
- [13] Annaidh A N, Bruyère K, Destrade M, Gilchrist M D and Otténio M 2012 Characterization of the anisotropic mechanical properties of excised human skin *J. Mech. Behav. Biomed. Mater.* **5** 139–48
- [14] Johnson M, Polgar J, Weightman D and Appleton D 1973 Data on the distribution of fibre types in thirty-six human muscles: an autopsy study *J. Neurol. Sci.* **18** 111–29
- [15] Elisseeff J 2008 Structure starts to gel *Nat. Mater.* **7** 271–3
- [16] Tsang V L and Bhatia S N 2004 Three-dimensional tissue fabrication *Adv. Drug Deliv. Rev.* **56** 1635–47

- [17] Zhang W, Soman P, Meggs K, Qu X and Chen S 2013 Tuning the poisson's ratio of biomaterials for investigating cellular response *Adv. Funct. Mater.* **23** 3226–32
- [18] El-Sherbiny I M and Yacoub M H 2013 Hydrogel scaffolds for tissue engineering: Progress and challenges *Glob. Cardiol. Sci. Pract.* **2013** 38
- [19] Sanchez-Dealcazar D, Romera D, Castro-Smirnov J, Sousaraei A, Casado S, Espasa A, Morant-Miñana M C, Hernandez J J, Rodríguez I, Costa R D, Cabanillas-Gonzalez J, Martinez R V. and Cortajarena A L 2019 Engineered protein-based functional nanopatterned materials for bio-optical devices *Nanoscale Adv.* **1** 3980–91
- [20] Binan L, Ajji A, De Crescenzo G and Jolicoeur M 2014 Approaches for neural tissue regeneration *Stem cell Rev. reports* **10** 44–59
- [21] Haggerty A E and Oudega M 2013 Biomaterials for spinal cord repair *Neurosci. Bull.* **29** 445–59
- [22] Choi M, Choi J W, Kim S, Nizamoglu S, Hahn S K and Yun S H 2013 Light-guiding hydrogels for cell-based sensing and optogenetic synthesis in vivo *Nat. Photonics* **7** 987–94
- [23] Sun Y L, Dong W F, Niu L G, Jiang T, Liu D X, Zhang L, Wang Y S, Chen Q D, Kim D P and Sun H B 2014 Protein-based soft micro-optics fabricated by femtosecond laser direct writing *Light Sci. Appl.* **3** e129–e129
- [24] Au A K, Huynh W, Horowitz L F and Folch A 2016 3D-printed microfluidics *Angew.*

- [25] Xiong Z, Kunwar P, Zhu Y, Filip A, Li H and Soman P 2020 Hybrid laser platform for printing 3D multiscale multi-material hydrogel structures (Conference Presentation) *Laser 3D Manufacturing VII* vol 11271 (International Society for Optics and Photonics) p 112710N
- [26] Xiong Z, Kunwar P and Soman P 2020 Hydrogel-Based Diffractive Optical Elements (hDOEs) Using Rapid Digital Photopatterning *Adv. Opt. Mater.* 2001217
- [27] Kunwar P, Xiong Z, Zhu Y, Li H, Filip A and Soman P 2019 Hybrid Laser Printing of 3D, Multiscale, Multimaterial Hydrogel Structures *Adv. Opt. Mater.* **7** 1900656
- [28] Au A K, Lee W and Folch A 2014 Mail-order microfluidics: evaluation of stereolithography for the production of microfluidic devices *Lab Chip* **14** 1294–301
- [29] Chen C, Mehl B T, Munshi A S, Townsend A D, Spence D M and Martin R S 2016 3D-printed microfluidic devices: fabrication, advantages and limitations—a mini review *Anal. Methods* **8** 6005–12
- [30] Qiu Y and Park K 2012 Environment-sensitive hydrogels for drug delivery *Adv. Drug Deliv. Rev.* **64** 49–60
- [31] Ho C M B, Ng S H, Li K H H and Yoon Y-J 2015 3D printed microfluidics for biological applications *Lab Chip* **15** 3627–37
- [32] Heintz K A, Bregenzer M E, Mantle J L, Lee K H, West J L and Slater J H 2016

- Fabrication of 3D Biomimetic Microfluidic Networks in Hydrogels *Adv. Healthc. Mater.* **5** 2153–60
- [33] Lawrence B D, Cronin-Golomb M, Georgakoudi I, Kaplan D L and Omenetto F G 2008 Bioactive silk protein biomaterial systems for optical devices *Biomacromolecules* **9** 1214–20
- [34] Pal R K, Kurland N E, Wang C, Kundu S C and Yadavalli V K 2015 Biopatterning of silk proteins for soft micro-optics *ACS Appl. Mater. Interfaces* **7** 8809–16
- [35] Choi M, Humar M, Kim S and Yun S H 2015 Step-Index Optical Fiber Made of Biocompatible Hydrogels *Adv. Mater.* **27** 4081–6
- [36] Shabahang S, Kim S and Yun S 2018 Light-guiding biomaterials for biomedical applications *Adv. Funct. Mater.* **28** 1706635
- [37] Gong H, Woolley A T and Nordin G P 2019 3D printed selectable dilution mixer pumps *Biomicrofluidics* **13** 14106
- [38] Revzin A, Tompkins R G and Toner M 2003 Surface engineering with poly (ethylene glycol) photolithography to create high-density cell arrays on glass *Langmuir* **19** 9855–62
- [39] Beebe D J, Moore J S, Bauer J M, Yu Q, Liu R H, Devadoss C and Jo B-H 2000 Functional hydrogel structures for autonomous flow control inside microfluidic channels *Nature* **404** 588–90

- [40] Bryant S J, Hauch K D and Ratner B D 2006 Spatial patterning of thick poly (2-hydroxyethyl methacrylate) hydrogels *Macromolecules* **39** 4395–9
- [41] Hahn M S, Taite L J, Moon J J, Rowland M C, Ruffino K A and West J L 2006 Photolithographic patterning of polyethylene glycol hydrogels *Biomaterials* **27** 2519–24
- [42] Xiong Z and Soman P 2021 Digital printing of hydrogel based diffractive optical elements *Advanced Fabrication Technologies for Micro/Nano Optics and Photonics XIV* vol 11696 (International Society for Optics and Photonics) p 116960X
- [43] Xiong Z, Kunwar P and Soman P 2021 Hydrogel-Based Diffractive Optical Elements (hDOEs) Using Rapid Digital Photopatterning *Adv. Opt. Mater.* **9** 2001217
- [44] Bryant S J, Cuy J L, Hauch K D and Ratner B D 2007 Photo-patterning of porous hydrogels for tissue engineering *Biomaterials* **28** 2978–86
- [45] Griffith L G and Naughton G 2002 Tissue engineering--current challenges and expanding opportunities *Science (80-.).* **295** 1009–14
- [46] Soman P, Chung P H, Zhang A P and Chen S 2013 Digital microfabrication of user-defined 3D microstructures in cell-laden hydrogels *Biotechnol. Bioeng.* **110** 3038–47
- [47] Xiong Z, Li H, Kunwar P, Zhu Y, Ramos R, McLoughlin S, Winston T, Ma Z and Soman P 2019 Femtosecond laser induced densification within cell-laden hydrogels results in cellular alignment *Biofabrication* **11** 35005

- [48] Xiong Z and Soman P 2020 User-defined and localized cellular alignment using femtosecond laser hydrogel densification *Frontiers in Ultrafast Optics: Biomedical, Scientific, and Industrial Applications XX* vol 11270 (International Society for Optics and Photonics) p 1127009
- [49] Hribar K C, Soman P, Warner J, Chung P and Chen S 2014 Light-assisted direct-write of 3D functional biomaterials *Lab Chip* **14** 268–75
- [50] Kaehr B and Shear J B 2008 Multiphoton fabrication of chemically responsive protein hydrogels for microactuation *Proc. Natl. Acad. Sci.* **105** 8850–4
- [51] Zhang W and Chen S 2011 Femtosecond laser nanofabrication of hydrogel biomaterial *MRS Bull.* **36** 1028–33
- [52] Waldbaur A, Rapp H, Länge K and Rapp B E 2011 Let there be chip—towards rapid prototyping of microfluidic devices: one-step manufacturing processes *Anal. Methods* **3** 2681–716
- [53] Lin H, Zhang D, Alexander P G, Yang G, Tan J, Cheng A W-M and Tuan R S 2013 Application of visible light-based projection stereolithography for live cell-scaffold fabrication with designed architecture *Biomaterials* **34** 331–9
- [54] Liska R, Schuster M, Inführ R, Turecek C, Fritscher C, Seidl B, Schmidt V, Kuna L, Haase A and Varga F 2007 Photopolymers for rapid prototyping *J. Coatings Technol. Res.* **4** 505–10

- [55] Han L-H, Mapili G, Chen S and Roy K 2008 Projection microfabrication of three-dimensional scaffolds for tissue engineering *J. Manuf. Sci. Eng.* **130**
- [56] Zhang Y, Luo J, Xiong Z, Liu H, Wang L, Gu Y, Lu Z, Li J and Huang J 2019 User-defined microstructures array fabricated by DMD based multistep lithography with dose modulation *Opt. Express* **27** 31956
- [57] Guo S, Lu Z, Xiong Z, Huang L, Liu H and Li J 2021 Lithographic pattern quality enhancement of DMD lithography with spatiotemporal modulated technology *Opt. Lett.* **46** 1377–80
- [58] Soman P, Kunwar P, Xiong Z, Zhu Y, Li H, Filip A and Ramos R 2019 Hybrid additive-subtractive laser fabrication platform for shaping hydrogels *42nd Society for Biomaterials Annual Meeting and Exposition 2019: The Pinnacle of Biomaterials Innovation and Excellence* (Society for Biomaterials)
- [59] Kunwar P, Xiong Z and Soman P 2021 Hybrid laser platform (HLP) for printing 3D multiscale multi-material hydrogel structures *Laser 3D Manufacturing VIII* vol 11677 (International Society for Optics and Photonics) p 116770T
- [60] Kunwar P, Xiong Z, McLoughlin S T and Soman P 2020 Oxygen-Permeable Films for Continuous Additive, Subtractive, and Hybrid Additive/Subtractive Manufacturing *3D Print. Addit. Manuf.* **7** 216–21
- [61] Xiong Z, Liu H, Tan X, Lu Z, Li C, Song L and Wang Z 2014 Diffraction analysis of

- digital micromirror device in maskless photolithography system *J. Micro/Nanolithography, MEMS, MOEMS* **13** 043016
- [62] Xiong Z, Liu H and Lu Z 2013 Diffraction Analysis of Digital Micromirror Device at Coherent Illumination *CIOMP-OSA Summer Session on Optical Engineering, Design and Manufacturing* (Optical Society of America) p Th14
- [63] Billiet T, Vandenhaute M, Schelfhout J, Van Vlierberghe S and Dubruel P 2012 A review of trends and limitations in hydrogel-rapid prototyping for tissue engineering *Biomaterials* **33** 6020–41
- [64] Lu Y, Mapili G, Suhali G, Chen S and Roy K 2006 A digital micro-mirror device-based system for the microfabrication of complex, spatially patterned tissue engineering scaffolds *J. Biomed. Mater. Res. - Part A* **77** 396–405
- [65] Choi J-W, Wicker R, Lee S-H, Choi K-H, Ha C-S and Chung I 2009 Fabrication of 3D biocompatible/biodegradable micro-scaffolds using dynamic mask projection microstereolithography *J. Mater. Process. Technol.* **209** 5494–503
- [66] Lantada A D and Morgado P L 2013 *Handbook on advanced design and manufacturing technologies for biomedical devices* (Springer)
- [67] Horn T J and Harrysson O L A 2012 Overview of current additive manufacturing technologies and selected applications *Sci. Prog.* **95** 255–82
- [68] Gittard S D and Narayan R J 2010 Laser direct writing of micro-and nano-scale medical

devices *Expert Rev. Med. Devices* **7** 343–56

- [69] Soman P, Lee J W, Phadke A, Varghese S and Chen S 2012 Spatial tuning of negative and positive Poisson's ratio in a multi-layer scaffold *Acta Biomater.* **8** 2587–94
- [70] Soman P, Fozdar D Y, Lee J W, Phadke A, Varghese S and Chen S 2012 A three-dimensional polymer scaffolding material exhibiting a zero Poisson's ratio *Soft Matter* **8** 4946–51
- [71] Soman P, Kelber J A, Lee J W, Wright T N, Vecchio K S, Klemke R L and Chen S 2012 Cancer cell migration within 3D layer-by-layer microfabricated photocrosslinked PEG scaffolds with tunable stiffness *Biomaterials* **33** 7064–70
- [72] Soman P, Tobe B T D, Lee J W, Winquist A A M, Singec I, Vecchio K S, Snyder E Y and Chen S 2012 Three-dimensional scaffolding to investigate neuronal derivatives of human embryonic stem cells *Biomed. Microdevices* **14** 829–38
- [73] Zhang A P, Qu X, Soman P, Hribar K C, Lee J W, Chen S and He S 2012 Rapid fabrication of complex 3D extracellular microenvironments by dynamic optical projection stereolithography *Adv. Mater.* **24** 4266–70
- [74] Fozdar D Y, Soman P, Lee J W, Han L and Chen S 2011 Three-dimensional polymer constructs exhibiting a tunable negative Poisson's ratio *Adv. Funct. Mater.* **21** 2712–20
- [75] Gauvin R, Chen Y-C, Lee J W, Soman P, Zorlutuna P, Nichol J W, Bae H, Chen S and Khademhosseini A 2012 Microfabrication of complex porous tissue engineering

- scaffolds using 3D projection stereolithography *Biomaterials* **33** 3824–34
- [76] Bertsch A, Heimgartner S, Cousseau P and Renaud P 2001 Static micromixers based on large-scale industrial mixer geometry *Lab Chip* **1** 56–60
- [77] Lee W, Kwon D, Choi W, Jung G Y, Au A K, Folch A and Jeon S 2015 3D-printed microfluidic device for the detection of pathogenic bacteria using size-based separation in helical channel with trapezoid cross-section *Sci. Rep.* **5** 1–7
- [78] Lee W, Kwon D, Chung B, Jung G Y, Au A, Folch A and Jeon S 2014 Ultrarapid detection of pathogenic bacteria using a 3D immunomagnetic flow assay *Anal. Chem.* **86** 6683–8
- [79] Shallan A I, Smejkal P, Corban M, Guijt R M and Breadmore M C 2014 Cost-effective three-dimensional printing of visibly transparent microchips within minutes *Anal. Chem.* **86** 3124–30
- [80] Zhang J M, Aguirre-Pablo A A, Li E Q, Buttner U and Thoroddsen S T 2016 Droplet generation in cross-flow for cost-effective 3D-printed “plug-and-play” microfluidic devices *RSC Adv.* **6** 81120–9
- [81] Kanai T and Tsuchiya M 2016 Microfluidic devices fabricated using stereolithography for preparation of monodisperse double emulsions *Chem. Eng. J.* **290** 400–4
- [82] Brennan M D, Rexius-Hall M L and Eddington D T 2015 A 3D-printed oxygen control insert for a 24-well plate *PLoS One* **10** e0137631

- [83] Odde D J and Renn M J 2000 Laser-guided direct writing of living cells *Biotechnol. Bioeng.* **67** 312–8
- [84] Koch L, Gruene M, Unger C and Chichkov B 2013 Laser assisted cell printing *Curr. Pharm. Biotechnol.* **14** 91–7
- [85] Wu P K, Ringeisen B R, Callahan J, Brooks M, Bubbs D M, Wu H D, Piqué A, Spargo B, McGill R A and Chrisey D B 2001 The deposition, structure, pattern deposition, and activity of biomaterial thin-films by matrix-assisted pulsed-laser evaporation (MAPLE) and MAPLE direct write *Thin Solid Films* **398** 607–14
- [86] Doraiswamy A, Narayan R J, Harris M L, Qadri S B, Modi R and Chrisey D B 2007 Laser microfabrication of hydroxyapatite-osteoblast-like cell composites *J. Biomed. Mater. Res. Part A* **80** 635–43
- [87] Chan V, Zorlutuna P, Jeong J H, Kong H and Bashir R 2010 Three-dimensional photopatterning of hydrogels using stereolithography for long-term cell encapsulation *Lab Chip* **10** 2062–70
- [88] Melchels F P W, Feijen J and Grijpma D W 2010 A review on stereolithography and its applications in biomedical engineering *Biomaterials* **31** 6121–30
- [89] Hutmacher D W, Sittertinger M and Risbud M V 2004 Scaffold-based tissue engineering: rationale for computer-aided design and solid free-form fabrication systems *TRENDS Biotechnol.* **22** 354–62

- [90] Ovsianikov A, Gruene M, Pflaum M, Koch L, Maiorana F, Wilhelmi M, Haverich A and Chichkov B 2010 Laser printing of cells into 3D scaffolds *Biofabrication* **2** 14104
- [91] Mapili G, Lu Y, Chen S and Roy K 2005 Laser-layered microfabrication of spatially patterned functionalized tissue-engineering scaffolds *J. Biomed. Mater. Res. Part B Appl. Biomater. An Off. J. Soc. Biomater. Japanese Soc. Biomater. Aust. Soc. Biomater. Korean Soc. Biomater.* **75** 414–24

CHAPTER 2: Hybrid laser printing of three-dimensional, multiscale, multi-material hydrogel structures *

2.1 Abstract

Fabrication of multiscale, multi-material three-dimensional (3D) structures at high resolution is difficult using current technologies. This is especially significant when working with hydrated and mechanically weak hydrogel materials. In this work, a new hybrid laser printing (HLP) technology is reported to print complex, multiscale, multimaterial, 3D hydrogel structures with microscale resolution. This technique of fabrication utilizes sequential additive and subtractive modes of material fabrication, that are typically considered as mutually exclusive due to differences in their material processing conditions. Further, compared to current laser writing systems that enforce stringent processing depth limits, HLP is shown to fabricate structures at any depth inside the material. As a proof-of-principle, a Mayan Pyramid with embedded cube-frame is printed using model synthetic polyethylene glycol diacrylate (PEGDA) hydrogel. Printing of ready-to-use open-well chips with embedded microchannels is also demonstrated using PEGDA and gelatin methacrylate (GelMA) hydrogels for potential applications in biomedical sciences. Next, HLP is used in additive and additive modes to print multiscale 3D structures spanning in size from centimeter to micrometers within minutes,

*Adapted from: P. Kunwar, Z. Xiong, Y. Zhu, H.Y. Li, A. Filip, P. Soman, Hybrid laser printing of 3D, multiscale, multimaterial hydrogel structures, *Advanced Optical Materials* 7 (21), 1900656 (2019)

*Reprinted as permitted by John Wiley & Sons, Inc. author agreement for personal use.

which is followed by printing of 3D, multi-material, multiscale structures using this technology. Overall, this work demonstrates that HLP's fabrication versatility can potentially offer a unique opportunity for a range of applications in optics and photonics, biomedical sciences, microfluidics, soft robotics, etc.

2.2 Introduction

Over the course of billions of years, nature has created and refined numerous elegant biosynthetic processes to make sophisticated functional structures. In contrast, current manufacturing techniques are still limited in their ability to fabricate 3D, multiscale, multi-material structures. New advances in fabrication methods are expected to revolutionize the development of next-generation devices for optics, photonics, microfluidics, soft robotics, flexible electronics, organ-on-a-chip and many other applications [1,2,3]. Already, the emergence of additive manufacturing methods such as extrusion-based fused deposition modeling (FDM), inkjet-based multiJet modeling (MJM), digital light processing (DLP) and stereolithography (SLA), have allowed the fabrication of structures and devices with high design flexibility, in a highly automated, assembly-free, and low cost manner [2,4]. A new version of DLP, coined as continuous liquid interface production (CLIP), is able to fabricate centimeter-sized polymeric constructs in a quick and continuous fashion [5]. However, these methods cannot fabricate structures with resolution below 25 μm . Multiphoton polymerization (MPP), often coined as direct laser writing, is an additive manufacturing method that allows the printing of complicated 3D structures at sub-micrometer resolution [6,7]. However, slow point-by-point scanning approach generally makes this method impractical for printing centimeter scale multiscale structures.

As compared to most of the additive methods discussed above, subtractive manufacturing methods based on lithography provide similar resolution for fabricating micro- and nano-scale

structures, but these methods are typically limited to planar or 2.5D structures [8]. Multiphoton ablation (MPA), a method that utilizes ultrafast lasers to remove material, can create embedded hollow micro-features such as channels, grooves in glass and polymer substrates [9,10]. Similar to MPP, MPA also suffers from low scalability and throughput due to the serial nature of fabrication. Additionally, the dependence of MPA on the optical transparency of the material, limits its penetration depth and overall design flexibility. Few research groups have utilized the ability of ultrafast lasers to process material in both additive (MPP) and subtractive (MPA) modes to develop a hybrid additive-subtractive method [10,11,12]. But, current laser-based hybrid methods are limited by scalability, types of specialized materials, and incompatible laser processing requirements, thereby preventing its widespread use in the field.

In this work, we report the design and development of a hybrid laser printing (HLP) technology, that combines the key advantages of CLIP process (quick on-demand continuous fabrication) and MPP and MPA processes (high-resolution and superior design flexibility). Using a series of proof-of-principle experiments, we show that HLP is capable of printing 3D, multiscale, multi-material structures using model biocompatible hydrogel materials that are highly difficult and/or extremely time consuming to fabricate using current technologies. We demonstrate the HLP versatility of printing in three different modes of fabrication: additive/subtractive, additive/additive and multimaterial modes and we foresee that HLP's fabrication capabilities can be applied to a broad range of applications.

2.3 Design of hybrid laser printer

HLP setup consists of a femtosecond laser source (Coherent, Ti:Sapphire), which is used in both additive and subtractive modes of fabrication. The additive crosslinking mode, indicated by solid blue arrows in Figure 2.1, is created by passing the fs-laser beam through a second harmonic generator (SHG) to obtain ultraviolet wavelengths and then spatially modulated via a digital micromirror device (DMD). DMD is an electronic board embedded with an array of micromirrors. Based on a user-defined image, DMD can selectively switch mirrors into either an ON state or an OFF state and create a light pattern that selectively crosslinks photosensitive prepolymer into 2D layers of a defined thickness. The subtractive ablation mode, indicated by the dashed red arrows in Figure 2.1, utilizes fs-laser beam directed via an objective lens to ablate voids within the previously crosslinked layer using MPA. Additionally, fs-laser can be also used in additive mode to polymerize 3D structures with microscale resolution using MPP. In this prototype, the additive mode can print $\sim 1 \text{ cm}^2$ feature in XY with smallest feature size of $30 \text{ }\mu\text{m}$, while the subtractive MPA mode can fully ablate features with a minimum feature size of $3 \text{ }\mu\text{m}$, based on the absorption properties of the hydrogel prepolymer. Figure 2.1 inset (big dashed box) shows the one sequence of the process flow of additive DMD crosslinking (CLIP) and subtractive MPA. Figure 2.1 inset (small dashed box) shows the schematic diagram of sample holder, stage and Teflon window. A detail description of the optical setup of HLP and a photograph and detail description of the sample holder and elevating stage is described in the Methods section and Supp. Info (Figure S2.1).

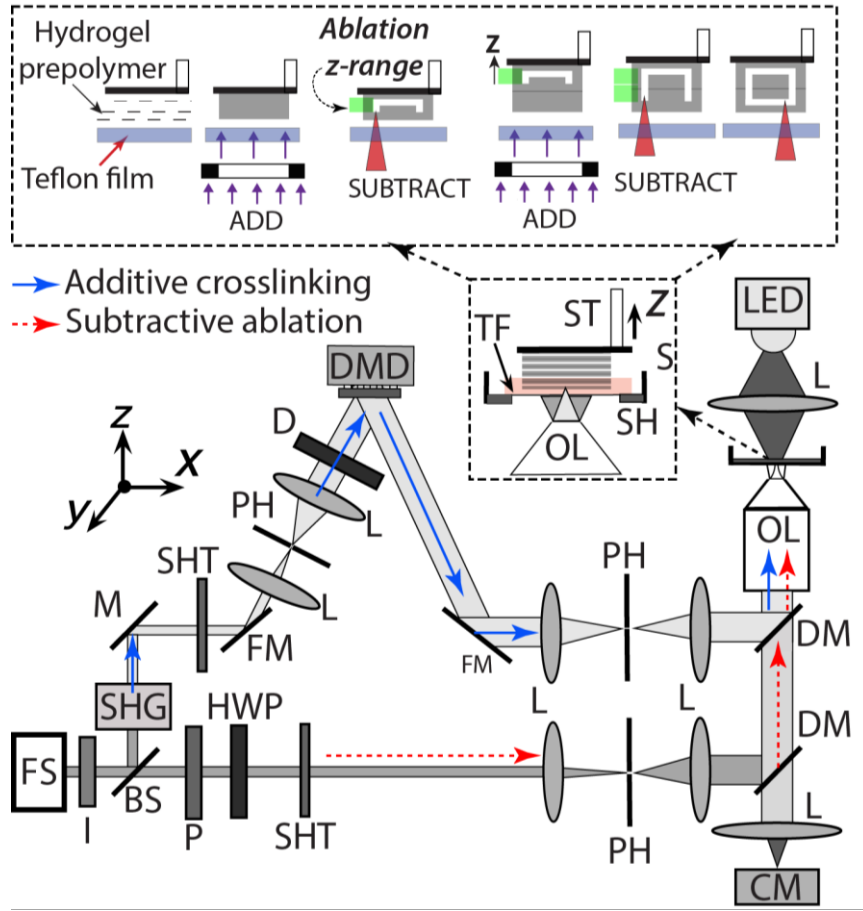


Figure 2.1. (A) Schematic of femtosecond laser-based additive-subtractive/additive-additive HLP machine. [FS-femtosecond laser, SHG-second harmonic generator, I-isolator, BS-beam splitter, P-polarizer, HWP-half waveplate, SHT-shutter, L-lens, PH-pin hole, FM-mirror in a flip mount, D-diffuser, DMD-digital micromirror device, DM- dichroic mirror, CM-camera, OL-objective, S-sample, SH-sample holder, ST-stage, TF-Teflon film]. Small dashed box: Schematic showing sample holder (SH) with teflon film (TF) and elevating stage (ST). Enlarged dashed box: Process flow of HLP showing one sequence of additive crosslinking and subtractive ablation steps.

2.4. Additive/subtractive mode of Hybrid laser printer

We characterized the dead-zone and ablation z-range of Hybrid laser printer. Fundamental to the HLP process is the relationship between the ‘dead-zone’ from the additive CLIP mode, and ‘ablation z-range’ from subtractive MPA mode (Figure 2.2A). Characterization of dead-zone is necessary for accurate determination of speed and z-resolution during the additive step while assessment of ablation z-range is important to determine the exact location of laser focus during the subtractive mode. Dead-zone is a thin uncrosslinked prepolymer solution between the Teflon window and the crosslinked hydrogel structure attached to the stage. This zone is created due to the inhibition of the photo-crosslinking process, a result of diffusion of oxygen through the permeable Teflon window. This prevents the adhesion of newly crosslinked layers to the bottom window and the liquid hydrogel prepolymer solution can freely refill the fabrication area adjacent to the Teflon window. The dead-zone thickness can vary in the order of tens of micrometers depending upon the control parameter such as laser intensity, exposure time, crosslinking properties of hydrogel, and local oxygen concentrations. Furthermore, the dead-zone defines the relationship between print speed and part resolution in the additive mode, and influences the linewidth of ablation part and penetration depths in the subtractive fabrication mode.

‘Ablation z-range’ is the region within the crosslinked hydrogel layers where material can be reliably removed in the subtractive ablation mode of HLP (Figure 2.2A). The two-photon absorption induced ablation process is limited to certain depth due to light absorption and scattering effects within the hydrogel, that defines the upper end of the ‘ablation z range.’ The lower end of the ‘ablation z-range’ is the region just above the dead-zone within the crosslinked hydrogel layer. Operating in this z-range ensures that the prepolymer solution does not inadvertently crosslink during the subtractive ablation step and avoids forming unwanted bubbles.

For this work, PEGDA prepolymer (90% by weight (wt), 700 MW) mixed with water soluble photoinitiator lithium phenyl-2,4,6-trimethylbenzoylphosphinate (LAP 1% by wt) was chosen as a model synthetic hydrogel prepolymer solution. Wavelengths of 400 nm and 800 nm were chosen for additive crosslinking (λ_{add}) and subtractive ablation (λ_{sub}) modes respectively. In order to estimate the dead-zone, the L shaped stage was placed exactly at 200 μm from the surface of the Teflon window. A spatially modulated laser beam ($\lambda_{\text{add}}=400\text{ nm}$) was used to crosslink a uniform square shaped structures for a range of crosslinking laser power (P_{add}) and exposure time (t_{add}). The thickness of the structures was measured using HIROX microscopy and was subtracted from 200 μm to obtain the dead-zone thickness as a function of P_{add} and t_{add} . (Figure 2.2B). For the laser dosage used in this work, the dead-zone thickness ranges from $8\pm 8\text{ }\mu\text{m}$ to $97\pm 3.5\text{ }\mu\text{m}$ and show an increasing trend with decreasing laser dosage. Increase in

dead-zone thickness essentially means that a higher speed can be implemented to fabricate structures.

To measure the ablation z-range, width of the ablated lines was characterized at different depths of crosslinked structure (Figure 2.2C). First PEGDA slab was crosslinked using crosslinking laser power of (P_{add}) of 150 mW and exposure time (t_{add}) of 20 s that results in small dead-zone of 30 μm . Next, lines were ablated within the crosslinked structure using the ablation laser powers of (P_{sub}) of 800 mW, 1000 mW and 1200 mW, and scanning speed (v_{sub}) of 100 $\mu\text{m/s}$. The ablated lines were written at the depth of 40 μm to 160 μm from the surface of Teflon window. Results demonstrate a decrease in linewidth with an increase in laser penetration depth, due to light absorption and scattering within the sample for all the laser powers. For P_{sub} of 800 mW, 1000 mW and 1200 mW, the upper ends of ablated z-range were measured to be 120 μm , 140 μm and 160 μm respectively. The lower ends of ablation-range were obtained from the dead-zone plot (Figure 2.2B). For a particular additive step with P_{add} of 150 mW and t_{add} of 20 s, the dead-zone thickness was measured as 30 μm , while for a particular subtractive step with P_{sub} of 1200 mW and v_{sub} of 100 $\mu\text{m/s}$, the upper end of the range was measured to be 160 μm , giving an ‘ablation z-range’ of $\sim 35\text{-}160$ μm . In a similar fashion, ablation z-ranges were calculated for a range of laser powers and scanning speeds, and these parameters were used to automate the HLP platform.

Next, the amount of material removal during the subtractive step of HLP was characterized in term of ablation linewidth. To do so, ablation laser powers (P_{sub}) and scanning speeds (v_{sub})

were varied and the widths of the ablated lines were measured. First, hydrogel slabs were crosslinked with P_{add} of 150 mW and t_{add} of 20 s. Second, laser ablation was carried out at a depth of 100 μm from the Teflon surface, and width of the ablated lines was measured using an optical microscope and the data was recorded by averaging 5 readings. As shown in Figure 2.2D, results show that the ablated linewidth decreases from 8 μm to 3 μm with an increase in scanning speeds (v_{sub}) and a decrease in ablation laser powers (P_{sub}). These data were used to determine the ablation laser power and scanning speed for achieving desired ablation linewidth. Our result suggests that the minimum feature size of the ablated line is around 3 μm , and this value is higher compared to resolution based on Abbe's resolution criteria. Considering Abbe's criteria, resolution is given by $d = \lambda / (2 \cdot \text{NA})$, where λ is wavelength of light and NA is numerical aperture. For two-photon absorption, the resolution improves roughly by a factor of $\sqrt{2}$ [7]. For a laser wavelength of 800 nm and numerical aperture of 0.55, the theoretical resolution of our optical setup should be ~ 514 nm. However, the mechanism of fs ablation of the hydrogel is dictated by the shockwave generation and bubble formation that extend beyond the laser focus spot and increases the feature size of ablated structure. Moreover, we only report the linewidth of fully ablated lines, and do not consider partial ablation or incomplete ablation events.

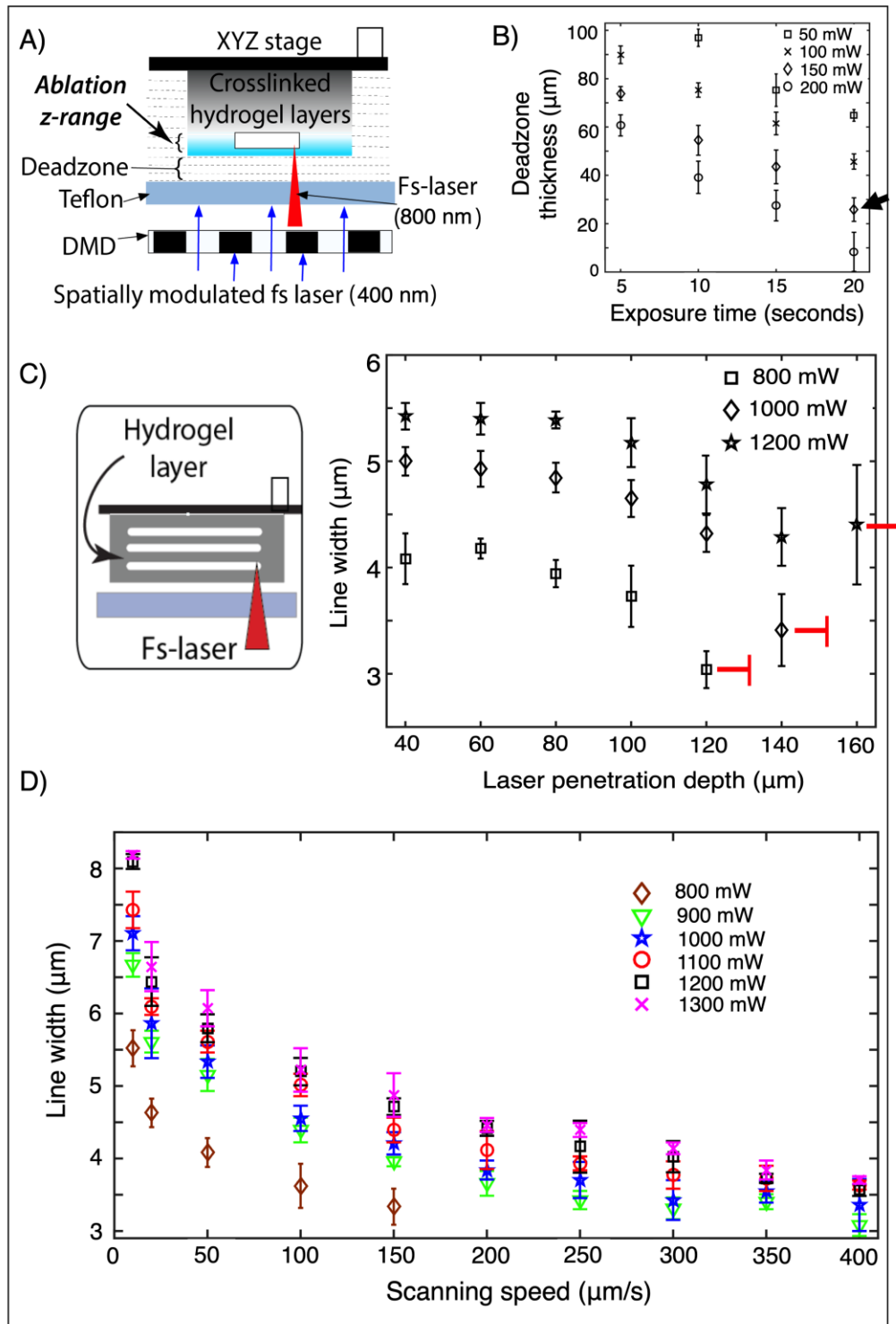


Figure 2.2. (A) Schematic showing key parameters in HLP. Ablation z-range and dead-zone are two key parameters, which are highlighted in the figure by curly bracket. Please note that the additive and subtractive processes are sequential processes, although they are

depicted in the same figure for simplicity. (B) Plot of dead-zone thickness as the function of exposure time and laser power. As for an instance, PEGDA slab crosslinked using crosslinking laser power of (P_{add}) of 150 mW and exposure time (t_{add}) of 20 s (marked by black arrow) results in dead-zone of 30 μm . (C) Schematic cartoon showing lines ablated at different penetration depths and plot of ablated linewidth as a function of laser penetration depths and laser powers. Results shows a decreasing linewidth trend with increasing laser penetration depth. Red marks in the plot represent the upper limit of ablation z-range. (D) Plot of ablated linewidth as a function of scanning speeds and laser powers. Plot shows a decreasing linewidth trend with decreasing laser dose. For all of the studies in this figure, 90% PEGDA and 1% LAP was used as material for fabrication.

Next HLP was used to print complex 3D structures with internal micro-features. To test the achievable design complexity of HLP, a Mayan pyramid, with a hollow cube-frame embedded within a 3D pyramid structure, was fabricated using 90% PEGDA, 1% LAP prepolymer solution. Briefly, a 3D model of a Mayan pyramid is sliced to generate digital masks for the DMD using a custom written algorithm, and additive-subtractive sequential processes were used to print the structure in an automated manner (Figure 2.3A, B). For the additive steps, laser wavelength (λ_{add}) of 400 nm and crosslinking laser power (P_{add}) of 200 mW was used to selectively crosslink PEGDA layers in a continuous fashion onto a methacrylated glass coverslip. For subtractive steps, a laser wavelength (λ_{sub}) of 800 nm, an ablation laser power

(P_{sub}) of 1200 mW, and a scanning speed (v_{sub}) of 100 $\mu\text{m/s}$ was used to ablate a hollow cube-frame within the crosslinked layers. (Figure 2.3B). The additive and subtractive process was iterated in an automated fashion to fabricate a Mayan pyramid (6 mm tall) with an embedded cube-frame (600 μm^3). The location of the cube is 2 mm inside the pyramid from the base of the pyramid (Figure 2.3C). A total fabrication time of 66 minutes was dominated by the time required for subtractive steps (62 minutes) as compared to all the additive steps combined (3.6 minutes) and the time required to transition between steps (0.4 minutes). This work demonstrates HLP's ability to remove material at any depth within a 3D structure. As compared to current laser based fabrication methods where laser penetration depth is substantially influenced by the optical properties of the prepolymer solution, HLP is less dependent on the optical properties of the prepolymer solution due to the sequential additive and subtractive modes of fabrication that enables the ablation of materials from any depth within a 3D structure.

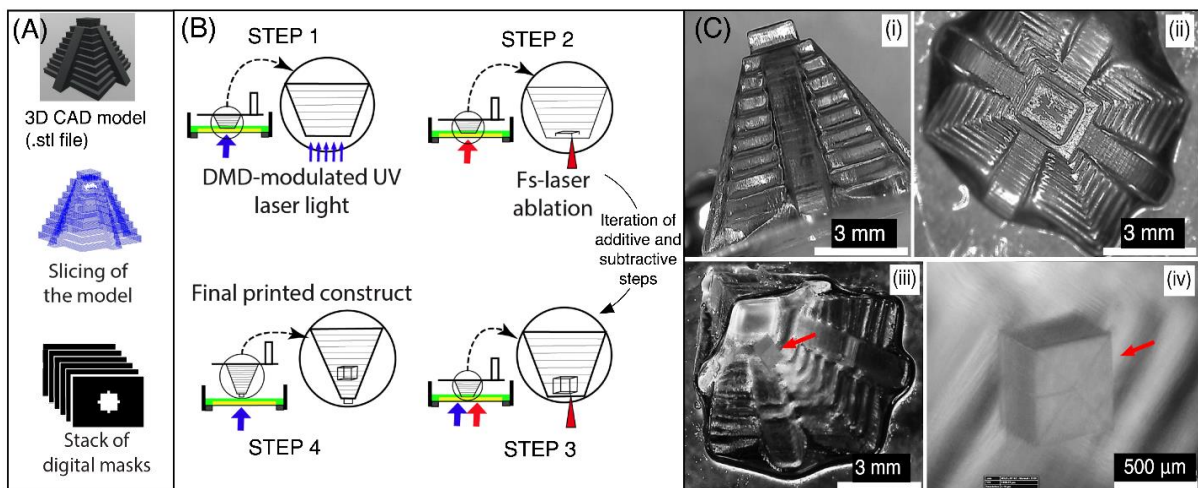


Figure 2.3. (A) Diagram showing slicing of an stl model of Mayan pyramid to create a stack of digital masks. (B) Key steps in the HLP process to print a Mayan pyramid with embedded

cube frame. Iteration of additive and subtractive steps are involved to print a complete ‘cube inside pyramid’ structure (C) Side, top and isometric views of ‘cube inside pyramid’ structure in 90% PEGDA, 1% LAP and the image is recorded by an HIROX digital optical microscope. For additive step laser power of 200 mW and laser wavelength of 400 nm was used, while laser power of 1200 mW, scanning speed of 100 μ m/s and laser wavelength of 800 nm was used for subtractive steps. The height of the pyramid is 6 mm. The cube is 600 μ m³, embedded 2 mm from the bottom of the pyramid. (red arrow points to the embedded cube).

To further demonstrate HLP’s printing capabilities, open-well chips were printed using 10% PEGDA 1% LAP (Figure 2.4). Multilayer 1.5 mm thick chips that consist of two open rectangular wells (1.25 mm \times 2.5 mm) connected by either in-plane microchannels (6 μ m in diameter) (Figure 2.4A) or out-of-plane microchannel (8 μ m) were printed (Figure 2.4B). For both these structures, the total printing time was 4.5 minutes. For chips with embedded in-plane microchannels, DMD-modulated laser beam was used to print rectangular wells using a λ_{add} of 400 nm, P_{add} of 150 mW and t_{add} of 20 s followed by ablation of microchannels in straight, zig-zag and square-wave configurations using a P_{sub} of 1200 mW and v_{sub} of 100 μ m/s. Repeated scans (2 times) are necessary to ensure that channels are not blocked with any debris. Rhodamine B dye, pipetted in one of the wells, was observed to perfuse within the channels under static hydrostatic pressure as shown in Figure 2.4A. Chips with out-of-plane 3D microchannels were fabricated using P_{add} of 150 mW, t_{add} of 20 s in the additive mode, and P_{sub}

of 1300 mW and v_{sub} of 50 $\mu\text{m/s}$ in the subtractive mode. Sequential additive and subtractive modes in HLP allow the ablation of 3D channel that span across multiple crosslinked layers (Figure 2.4B).

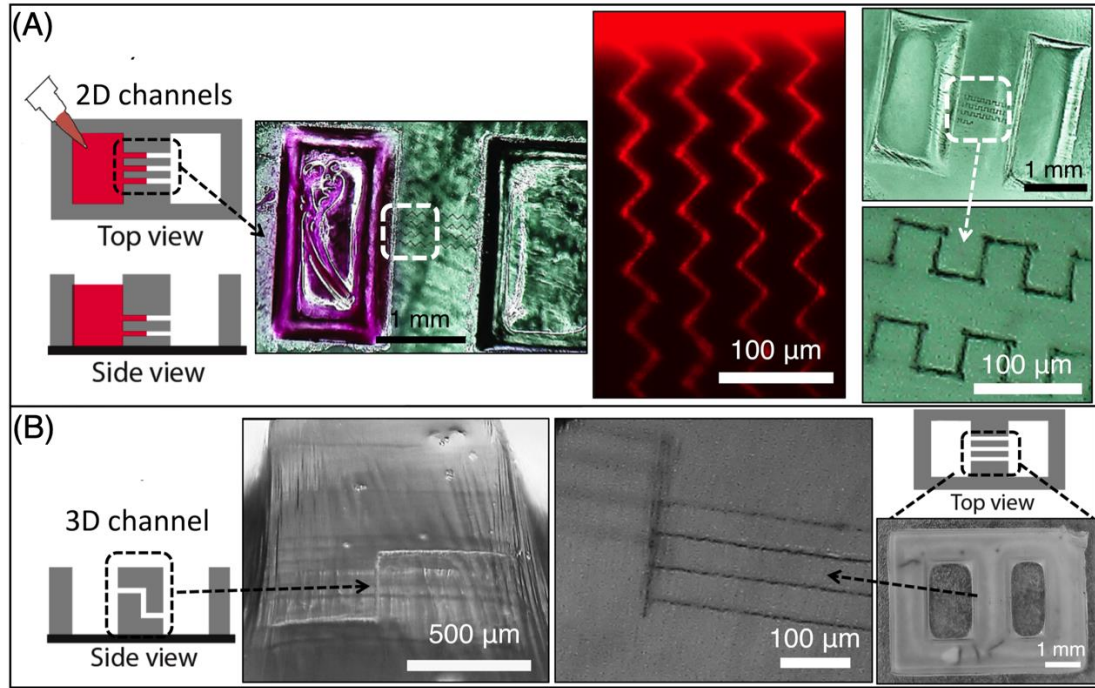


Figure 2.4. Printing user-defined two-well PEGDA chips with interconnecting in-plane and out-of-plane microchannels. (A) In-plane channels: side and top views of channels with zig-zag and square-wave configurations are depicted. Perfusion of Rhodamine B through zig-zag channels is demonstrated. (B) Out-of-plane channels: Side, isometric and top views of 3D channels spanning multiple crosslinked layers are depicted. White dotted box highlights the zig-zag ablated channels. For all of the studies in this figure, 10% PEGDA and 1% LAP was used for fabricating the structures.

To demonstrate the utility of HLP for potential bioscience applications, 4-well PEGDA chips with embedded microchannels were printed (Figure 2.5). To assess the utility of such chips in studying cell-cell communication, we choose model osteocyte cell line. In the bone tissue, osteocytes reside within isolated cavities (lacunae) and they communicate with their neighbouring cells by forming dendritic processes within hollow microchannels called canaliculi. To mimic this microenvironment, PEGDA chips, 200 μm thick, with 40 microchannels (diameter 5 μm) were ablated within walls (width=100 μm) that separate adjacent wells. These chips were printed using a P_{add} of 150 mW, t_{add} of 20 s, P_{sub} of 1200 mW, and v_{sub} of 200 $\mu\text{m/s}$. For the fabrication of these chips, a total printing time of 3 minutes was required. Mice MLO-Y4 osteocytes, seeded within the chips, remain isolated in their respective wells; however, they extend cell processes through the microchannels to establish direct physical contact with cells seeded in the adjacent well. This is confirmed by the presence of the nucleus on the either side of the wall, while only cell processes labelled by f-actin (green) is present within the channel (Figure 2.5A).

To potentially extend the utility of these chips to cell migration studies, the chip design was modified by increasing the wall thickness to 300 μm . A P_{sub} of 1400 mW and v_{sub} of 50 $\mu\text{m/s}$ was used to ablate channels of diameter 7 μm , a size that would facilitate cell migration within the channel (Figure 2.5B). Model human Saos-2 osteosarcoma cell line, chosen for this work, is able to migrate within the channels, as indicated by the presence of both f-actin (green) and nucleus (blue) within the interconnecting channels on day 4. For these chips, a total printing

time of 11 minutes was required to account for the increased wall thickness and channel sizes. Based on Figure 2.5A and Figure 2.5B, we can say that the resulting channels are open and are not clogged by debris. The process is not toxic to cells as seen in the figures, where seeded cells reliably migrate and form cell-cell connections within the microchannels. To demonstrate that HLP can be extended to other photosensitive hydrogels, 4-well chips using naturally-derived gelatin methacrylate (GelMA) hydrogel were printed using a P_{add} of 200 mW, t_{add} of 25 s, P_{sub} of 1000 mW, and v_{sub} of 100 $\mu\text{m/s}$. (Figure S2.2, Supp. Info)

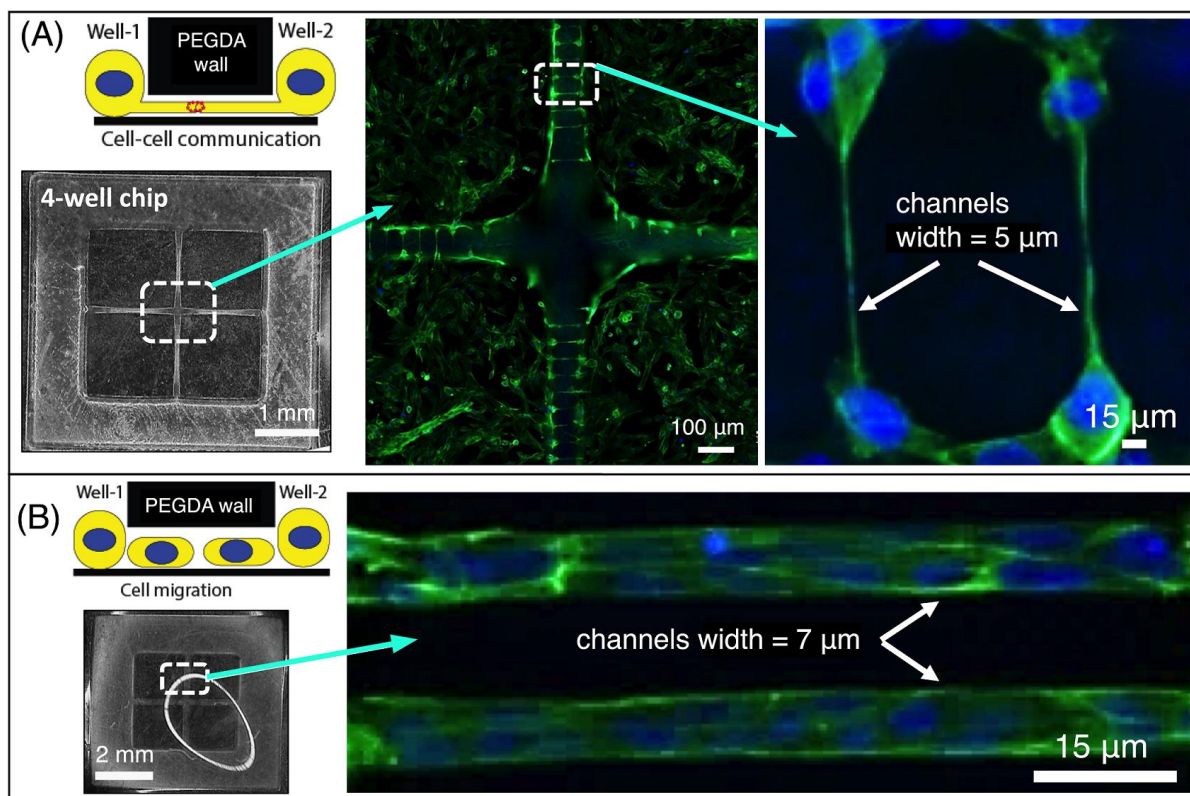


Figure 2.5. (A) Brightfield image of a 4-well PEGDA chips with inter-well microchannels is depicted. Fluorescent images showing actin (green) and nucleus (blue). MLO-Y4 cells seeded in neighboring wells communicate with each other by extending cell processes within the

ablated channels. White arrows point the communication channels with a diameter of 5 μm (B) Brightfield image of a 4-well PEGDA chips with inter-well microchannels is depicted. Seeded osteosarcoma Saos-2 cells migrate within the ablated channels. White arrows show the migration channels with a diameter of 7 μm . For all the studies in this figure, 10% PEGDA and 1% LAP was used for fabricating the open-well chips.

2.5 Additive/additive mode of Hybrid laser printer

HLP in additive DMD based printing (CLIP) and additive MPP was used to achieve on-demand fabrication of multiscale 3D structures with superior design flexibility. To demonstrate this capability, we choose to use model prepolymer solution (90% PEGDA, 1% LAP) to print a multi-tier design that consists of three log-pile structures printed on different Z-heights and XY locations. Figure 2.6A illustrates the sequence of steps, while Figure 2.6B shows the series of masks for additive CLIP and laser paths during the additive MPP steps. In the first step, a 200 μm thick layer was additively printed using CLIP (Mask 1). In the second step, MPP was used to print the first woodpile structure. This is followed by Step 3, where another 200 μm thick layer was printed using Mask 2 (CLIP). Similarly, sequential use of MPP and CLIP was used to print the rest of the structure (Steps 3-6). To clearly visualize the embedded 3D logpile structures in different z-planes without mechanical sectioning, a rhombus shaped blank structure was added to the DMD masks. Figure 2.6C depicts a representative HIROX digital

microscopy image of HLP-printed 3D multiscale structure. In this study, additive CLIP steps used a laser power of 200 mW and exposure time of 5 sec, while additive MPP steps used a laser power of 400 mW and scanning speed of 100 $\mu\text{m/s}$ using an objective lens (Zeiss, 20X) with numerical aperture of 0.25. The logpile structures consists of 10 layers of logpile structure (log-size=2 μm ; log-spacing=20 μm). Each logpile structure is $\sim 80 \mu\text{m}$ thick and each structure is printed at different z-levels/heights. (Figure S2.3, Supp. Info) The total fabrication time of 45 minutes is mostly dictated by the MPP steps. This work demonstrates that the HLP is capable of fabricating 3D multiscale structure using multistep and automated additive-additive approach.

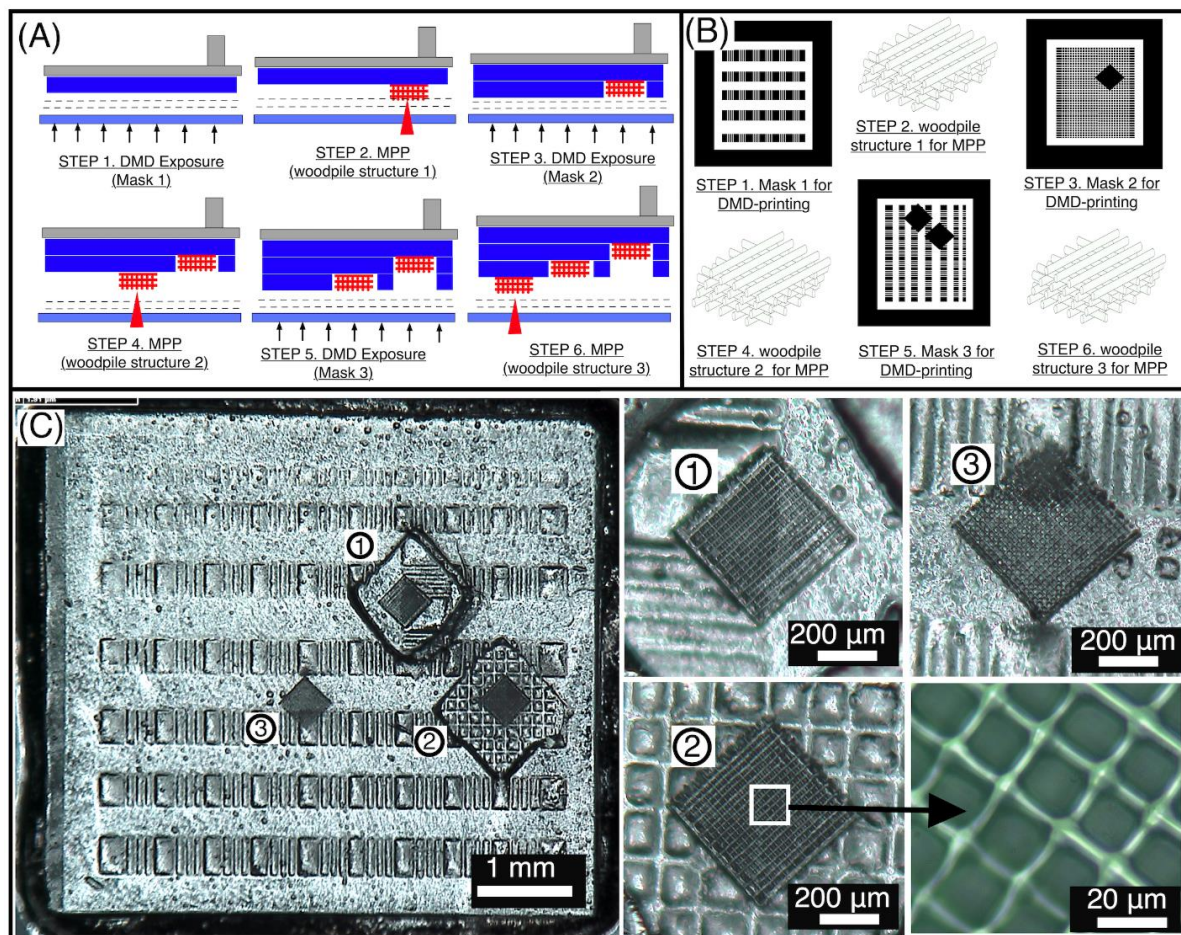


Figure 2.6. HLP's capability of additive-additive multiscale printing (A) Schematic depicting sequential additive steps of DMD based printing (CLIP) and multiphoton polymerization (MPP). Three woodpile structures were printed in different depth using MPP. (B) Corresponding DMD masks and wood pile structures. (C) HIROX digital optical microscopy image depicting three woodpile structures fabricated at different z-planes and xy spatial locations. Three different woodpile structure marked by 1, 2 and 3 correspond to the zoomed images to the left. Structure was printed using 10% PEGDA and 1% LAP with laser power of 200 mW and exposure time of 5 seconds in additive CLIP step. While high resolution MPP fabrication was performed using laser power of 400 mW and scanning speed of 100 $\mu\text{m/s}$.

2.6 Multi-material printing mode of Hybrid laser printer

To demonstrate the HLP's capability of printing multi-material 3D structures, we built a new fluid chamber with necessary tube connections to enable efficient switching of different prepolymer solutions. The fluid chamber was designed using Autodesk Inventor and machined using a vertical mill. The sample holder consists of the five 3-mm diameter inlets, printing region (also known as fabrication window) of 1 cm in diameter, and five 3-mm diameter outlets. Three inlets were used to pump different hydrogel prepolymer solutions, while the fourth and the fifth inlets were designed to pump in washing solution and/or nitrogen. Similarly, three of outlets were designed to pump-out the prepolymer solution to the respective syringes

so that the solutions can be reused. The other two outlets were used to drain the DI water during washing steps; this step is necessary to avoid mixing of different prepolymer solutions during printing. A circular hole (diameter 10 mm) was drilled in the center of the sample holder and a thin Teflon film was glued. This area is named as fabrication window where the exposure of the hydrogel prepolymer solution takes place. The floor of the fluid chamber was sloped so that the prepolymer solutions can be easily drained during the washing steps. Before introducing new prepolymer solution, compressed nitrogen was used to ensure the complete removal of DI water. While printing GelMA structures, the heater (shown in Figure S2.1, Supp. Info.) was maintained at 40 °C. This setup allowed for repeatable printing of multi-materials structures with no mixing of the prepolymer solutions.

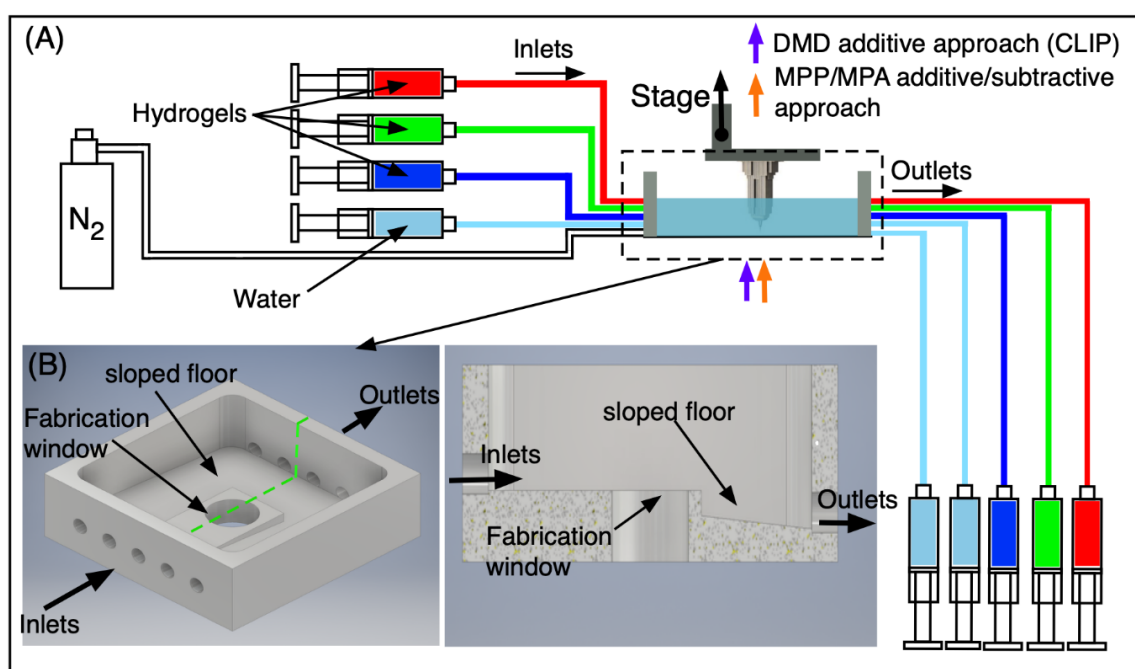


Figure 2.7. (A) Syringe pump system for multiscale, multimaterial fabrication. Three different inlets and three outlets were used for exchange of printing material. Nitrogen/water inlets and two water outlets were meant for washing and drying steps. (B) Side view of the fluid chamber, which depicts 5 inlets/5 outlets and fabrication area. Cross-section view (at marked green dotted line) shows the sloped floor design that facilitates easy exchange of prepolymer solutions during printing.

HLP in DMD based additive mode (CLIP) was used to demonstrate the multi-material printing capability in both the z (Mayan Pyramid, Figure 2.8A) and the xy (Yin-yang, Figure 2.8B) directions. First, digital masks and image of a Mayan Pyramid printed using three solutions composed of 90% PEGDA hydrogel, 1% LAP photoinitiator and food colour dye of different colors (blue, green, and red). This structure was printed using the crosslinking laser power (P_{add}) of 200 mW, a printing speed in the vertical direction of 0.02 mm/s, and an exposure time per layer (t_{add}) of 3 seconds. Similarly, yin-yang structure was printed using a laser power of (P_{add}) 200 mW and exposure time (t_{add}) of 5 seconds for each step. Second, additive DMD based mode (CLIP) was combined with additive MPP to print nested logpile multiscale 3D structures using three different polymer compositions. (Figure 2.8C) First, CLIP was used to print the outer thick pink wall using 20% GELMA, 0.25% LAP doped with Rhodamine B dye. Second, CLIP was used to print internal walls (that separate the wells) using 50% PEGDA, 1% LAP. For both these structures, a crosslinking laser power (P_{add}) of 200 mW and exposure time (t_{add}) of 5 seconds was used. Third, MPP was used to print high resolution logpile structure using a

laser power of 400 mW and scanning speed of 100 $\mu\text{m/s}$. The laser beam was focused using 20X objective lens (Zeiss, NA=0.25) to obtain a minimum feature size of 2 μm . Next, multi-material 3D printing capability was demonstrated by combining additive CLIP and subtractive MPA modes. Additive CLIP was used to print structures using two hydrogel compositions (90% PEGDA, 0.5% LAP with green food dye, 50% PEGDA, 0.5% LAP, with red food dye) with a laser power (P_{add}) of 200 mW and exposure time (t_{add}) of 5 s. (Figure 2.8D) Laser processing conditions to achieve a specific ablation size within both materials (Figure S2.4, Supp. Info) were used to ablate an array of channels in both regions using MPP. For this step, laser power was kept constant ($P_{\text{sub}}=1500$ mW) and the scanning speed was switched between 50 $\mu\text{m/s}$ to 150 $\mu\text{m/s}$. The plot shown in Figure S2.4 can be explicitly used to ablate desired linewidth structures in these material. For instance, to print a uniform channel of (~ 7.6 μm) throughout the both slabs, the scanning speed is required to maintain at 130 $\mu\text{m/s}$ inside 90% PEGDA slab and 50 $\mu\text{m/s}$ inside the 50% PEGDA slab.

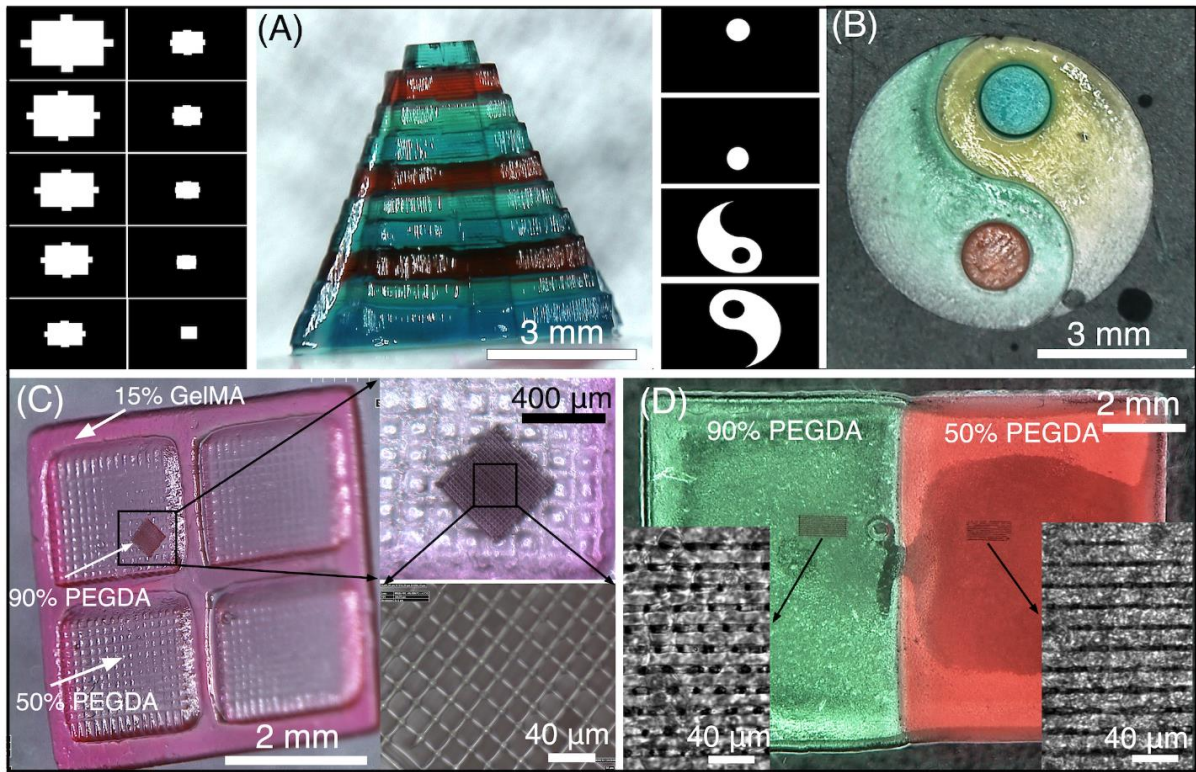


Figure 2.8. (A) Schematic depicting digital mask and multicolored Mayan pyramid fabricated using multimaterial additive printing of three colored 90% PEGDA, 1% LAP prepolymer solutions. (B) Ying and yang structure printed using four different colored 90% PEGDA, 1% LAP. (C) Multiscale printing of multimaterial structure using two commonly used hydrogel (GelMA and PEGDA). The outer thick wall colored in pink is printed with 15% GELMA, 0.5% LAP using DMD based fabrication. Similarly, the DMD based approach is used to print intersecting lines using 50% PEGDA, 1% LAP. Further logpile structure shown inside the black square box is printed using MPP based DLW approach using 90% PEGDA, 1% LAP. (D) Additive and subtractive multimaterial approach of fabrication is demonstrated using 90% PEGDA, 0.5% LAP (colored in green) and 50% PEGDA, 0.5% LAP (colored in red). Insets shows the zoomed version of ablated lines using MPA.

2.7. Discussion

2.7.1. Comparison of HLP with existing fabrication techniques

Contrary to materials found in nature that possess 3D structural hierarchy and material heterogeneity, man-made materials remain relatively simple. Current manufacturing technologies are limited by a trade-off between the use of multiple materials, overall size range, dimensionality, throughput and resolution. (Table S1) For instance, subtractive methods based on lithography (photo-, soft-, nanoimprint-lithography) exhibit excellent feature resolution, however these methods typically generate planar devices or they required complicated multiple bonding and stacking steps to fabricate devices with even simple 3D designs [8,13]. On the other hand, additive manufacturing methods such as FDM, MJM, and DLP offer 3D design flexibility, however achieving microscale resolution with these methods remain challenging [2-4]. Among the various fabrication methods at our disposal, ultrafast lasers, with their unique property of nonlinear multiphoton absorption, have revolutionized the processing of materials at micrometer scale using MPP and MPA [14,15]. In this work, we have designed and built a single versatile manufacturing platform coined as HLP. HLP, by combining additive CLIP with additive MPP and subtractive MPA processes, enables quick printing of centimeter-sized hydrogel chips with embedded hollow or solid micro-features; this would otherwise require, multiple planar fabrication followed by the complex alignment of multiple components using conventional lithography. Integration of subtractive MPA with CLIP also ensures reliable removal of material in defined locations. This is a clear advantage as compared to current 3D

printing methods where removal of support or sacrificial material from micro-channels/features remains challenging. Using several proof-of-concept studies, we demonstrate HLP's ability to shape soft hydrated and difficult-to-process hydrogel materials into complex multiscale structures that are either highly challenging, or time consuming to fabricate, or cannot be fabricated using current methods [16].

2.7.2. Comparison of HLP with existing laser based hybrid methods

Only a handful researchers have developed hybrid additive-subtractive methods using lasers due to the material incompatibilities and/or processing requirements [10,11]. One approach, that has been widely used, has combined ultrafast lasers in additive (MPP) and subtractive (MPA) modes to fabricate complex 3D structures using epoxy-based photoresists. However, time-consuming serial nature of the both MPP and MPA has limited the scalability of these methods and therefore their utility in the field for making centimeter sized devices [8,12]. In comparison, HLP combines additive CLIP with MPP/MPA processes to enable printing of centimeter-sized hydrogel chips with embedded micro-features within minutes. Another laser hybrid method utilizes specialized materials such as Foturan photosensitive glass to make hollow micro-features. This method involves two steps. In step 1, laser irradiation is used to modify the material properties to allow facile removal of materials using chemical etching. In step 2, MPP is used to crosslink complex 3D structure within the chemically etched channels. Since processing requirements for the etching and MPP steps are distinct, this approach cannot be automated into a multi-step multi-layer process. Additionally, the use of harsh chemical and

processes (etching and high temperature treatment) makes this process incompatible with hydrogel materials. In comparison, HLP technique can print 3D structures with embedded features at a resolution of few micrometers using a multi-step multi-layer automated process without the use of any harsh processing steps, a key materials criteria when working with soft hydrogel materials. Although we have utilized model synthetic PEGDA and naturally-derived GelMA hydrogels in this work, we anticipate that HLP can be extended to other photosensitive materials.

2.7.3. HLP can fabricate hollow micro-features at any depth within a 3D structure

Laser based methods such as MPA depend heavily on the optical properties (transparency, absorption, scattering) of the material [15-17]. Low laser penetration depths limit the processing range of subtractive ablation within the materials. In contrast, HLP technology allows the fabrication of hollow micro-features at any depth within a complex user-defined 3D microstructure. This unique feature is demonstrated by the printing of (i) an embedded hollow cube-frame deep within a Mayan Pyramid 3D structure (Figure 2.3C), (ii) an embedded out-of-plane microchannel within a two-well PEGDA chip (Figure 2.4B), and (iii) 3D log-pile structures at different depth/heights (Figure 2.6). The sequential additive-subtractive modes make this technique more-or-less independent of stringent processing depth limits. HLP can be potentially used to fabricate 3D structures using less transparent materials as well, thus decreasing the dependence of laser penetration depths on the optical properties of the materials.

2.7.4. HLP as compared to current light-based multi-scale fabrication methods

Laser based methods that combine two separate additive processing steps or methods have been used to fabricate multiscale 3D structures [18,19-21]. For instance, SLA was used to print multiscale surface features with a resolution of 37 μm by adaptively switching the laser spot and slice layer thicknesses [19]. Shaped laser beams with adaptive layer thicknesses were used to print 3D multiscale structures with a resolution of 30 μm , although hollow microscale features were not reported [20]. Large area multiscale printing was demonstrated by synchronizing linear scanner with high speed capability of galvano scanners [21]. As compared to the methods described above, HLP can print 3D multiscale structures with a smallest feature size of 3 μm . Figure 2.6 highlights the quick fabrication of 3D multiscale structures with superior design flexibility.

2.7.5. HLP as compared to current light based multi-material fabrication methods

Few light-based methods have been adopted for multi-material printing as explained below [22-27]. SLA and DMD based optical lithography have been used to print multiple low viscosity resins [23], and hydrogel-based materials [24]. To improve the fabrication speed, DMD-SLA was recently combined with a microfluidic device [25] and an air-jet [26] to achieve automated and quick material exchanges. Recently, a commercial direct laser writing system was combined with a microfluidic chamber to enable 3D multimaterial printing [27]. As compared to the current methods, HLP enables multi-material printing in additive-additive (CLIP-CLIP), additive-additive (CLIP-MPP), and additive-subtractive (CLIP-MPA) modes (Figure 2.8). By combining CLIP with MPP and MPA, HLP achieves a suitable trade-off

between the use of multi-materials, overall throughput, size-range and feature resolution, factors critically important in manufacturing 3D multiscale structures.

The HLP technology can be further improved to enable new capabilities. For instance, the maximum size of printable 3D structure can be increased by simply modifying the polymer chamber, and by adding new inlet channels can be used to increase the number of materials. Additionally, the speed of multi-material HLP can be further improved by adopting a continuous stop-flow lithography method and automation of fluid exchange and printing processes [28]. Furthermore, future studies can be made to better understand the ablation mechanism, which is not currently known. Based on known literature, the formation of shockwaves and cavitation, likely led to a disruptive breakdown of the hydrogel matrix and resulted in the generation of voids during the subtractive ablation mode of HLP, however systematic studies are required [11]. In the future, it is also advisable to study the chemical composition of the ablated regions, which is at this point difficult due to their microscale size of the ablation voids and mechanically weak nature of hydrogel materials.

In essence, we anticipate that HLP has the potential to revolutionize the ability to make 3D multiscale multi-material structures, specifically those structures that consist of internal or embedded hollow features that cannot be made using current technologies.

2.8 Conclusion

Due to material incompatibilities and significant differences in laser processing requirements of additive and subtractive processes, only few research groups have investigated hybrid fabrication approaches. In this work, we have designed and developed a new HLP technology that seamlessly combines additive crosslinking and subtractive ablation modes of femtosecond laser to achieve the printing of 3D multiscale multi-material structures using difficult-to-process hydrogel materials. Quick fabrication of multiscale structures with embedded hollow microfeatures demonstrates superior design flexibility of HLP as compared to conventional lithography methods, with a resolution close to that achieved by lithography. The ability to print multi-materials in additive-additive and additive-subtractive modes demonstrates the fabrication versatility of HLP. This capability can be potentially used to print 3D multi-material hydrogel-based structures for a variety of applications in biomedical sciences, microfluidics, soft robotics, optics, photonics, and other application areas.

2.9. Experimental Section

Optical setup for Hybrid Laser Printer (HLP). The schematic of the custom-built hybrid laser printing setup is shown in Figure 2.1. Both additive and subtractive modes of HLP utilize a femtosecond (fs) laser source (Coherent, Chameleon-Ultra Ultrafast Ti:Sapphire) capable of producing 150-fs wide pulses at a repetition rate of 80 MHz, with tunable fundamental wavelength ranging from 690-1040 nm. In the additive mode of HLP (shown by blue arrow in

Figure 2.1), fs-laser beam is passed through a second harmonic generator (SHG) (Autotracker, Coherent) to obtain an ultraviolet/near visible wavelength. A shutter (SH05, Thorlabs Inc) is placed after SHG generator and 2f-transfer lens ($f=40$ mm and 200 mm) assembly, which collimates and expands the laser beam. A pin hole of $25\text{ }\mu\text{m}$ is used to spatially clean the laser beam. The Gaussian intensity distribution of the laser beam is changed to hat-top intensity distribution using an engineered diffuser (RPC photonics Inc.) in a rotating mount and the beam is spatially modulated via a DMD (0.95" 1080p UV DMD, DLi Inc). DMD is a spatial light modulator consisting of an array of micromirrors. User can selectively switch mirrors into either an ON state or an OFF state to modulate laser beam in user-defined light-patterns using a computer-generated digital mask. A DMD-modulated fs-laser beam is projected to the sample with the infinity corrected projection optics. Laser beam modulated by the DMD can be used to crosslink photosensitive hydrogels in both continuous and layer-by-layer manner, with a feature size ranging from $\sim 30\text{ }\mu\text{m}$ to 1 cm. A custom written MATLAB code is used to slice a 3D model of the structure and to obtain a series of DMD mask.

The subtractive mode of HLP utilizes the fs direct laser writing to fabricate structure using multiphoton ablation (MPA) process. However, this mode can also be used as multiphoton polymerization (MPP) mode simply by adjusting the laser intensity. The fs laser beam tuned at 800nm is passed through an assembly of a half-wave plate and a polarizing beam splitter, which is used to adjust the intensity of the incident laser beam. The laser beam is spatially cleaned

and collimated using a 2f-transfer lens ($f=40$ mm and 200 mm) assembly and a 25 μm pinhole. The beam is directed towards the dichroic filters (Semrock, FF395/495/610-Di01-25x36) which reflects the laser beam towards objective lens (Carl Zeiss, 50X, 0.55 NA). The objective lens focuses the laser beam into the previously crosslinked hydrogel layer. Material from predefined region is ablated when the laser intensity exceeds the ablation threshold of the crosslinked hydrogel layer. The in-situ fabrication process can be monitored in real-time using a microscopy arm incorporated in the setup. A custom-written LabVIEW program is used to synchronize the additive and subtractive processes, including switching the DMD masks, turning the shutter ON and OFF, and moving of XYZ stages. It is worth noting, that for all the experiments, laser power was measured at the back aperture of the objective lens, however for the additive crosslinking, power (P_{add}) was measured just before the DMD. The coverslips used in this work were methacrylated to ensure adhesion of crosslinked structure.

Measurement of linewidth. The linewidth of the structure was imaged by Zeiss microscopy and measured via ImageJ software. Line profiles of the structures were plotted and full width at half maxima (FWHM) was recorded to obtain the linewidth. The linewidth of the structures was averaged from 5 line profiles.

Surface modification of glass substrate. Glass coverslips (18 mm \times 18 mm, No.1; Globe Scientific) were surface modified with methacrylated function group to ensure adhesion of crosslinked structure to the glass during HLP printing. Briefly, glass coverslips were treated in piranha solution (sulfuric acid and hydrogen peroxide, 7:3 ratio) for 20 minutes, washed with

MilliPore water and 100% ethanol (Fisher Scientific, Pittsburgh, PA), blow-dried using compressed air, and soaked in a bath containing 85 mM 3-(trimethoxysilyl) propyl methacrylate (Fluka, St. Louis, MO) in ethanol with acetic acid (pH 4.5) for 12 hours at room temperature, and subsequently washed in 100% ethanol and air dried.

LAP photoinitiator synthesis. Lithium phenyl-2,4,6-trimethylbenzoylphosphinate (LAP) was synthesized in a two-step process based on an established method [29]. At room temperature and under argon, 2,4,6-trimethylbenzoyl chloride (4.5 g, 25 mmol) was added dropwise to continuously stirred dimethyl phenylphosphonite (4.2 g, 25 mmol). This solution was stirred for 24 hours before adding an excess of lithium bromide (2.4 g, 28 mmol) in 50 mL of 2-butanone to the reaction mixture at 50°C, to obtain a solid precipitate after 10 minutes. The mixture was then cooled to room temperature, allowed to rest overnight and then filtered. The filtrate was washed with 2-butanone (3 x 25 mL) to remove unreacted lithium bromide and dried under vacuum to give LAP (6.2 g, 22 mmol, 88% yield) as a white solid.

Preparation of PEGDA and GelMA prepolymer solutions. Different concentrations of Poly (ethylene glycol) diacrylate (PEGDA, Mw=700, Sigma-Aldrich) prepolymer solutions were prepared for this project. First, LAP (0.4 gm) was added to 4 ml of Millipore water and mixed thoroughly using Vortex mixer (Vortex-Genie 2 from Fisher Scientific). Second, 36 ml of 100% PEGDA hydrogel is added to the 4 ml of LAP solution to prepare 90% PEGDA solution and

further mixed in Vortex mixer, and incubated at 37 °C to remove the bubbles. Similarly, 10% and 50% PEGDA prepolymer solutions were also prepared.

Gelatin Methacrylate (GelMA) macromer was synthesized as described previously [30]. Briefly, 200 ml Dulbecco's phosphate buffered saline (DPBS, Gibco) was heated to 40 °C, and was used to dissolve 10 gm of porcine skin gelatin (Sigma Aldrich, St. Louis, MO). Further, methacrylic anhydride was subsequently added to the solution and stirred for 3 hours. The unreacted groups from the solution was removed by dialyzing the mixture against distilled water for a week at 40 °C. Next, the dialyzed GelMA was lyophilized in a freeze dryer (Labconco, Kansas City, MO) for another week. A stock solution was prepared by mixing 0.75 g freeze dried GelMA with 10 ml of deionized water at 40 °C and 0.01875 gm of LAP photoinitiator to obtain a 10% (w/v) GelMA with 0.25% LAP (w/v).

Cell culture. All the cells used in the experiment were cultured under standard cell culture conditions (5% CO₂; 37 °C). MLO-Y4 osteocytes were maintained in α -Modified Eagle Medium (α -MEM, Gibco) supplemented with 2.5% heat inactivated FBS, 2.5% calf serum (CS), 1% P/S and 1% Glutamax on rat tail type I collagen-coated flasks, and passage 9-15 were used. Saos-2 human osteosarcoma cells were maintained in DMEM supplemented with 10% FBS, 1% P/S and 1% Glutamax, and were passaged when 70-80% confluence was reached.

Cell culture within PEGDA chips. Multi-wells PEGDA chips were designed and printed using HLP. The PEGDA multi-well chips were coated with rat tail type I collagen at 37 °C overnight and then flushed with DPBS before seeding either MLO-Y4 osteocytes or Saos-2 osteosarcoma

cells at a final concentration of 1 M/ml. Specifically, a 2 μ l cell solution was added to the chips, and placed in the incubator (37 oC) for 20 minutes to allow for sufficient attachment of the cells, before adding medium to the entire chip and culturing them under standard culture conditions. Live/Dead assay kit (Invitrogen) (Calcein AM, Ethidium homodimer) was used to quantify the viability of cells after 3 days of culture. Briefly, a solution of 0.5 μ l/ml calcein AM and 2 μ l/ml Ethidium homodimer in BME was pipetted into PEGDA biochips, incubated at 37 oC for 45 minutes before capturing images using an inverted microscope (Nikon Eclipse). To determine cellular morphology, cells cultured within chips were fixed with 4% formaldehyde (Invitrogen, Carlsbad, CA) for 30 mins, soaked in 2% Triton X-100 in DPBS for 30 minutes, and subsequently stained with phalloidin (Alexa-Fluor 568, Invitrogen) (1/100 dilution in DPBS) (45 mins at RT) and with 1.25 μ g/ml DAPI (Life Technologies) (5 minutes at RT) to visualize f-actin and cell nuclei respectively.

Digital optical microscope imaging. The fabricated structures were imaged and characterized using a digital optical microscope (HIROX, KH-8700). The MXG-2016Z /MX-2016Z 20-160x objective lens was used to image the fabricated structures, which provided a resolution of 1.35 μ m.

2.10 Supporting Information

2.10.1 Sample holder and stage

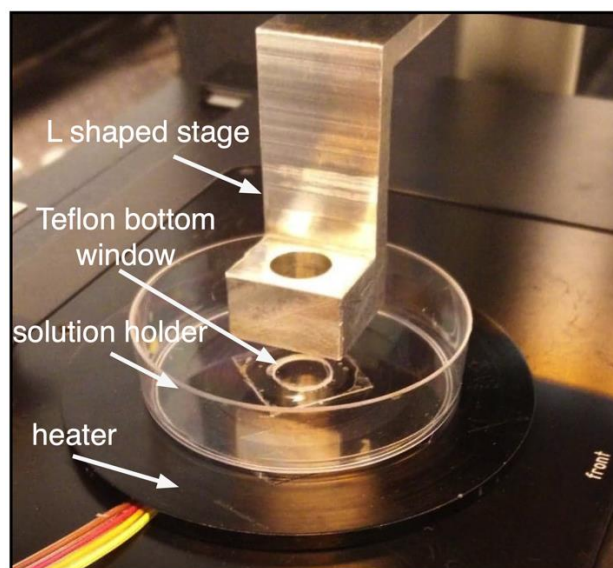


Figure S2.1. Photographs showing the sample holder and stage used in Hybrid laser printing.

Figure S2.1 shows the photograph of the sample holder assembly. This sample holder assembly consists of heater (WP-16 Warner instrument), and plastic petri dish (prepolymer hydrogel solution holder) and L shaped stage. The heater is maintained at 40 °C for GelMA printing and is turned off during PEGDA printing. The L-shaped stage is controlled by a three-dimension linear stage (Newport) and controller EPS301 (Newport). A hole was bored in the center of the petri dish and 45 μm thick Teflon film (Teflon AF 2400) was glued as a bottom window. An oxygen permeable (1000 barrers; 1 barrer = $10^{-10} \text{ cm}^3 \text{ (STP) cm cm}^{-2} \text{ s}^{-1} \text{ cmHg}^{-1}$), UV transparent, and chemically inert Teflon film was used as a bottom window to ensure that the fabricated structure does not get attached to the solution holder. The bottom window was created using an oxygen-permeable Teflon film of 45 μm . Even with this thickness, Teflon was able to maintain a robust

window without sagging or warping. Thin film created using other materials with higher oxygen permeability such as PDMS were found to have low flexural rigidity, a key criterion for the bottom window in this work. We found that PDMS film of thickness $\sim 600\text{ }\mu\text{m}$ or more was needed to serve as the bottom window.

2.10.2 Fabrication of GelMA microfluidic chip using HLP

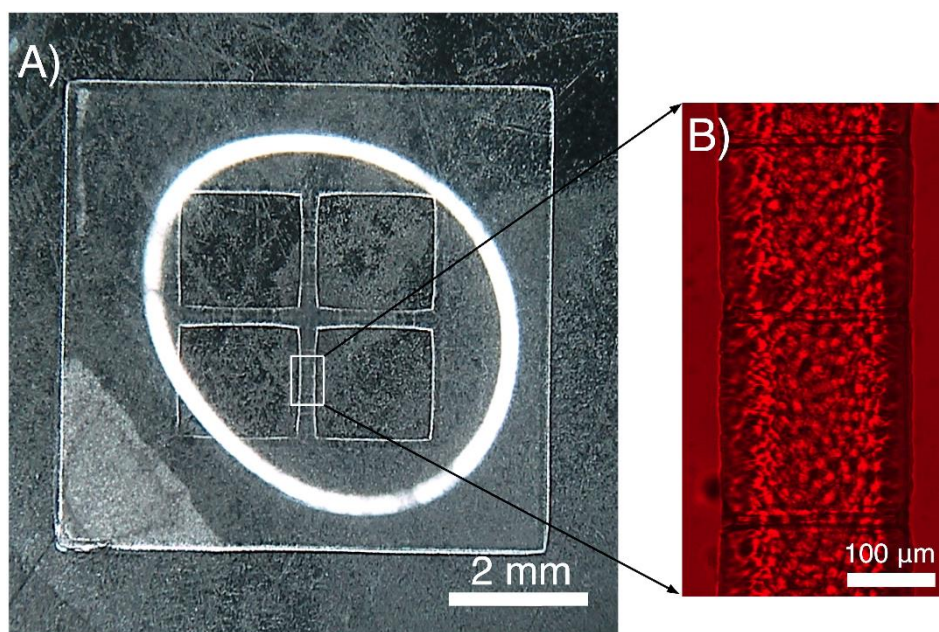


Figure S2.2. A) Four well microfluidic chips fabricated in 10% GelMA and 0.25% LAP using HLP. Rectangular wells were printed using a crosslinking laser wavelength (λ_{add}) of 365 nm, crosslinking laser power (P_{add}) of 200 mW and exposure time (t_{add}) of 25 s. In subtractive mode of HLP, ablation wavelength(λ_{sub}) of 730 nm, ablation laser power (P_{sub}) of 1000 mW and scanning speed (v_{sub}) of 100 $\mu\text{m/s}$ was used. Image was recorded using HIROX microscope. B) Optical microscopy image of wall between the wells with embedded microchannels.

2.10.3 Fabrication of hybrid (additive- additive) laser printing of three dimensional multiscale structure.

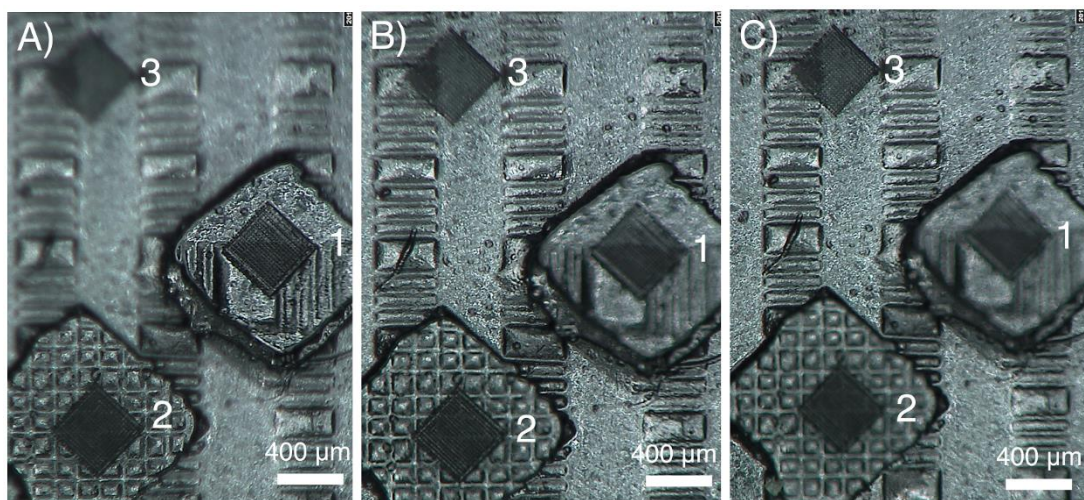


Figure S2.3. Imaging of woodpile structure fabricated at different depth (at the interval of 200 μm) of the three dimensional multiscale structure. A) Woodpile structure 1 is at focus, whereas woodpile structure 2 and 3 are out of focus B) Woodpile structure 2 is at focus and woodpile structure 1 and 3 are out of focus C) Woodpile structure 3 is at focus and wood pile structure 1 and 2 are out of focus.

2.10.4 Study of ablated linewidth as a function of scanning speed for 90% PEGDA and 50% PEGDA hydrogels.

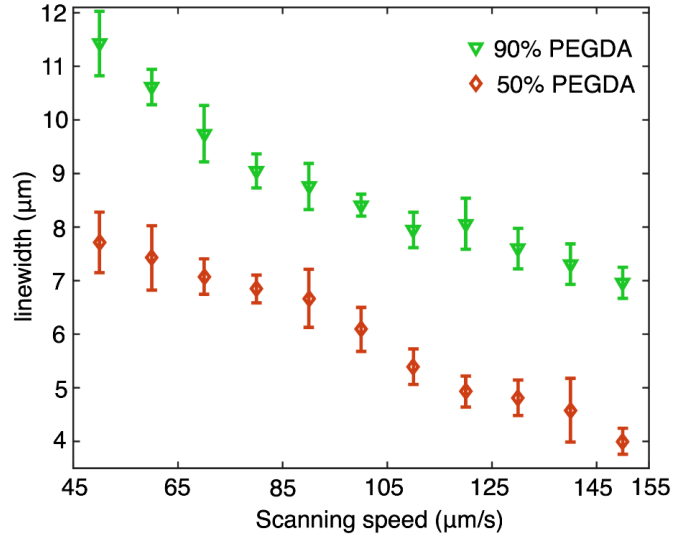


Figure S2.4. Plot depicting the linewidth of the ablated features, which are shown in the Figure 2.7D. A laser power of the 1300 mW was kept constant and the scanning speed was varied from the 50 $\mu\text{m/s}$ to 150 $\mu\text{m/s}$ to ablate feature in 90% PEGDA, 0.5% LAP (marked in green) and 50% PEGDA, 0.5% LAP (marked in red).

2.10.5 Comparison of Hybrid laser printer with existing fabrication technology.

Table S2.1. HLP can print centimeter-scale 3D structures with micrometer resolution and high design flexibility (FDM-Fused Deposition Modeling; MJM-Multijet modeling; SLA-

Stereolithography; DMD-Digital Micromirror Device; CLIP-Continuous liquid interface production; MPP-Multi-photon polymerization; MPA-Multi-photon ablation).

Methods	Channel resolution	Fabrication speed	Design flexibility in 3D	Size range	Use of multi-material
Lithography	<1 μ m	Slow (manual steps)	Low (multiple bonding steps and alignment required)	cm to sub- μ m	Difficult
FDM, MJM	>50-100 μ m	Fast	High	cm to ~100 μ m	Easy
SLA	>25 μ m	Slow	High	cm to ~25 μ m	Medium difficulty
DMD (CLIP)	~100 μ m	Fast	Medium	cm to ~50 μ m	Medium difficulty
MPP	~1 μ m	Slow (serial writing)	High (however low scalability)	sub-mm to 1 μ m	Difficult
MPA	~1 μ m	Slow (serial writing)	High (however low scalability as penetration depth depends upon material's optical properties)	sub-mm to 1 μ m	Not applicable
HLP (This work)	~1 μ m	Fast (CLIP) Slow (MPP/MPA)	High	cm to 1 μ m	Medium difficulty

2.11 References

- [1] Y. Xia, G. M. Whitesides, *Angewandte Chemie International Edition* **1998**, 37, 550; J. R. Tumbleston, D. Shirvanyants, N. Ermoshkin, R. Janusiewicz, A. R. Johnson, D. Kelly, K. Chen, R. Pinschmidt, J. P. Rolland, A. Ermoshkin, *Science* **2015**, 2397; D. Rus, M. T. Tolley, *Nature* **2015**, 521, 467; E. W. Esch, A. Bahinski, D. Huh, *Nature reviews Drug discovery* **2015**, 14, 248.
- [2] A. K. Au, W. Huynh, L. F. Horowitz, A. Folch, *Angewandte Chemie International Edition* **2016**, 55, 3862.
- [3] S. Khan, L. Lorenzelli, R. S. Dahiya, *IEEE Sensors Journal* **2015**, 15, 3164.

- [4] S. Waheed, J. M. Cabot, N. P. Macdonald, T. Lewis, R. M. Guijt, B. Paull, M. C. Breadmore, *Lab on a Chip* **2016**, *16*, 1993; C. M. B. Ho, S. H. Ng, K. H. H. Li, Y.-J. Yoon, *Lab on a Chip* **2015**, *15*, 3627.
- [5] J. R. Tumbleston, D. Shirvanyants, N. Ermoshkin, R. Janusiewicz, A. R. Johnson, D. Kelly, K. Chen, R. Pinschmidt, J. P. Rolland, A. Ermoshkin, *Science* **2015**, *347*, 1349.
- [6] L. Li, J. T. Fourkas, *Materials Today* 2007, *10*, 30; M. Farsari, M. Vamvakaki, B. N. Chichkov, *Journal of Optics* **2010**, *12*, 124001; J.-F. Xing, M.-L. Zheng, X.-M. Duan, *Chemical Society Reviews* **2015**, *44*, 5031.
- [7] M. Farsari, B. N. Chichkov, *Nature photonics* **2009**, *3*, 450; S. Maruo, O. Nakamura, S. Kawata, *Optics letters* **1997**, *22*, 132; J. Fischer, M. Wegener, Three-dimensional optical laser lithography beyond the diffraction limit. *Laser Photonics Rev.* **2013**, *7*, 22–44.
- [8] J. Chen, Y. Zhou, D. Wang, F. He, V. M. Rotello, K. R. Carter, J. J. Watkins, S. R. Nugen, *Lab on a Chip* **2015**, *15*, 3086; D. Qin, Y. Xia, G. M. Whitesides, *Nature protocols* **2010**, *5*, 491; C. Chen, D. Hirdes, A. Folch, *Proceedings of the National Academy of Sciences* **2003**, *100*, 1499.
- [9] R. R. Gattass, E. Mazur, *Nature photonics* **2008**, *2*, 219; K. Sugioka, Y. Cheng, K. Midorikawa, *Applied Physics A* **2005**, *81*, 1; S. Eaton, R. Osellame, R. Ramponi, "Femtosecond laser micromachining for the realization of fully integrated photonic and microfluidic devices", presented at *Integrated optics: devices, materials, and technologies XIX*, **2015**.

- [10] F. Sima, H. Kawano, A. Miyawaki, L. Kelemen, P. Ormos, D. Wu, J. Xu, K. Midorikawa, K. Sugioka, *ACS Applied Bio Materials* **2018**, *1*, 1667.
- [11] F. Sima, K. Sugioka, R. M. Vázquez, R. Osellame, L. Kelemen, P. Ormos, *Nanophotonics* 2018, *7*, 613; K. Sugioka, D. Wu, J. Xu, F. Sima, K. Midorikawa, "Hybrid Subtractive and Additive Micromanufacturing using Femtosecond Laser for Fabrication of True 3D Biochips", presented at *CLEO: Applications and Technology*, **2015**; C. Hnatovsky, R. Taylor, E. Simova, P. Rajeev, D. Rayner, V. Bhardwaj, P. Corkum, *Applied Physics A* **2006**, *84*, 47; K. Sugioka, Y. Cheng, *Lab on a Chip* 2012, *12*, 3576; S. Pradhan, K. A. Keller, J. L. Sperduto, J. H. Slater, *Advanced healthcare materials* **2017**, *6*, 1700681; L. Jonušauskas, S. Rekštyte, R. Buividas, S. Butkus, R. Gadonas, S. Juodkasis, M. Malinauskas, *Optical Engineering* **2017**, *56*, 094108.
- [12] W. Xiong, Y. S. Zhou, X. N. He, Y. Gao, M. Mahjouri-Samani, L. Jiang, T. Baldacchini, Y. F. Lu, *Light: Science & Applications* **2012**, *1*.
- [13] M. A. Unger, H.-P. Chou, T. Thorsen, A. Scherer, S. R. Quake, *Science* **2000**, 288, 113; M. Zhang, J. Wu, L. Wang, K. Xiao, W. Wen, *Lab on a Chip* **2010**, *10*, 1199.
- [14] Y.-L. Sun, W.-F. Dong, L.-G. Niu, T. Jiang, D.-X. Liu, L. Zhang, Y.-S. Wang, Q.-D. Chen, D.-P. Kim, H.-B. Sun, *Light: Science & Applications* **2014**, *3*, 129.
- [15] M. B. Applegate, J. Coburn, B. P. Partlow, J. E. Moreau, J. P. Mondia, B. Marelli, D. L. Kaplan, F. G. Omenetto, *Proceedings of the National Academy of Sciences* **2015**, *112*, 12052.

- [16] Y. S. Zhang, A. Khademhosseini, *Science* **2017**, 356, 3627; D. Seliktar, *Science* **2012**, 336, 1124; A. S. Hoffman, *Advanced drug delivery reviews* **2012**, 64, 18; C. Keplinger, J.-Y. Sun, C. C. Foo, P. Rothmund, G. M. Whitesides, Z. Suo, *Science* **2013**, 341, 984; C. Larson, B. Peele, S. Li, S. Robinson, M. Totaro, L. Beccai, B. Mazzolai, R. Shepherd, *Science* **2016**, 351, 1071; L. Ionov, *Materials Today* **2014**, 17, 494.
- [17] L. Li, M. Hong, M. Schmidt, M. Zhong, A. Malshe, B. Huis, V. Kovalenko, *CIRP Annals-Manufacturing Technology* **2011**, 60, 735; N. I. Smith, K. Fujita, O. Nakamura, S. Kawata, *Applied Physics Letters* **2001**, 78, 999.
- [18] X. Li, H. Choi, Y. Yang, *Thin Solid Films* **2002**, 420, 515; H. Exner, A. Streek, "High resolution laser micro sintering/melting using q-switched and high brilliant laser radiation", presented at *Laser 3D Manufacturing II*, **2015**; A. Piqué, N. A. Charipar, R. C. Y. Auyeung, H. Kim, S. A. Mathews, "Assembly and integration of thin bare die using laser direct-write", *Proc. SPIE 6458, Photon Processing in Microelectronics and Photonics VI* **2007**, 645802.
- [19] Y. Li, H. Mao, P. Hu, M. Hermes, H. Lim, J. Yoon, M. Luhr, Y. Chen, W. Wu, *Advanced Materials Technologies* **2019**, 1800638.
- [20] H. Mao, Y.-S. Leung, Y. Li, P. Hu, W. Wu, Y. Chen, *Journal of Micro and Nano-Manufacturing* **2017**, 5, 040905.
- [21] L. Jonušauskas, D. Gailevičius, T. Baravykas, S. Juodkasis, M. Malinauskas, "Mesoscale ultrafast laser 3D lithography: throughput in voxels-per-second", presented at *3D Printed Optics and Additive Photonic Manufacturing*, **2018**.

- [22] A. Bandyopadhyay, B. Heer, *Materials Science and Engineering: R: Reports* **2018**, 129, 1.
- [23] J.-W. Choi, H.-C. Kim, R. Wicker, *Journal of Materials Processing Technology* **2011**, 211, 318.
- [24] V. Chan, J. H. Jeong, P. Bajaj, M. Collens, T. Saif, H. Kong, R. Bashir, *Lab on a Chip* **2012**, 12, 88.
- [25] A. K. Miri, D. Nieto, L. Iglesias, H. Goodarzi Hosseinabadi, S. Maharjan, G. U. Ruiz-Esparza, P. Khoshakhlagh, A. Manbachi, M. R. Dokmeci, S. Chen, *Advanced Materials* **2018**, 30, 1800242.
- [26] K. Kowsari, S. Akbari, D. Wang, N. X. Fang, Q. Ge, *3D Printing and Additive Manufacturing* **2018**, 5, 185.
- [27] F. Mayer, S. Richter, J. Westhauser, E. Blasco, C. Barner-Kowollik, M. Wegener, *Science Advances* **2019**, 5, 9160.
- [28] D. Dendukuri, D. C. Pregibon, J. Collins, T. A. Hatton, P. S. Doyle, *Nature materials* **2006**, 5, 365.
- [29] B. D. Fairbanks, M. P. Schwartz, C. N. Bowman, K. S. Anseth, *Biomaterials* **2009**, 30, 6702.
- [30] S. W. Sawyer, S. V. Shridhar, K. Zhang, L. D. Albrecht, A. B. Filip, J. A. Horton, P. Soman, *Biofabrication* **2018**, 10, 035013.

CHAPTER 3: Femtosecond laser induced densification within cell-laden hydrogels

results in cellular alignment*

3.1 Abstract

The unique capabilities of ultrafast lasers to introduce user-defined microscale modifications within 3D cell-laden hydrogels have been used to investigate fundamental cellular phenomenon such as adhesion, alignment, migration and organization. In this work, we report a new material modification phenomenon coined as ‘densification’ and its influence on the behavior of encapsulated cells. Femtosecond laser writing technique was used to write densified lines of width 1-5 μ m within the bulk of gelatin methacrylate (GelMA) constructs. We found that densified micro-lines within cell-laden GelMA constructs resulted in preferential and localized alignment of encapsulated human endothelial cells. Degree of cellular alignment was characterized as a function of cell-culture time and the spacing between the densified line patterns. This phenomenon was found to be true for several cell lines, including mouse fibroblasts and osteocytes, and mesenchymal stem cells derived from human induced pluripotent cells. This first report of physical densification using fs lasers can be potentially extended for investigating cell behavior within other photosensitive hydrogels.

*Adapted from: Z. Xiong, H.Y. Li, P. Kunwar, Y. Zhu, R. Ramos, S. Mcloughlin, T. Winston, Z. Ma, P. Soman, Femtosecond laser induced densification within cell-laden hydrogels results in cellular alignment, *Biofabrication* 11 (3), 035005 (2019)

*Reprinted as permitted by IOP Publishing, Inc. author agreement for personal use.

3.2 Introduction.

Extracellular matrix mimicking hydrogels have been widely used as model 3D culture systems to uncover underlying mechanisms of cell behavior occurring during development and disease [1-3]. In a typical experimental process flow, (i) cells are encapsulated within a biocompatible synthetic, semi-synthetic or natural hydrogel matrix, followed by (ii) biophysical and/or biochemical manipulation of the hydrogel environment in a controlled fashion, followed by (iii) assessment of the cellular responses by conventional microscopy techniques. Although a large number of research tools have been developed to manipulate hydrogel properties, ultrafast laser writing is the one of few methods capable of providing user-defined micro-to-nanoscale manipulation within a cell-laden hydrogel matrix [3-5].

Femtosecond (fs) laser induced multiphoton processing has been used to manipulate material properties within cell-laden hydrogels with minimal collateral damage to surrounding living cells [6-8]. Fs lasers have been used to immobilize growth factors and adhesive peptides and/or create biophysical voids and channels within cell-laden hydrogels to investigate fundamental cell behavior [2, 3, 9-14]. Also, fs laser writing combined with advances in orthogonal chemistry have also allowed the concurrent patterning of stiffness and temporal control over soluble factors to better complex *in vivo* environments. Fs laser based ablation and degradation of unmodified hydrogels and hydrogels modified with photo-cleavable groups respectively have allowed the *in situ* patterning of microchannels in the presence of living cells. This method

has been widely used to produce hollow micro-features within a range of hydrogels to spatially direct cell migration, guide multicellular organization to form neural and micro-vasculature networks, and engineer disease models with embedded fluid flows.

Although never reported in cell-laden hydrogels, fs laser writing within glass, polymers, silicone hydrogels, and BSA protein solutions have been reported to cause a change in refractive indices[15-17]. The change in RI, especially in glass and polymers has been exploited to create optical waveguides, diffraction gratings, and optical storage devices [10, 18, 19]. Although not fully understood, the underlying cause for a change in refractive indices in various materials have been attributed to crosslinking, material densification due to collapse of polymer chains, phase separation or changes in functional groups[20-23]. For the first time, we report that fs lasers can introduce material modification in form of ‘densification’ within the bulk of 3D cell-laden hydrogel constructs. We also report that all the cell types tested in this work sense the densified patterns and preferential align along micro-patterns, resulting in localized, user-defined and 3D cellular alignment.

3.3 Materials and Methods

3.3.1 Synthesis of GelMA, LAP photoinitiator, and prepolymer preparation.

Gelatin Methacrylate (GelMA) macromer was synthesized using a previously reported protocol[24]. Briefly, 10 g porcine skin gelatin (Sigma Aldrich, St. Louis, MO) was mixed in

200 ml phosphate buffered saline (PBS, Thermo Fisher Scientific), stirred at 45°C, and methacrylic anhydride was added to the solution and stirred for 3 h. After stirring, the mixture was dialyzed against distilled water for 1 week at 40°C to remove the unreacted groups from the solution. The dialyzed GelMA was lyophilized in a freeze dryer (Labconco, Kansas City, MO) for one week. Lithium phenyl-2,4,6-trimethylbenzoylphosphinate (LAP) was synthesized in a two-step process according to the literature. At room temperature and under argon, 2,4,6-trimethylbenzoyl chloride (4.5 g, 25 mmol) was added dropwise to continuously stirred dimethyl phenylphosphonite (4.2 g, 25 mmol). The reaction mixture was then stirred for 24 hours therefore an excess of lithium bromide (2.4 g, 28 mmol) in 50 mL of 2-butanone was added to the reaction mixture from the previous step which was then heated to 50 °C. After 10 min, a solid precipitate formed. The mixture was then cooled to room temperature, allowed to rest overnight and then filtered. The filtrate was washed with 2-butanone (3 × 25 mL) to remove unreacted lithium bromide and dried under vacuum to give LAP (6.2 g, 22 mmol, 88%) as a white solid. To prepare either 7% or 10% (w/v) GelMA, a stock solution was prepared by mixing 0.7 or 1g of freeze dried GelMA with 10 ml of deionized water (dissolved at 40°C), and 0.25% (w/v) UV photoinitiator lithium phenyl-2,4,6-trimethylbenzoylphosphinate (LAP) was added into the solution. GelMA pre-polymer solution was filtered (pore size=0.2 µm) and used within 2 hours after preparation.

3.3.2 Characterization of mechanical properties of GelMA constructs.

In-situ photo-rheometry was performed to observe the changes in the storage modulus (G') during UV exposure of specific duration of UV exposure[24]. A modified standard AR 2000 Rheometer (TA Instruments, New Castle, DE) fitted with a 45 deg reflective mirror and custom-made insert allowing for the attachment of a UV-light collimating tube from a UV lamp (output power 3.5 mW cm^{-2} , OmniCure S2000) [24, 25]. Samples were tested at 25°C and at 1 Hz under 1% strain using an 8 mm diameter bottom plate and 50 μL of prepolymer solution. Gap distance was set at 250 μm to match the height of the GelMA samples used in this study. Total test time was fixed at 10 minutes, with the UV light being turned on after 1 min for a specific duration (5s to 60s). To measure the elastic modulus of partially crosslinking GelMA samples, the following procedure was used. 50 μL of the GelMA prepolymer solution (7% w/v; 0.25% LAP) was pipetted into custom made PDMS wells (8mm diameter, 0.25 mm thickness) and exposed to UV light (output power 3.5 mW cm^{-2} , OmniCure S2000) for a range of predefined time (5 s to 60 s). The crosslinked samples were then transferred to the well plates and incubated in ultra-pure DI water and allowed to swell for 24 hrs. The storage (G') and loss (G'') modulus of the samples were measured at 0.5% strain for a range of 0.1-100 Hz. The linear regions for both moduli recorded between 1 Hz and 10 Hz were used to calculate the shear (G) and Elastic modulus (E). The Poisson's ratio (ν) was assumed to be 0.4 [26, 27]:

$$E = 2G(1 + \nu) \text{ where } G = \sqrt{G'^2 + G''^2} \quad (1)$$

3.3.3 Cell culture

Human umbilical vein endothelial cells (HUVECs) were maintained in Vasculife Basal Medium (Lifeline Cell Technology) supplemented with Vasculife VEGF LifeFactors Kit (Lifeline Cell Technology), 1% Penicillin/Streptomycin (P/S) on gelatin-coated flasks. Medium of HUVECs were changed every 2 days, and passage 4-9 were used for cell encapsulation studies. Mouse 10T1/2 fibroblasts were maintained in Basal Medium Eagle (BME, Gibco) supplemented with 10% Fetal Bovine Serum (FBS), 1% P/S and 1% Glutamax, and passage numbers below 17 were used for cell encapsulation studies. Mouse IDG-SW3 late osteoblasts were maintained in α -Modified Eagle Medium (α -MEM) supplemented with 10% FBS, 1% P/S, 1% Glutamax and 50 U/ml IFN- γ on rat tail type I collagen-coated flasks, and passage 5-15 were used for cell encapsulation studies. All cell lines in this work, except for mouse IDG-SW3 late osteoblast cell line, were cultured in a cell culture incubator in 5% CO₂ atmosphere at 37°C. IDG-SW3 late osteoblasts were cultured in 33°C incubator with 5% CO₂. The hiPSCs were maintained on 6-well plates coated with growth factor reduced Geltrex (Life Technologies, Ca# A1413302) in Essential 8 (E8) media (Life Technologies, Ca# A1517001). To start MSC differentiation, hiPSC were maintained in E8 for two additional days, and then induced for differentiation at “day 0” with differentiation media that consists of 10 ng/mL bFGF (R&D Systems Ca# 233-FB), 4 μ M SB431542 (Stemgent, Ca# 04-0010-10) and 4 μ M WNT agonist CHIR99021 (Stemgent, Ca# 04-2004) in Essential 6 (E6) media (Life Technologies, A1516401). Differentiation media was changed daily for the next 5 days. On day 6, the differentiated cells were plated as MSC Passage 0 (MP0) on a Geltrex coated 6-well plate in a

serum-free MSC culture media (CTS StemPro MSC SFM), (Life Technologies, A1033201) for continuous passages. After MP5, the differentiated cells gained the cellular morphology and molecular characteristics of MSCs. For alignment experiment in the GelMA hydrogel, hiPSC-MSCs were maintained in Dulbecco's Modified Eagle Medium (DMEM, Gibco) supplemented with 10% Fetal Bovine Serum (FBS), 1% P/S and 1% Glutamax on attachment factor protein (Gibco)-coated flasks, and passage 10-15 were used for encapsulation.

3.3.4 Femtosecond laser writing setup.

Custom-built fs-laser platform was designed and built by combining a Ti:Sapphire fs laser (Coherent, Chameleon, USA) with a Zeiss Microscope (Observer Z1, Germany) (**SI-1**). In this setup, a 730nm femtosecond laser beam with a repetition rate of 80 MHz was passed through an isolator that prevented back scattering. A $\lambda/2$ waveplate in combination with a Glan-Taylor polarizer was used to control laser power, measured by a power meter (Newport, USA). Two biconvex lens were used to expand the beam to fill the back aperture of the objective lens. A pinhole was used to filter out diffraction noise at the periphery of the beam. An objective 20 \times (Zeiss, Germany) was used to process GelMA samples. A filter (Semrock, USA) was used to block out the UV spectrum of the illumination light source to avoid any crosslinking effects on GelMA samples. This setup was used to introduce patterns in the center or the mid-point of both GelMA and cell-laden GelMA samples. User-defined patterns were designed using AutoCAD and then converted to visual basic code. Line patterns were written at varying speeds

and laser powers using a custom written algorithm that controls the stage and laser shutter based on a computer-generated design. Patterns were visualized in real time under bright-field and contrast microscopy. In this work, laser dosage (E) was defined as

$$E = \text{Intensity} \times \text{Time} \quad (2)$$

where laser intensity, $I = \frac{P}{\pi R^2}$, exposure time, $T = \frac{2R}{V}$, airy radius of laser beam, $R = \frac{0.61\lambda}{NA}$, P is the average power measured by a power-meter right before the objective, V is the stage scanning speed, λ is the wavelength of fs laser and NA is the numerical aperture of the objective.

3.3.5 Fs-laser modifications within cell-laden GelMA

Prior to encapsulation, cells (1×10^6 cells/ml) were trypsinized, counted and mixed with 10% GelMA (w/v) pre-polymer solution and 0.36% LAP photoinitiator, to achieve a final concentration of 7% GelMA with 0.25% LAP. The cell-laden pre-polymer solution (20 μ l) was pipetted between glass slide and methacrylated glass coverslip (spacing=250 μ m) (SI-1). UV light was exposed at a power of 3.5 mW/cm² for 5 seconds to obtain partially crosslinked cell-laden GelMA samples. Femtosecond laser writing system was then used to write user-defined patterns (10 lines per pattern) at the center of the GelMA samples. Patterns were written at varying depths of the sample, while keeping the laser power and speed constant. (800mW, 50 μ m/s). The ability to introduce laser-based modification during ongoing cell culture was demonstrated using IDG-SW3-laden GelMA samples. In this experiment, cell encapsulated was performed on Day 0, followed by introduction of densified lines after 24 hours. All samples

were cultured in 12-well-plates (Fisher Scientific) under standard culture conditions (37°C, 5% CO₂) using the specific media for each cell type. The media were changed every 2 days.

3.3.6 Quantification of cellular viability and alignment

Viability of cells were determined using a Live/Dead Assay Kit. Samples were incubated in calcein AM and ethidium homodimer (Invitrogen) at concentration of 0.5 µl/ml and 2 µl/ml, and fluorescence microscope (Nikon Eclipse Ti) was used to determine cell viability using ImageJ software. To determine cellular morphology, samples were stained for f-actin and nuclei. At pre-determined time-points, cells were fixed with 4% formaldehyde (Invitrogen, Carlsbad, CA) for 30 minutes, soaked in 2% Triton X-100 in DPBS for 30 minutes, and subsequently stained with phalloidin (Alexa-Fluor 568, Invitrogen) (1/100 dilution in DPBS) (45 mins at RT) and with 1.25 µg/ml DAPI (Life Technologies) (5 mins at RT) to visualize f-actin and cell nuclei respectively. In another experiment, Cytochalasin D, a known inhibitor of actin dynamics, was added to the media of selected 10T1/2-laden GelMA samples (0.25 µg/ml) on day 0 or day 3 and these samples were fixed on day 3 and day 6 respectively, before immunostaining them for DAPI and phalloidin. Cell images were taken by inverted microscope (Nikon Eclipse Ti) and quantified using ImageJ software. The cell nuclei orientation was defined as the orientation of the major axis of individual nuclei with respect to the densified line patterns. Nuclei orientation angle less than 10° was identified as completely aligned cells. The nuclear shape index ($\text{circularity} = 4 \cdot \pi \cdot \text{area} / \text{perimeter}^2$), an indicator of the shape of the

cells, was also measured. The shape index of 1 was designated as a perfectly circular cell, while a decrease in the shape index was used to assess cellular elongation.

3.4 Results

3.4.1 Laser induced material modifications within partially crosslinked GelMA.

Fs laser direct writing system was used to introduce material modifications in form of line patterns within partially crosslinked GelMA in a two-step process (**Fig. 3.1A, SI-3.1**). In the first step, a liquid prepolymer GelMA solution (7% or 10%), with 0.25% LAP photoinitiator, was pipetted between methacrylated glass coverslip and glass slide, and exposed to UV light (365nm, 3.5mW cm⁻²) for varying amount of UV times to obtain a GelMA samples of thickness 250μm. Upon UV exposure, GelMA crosslinking begins to occur through the conversion of the methacrylate double bond into covalent bonds, indicated by an increase in storage and elastic modulus (**SI-3.2**). In the second step, focused fs-laser was used to introduce line patterns at the center of a 250μm thick GelMA sample with increasing laser dosage. To increase laser dosage, the scanning speed was varied while maintaining a constant laser intensity. Based on the absorption spectra of GelMA, a wavelength of 730nm was used to introduce material modifications using two-photon absorption at the fs-laser focus. (**SI-3.3**),

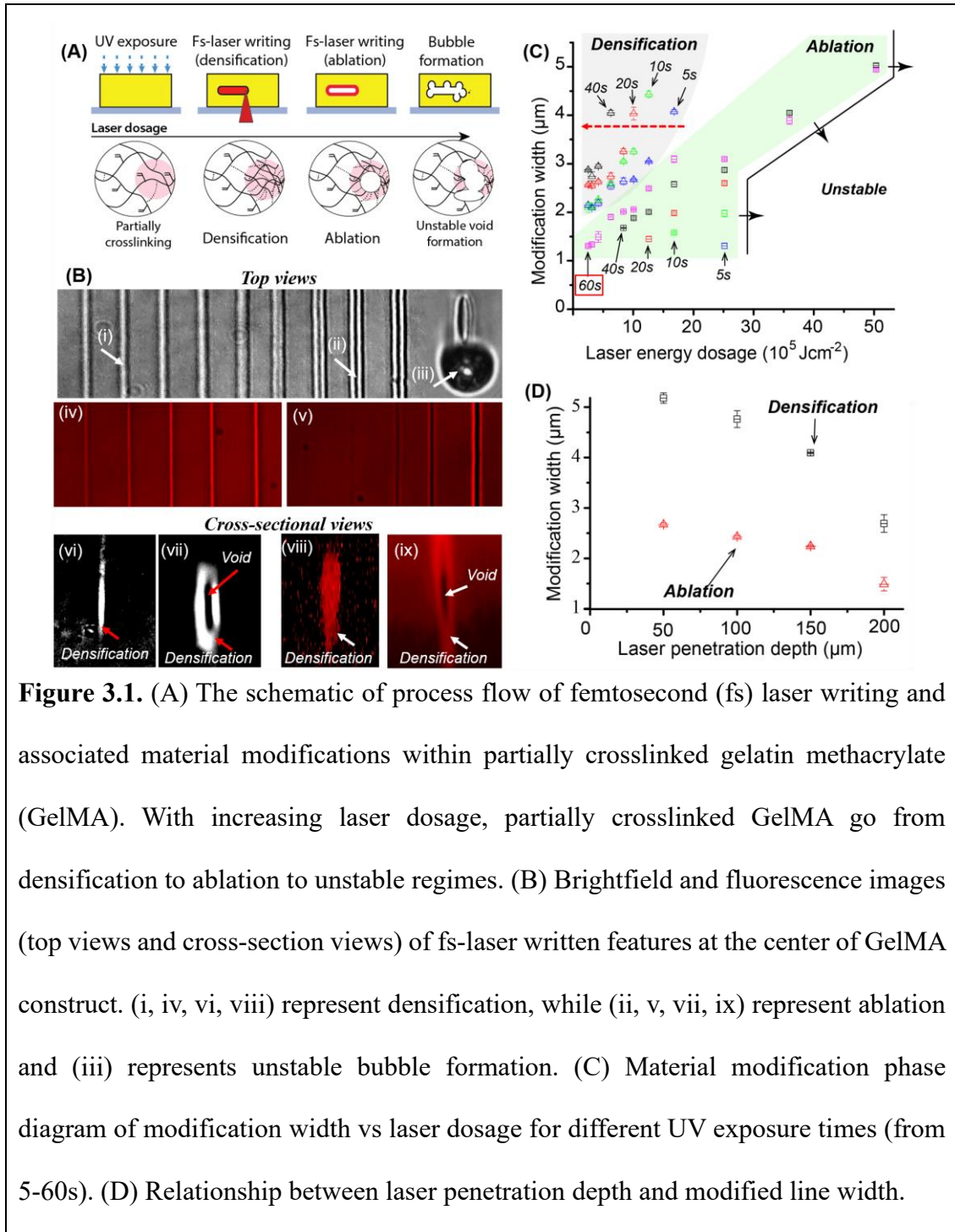


Figure 3.1. (A) The schematic of process flow of femtosecond (fs) laser writing and associated material modifications within partially crosslinked gelatin methacrylate (GelMA). With increasing laser dosage, partially crosslinked GelMA go from densification to ablation to unstable regimes. (B) Brightfield and fluorescence images (top views and cross-section views) of fs-laser written features at the center of GelMA construct. (i, iv, vi, viii) represent densification, while (ii, v, vii, ix) represent ablation and (iii) represents unstable bubble formation. (C) Material modification phase diagram of modification width vs laser dosage for different UV exposure times (from 5-60s). (D) Relationship between laser penetration depth and modified line width.

During the fs-laser writing experiments, two material modification regimes, densification and ablation, were identified (**Fig.3.1**). In the densification regime, fs laser writing at lower laser dosage drives two photon crosslinking of partially crosslinking GelMA by conversion of free

acrylate groups into covalent double bonds. Further increase in laser dosage likely results in collapse and compaction of GelMA chains resulting in a densified region, that appears brighter as compared to the rest of the GelMA (**Fig.3.1B**) To verify that ‘densification’ is different from ‘crosslinking’ of partially-crosslinked GelMA samples, the written lines were irradiated with UV lamp for 30mins to ensure complete crosslinking of GelMA. We found that modified lines written with fs-laser continue to be clearly identified under brightfield imaging and fluorescence imaging using Rhodamine B stained GelMA (**Fig.3.1B**), suggesting that densification of GelMA is not similar to fully-crosslinked GelMA.

Figure 3.1C shows the phase diagram for both densification and ablation processing regimes, with the width of the modified (densified or ablated) line on the X axis and increase in the laser energy dosage on the Y axis. Within the plot, pink, black, red, green, and blue color symbols represent UV exposure times of 60, 40, 20, 10 and 5 seconds respectively. Changes in UV exposure times influence the degree of partial crosslinking of GelMA samples before a focused fs laser is irradiated within the samples. In the densification regime, the width of the densified lines increase exponentially with an increase in laser dosage (**Fig.3.1C**). With an increase in UV exposure time from 5s to 40s, the required laser dosage is decreased for achieving same width of densified lines, indicated by a shifting of the densification curve towards the left (**Red dashed arrow in Fig.3.1C**). This result implies that during the fs laser writing step, the energy is initially utilized to crosslink partially crosslinked GelMA before being used for densification.

For samples with higher degree of crosslinking (higher UV exposure times), the ‘densification’ regime becomes narrower (UV times of 5-40s). For fully crosslinked samples (UV time of 60s) (SI-3.2), densification disappears completely and material modification shift to the ablation regime (**Red square in Fig.3.1C**). This implies that some degree of partial crosslinking is a necessary condition for densification to occur.

In the ablation regime, increase in laser dosage causes an ablation of a void surrounded by a densified shell (**Fig.3.1B**). In this regime, the channel width increase linearly with fs laser dosage (**Fig.3.1C**). For a fully crosslinking sample (UV time-60s), ablation occurs even at lower laser dosage, while for partially crosslinked samples (40s, 20s, 10s and 5s), laser energy is initially utilized for crosslinking and densification processes, before being utilized for the ablation process. This explains the left shift in the ablation curve with an increase in UV time which corresponds to an increase in partial crosslinking of GelMA. Beyond a critical value of fs-laser dosage, bubble formation is observed depicted as ‘unstable’ (**Fig. 3.1C**). Modification widths in both densification and ablation regimes decreases with increasing laser focus depth within the GelMA samples possibly due to scattering losses (**Fig. 3.1D**). In summary, an increase in the laser dosage within partially crosslinked GelMA leads to continuous material modifications from fully crosslinking to densification to ablation to unstable bubble formation.

3.4.2 Influence of fs-laser induced densification on cell behavior.

In this work, we choose to investigate the influence of fs-laser induced densification on cell behavior. Densified lines were introduced within cell-laden GelMA samples, and cellular viability and morphology of encapsulated cells were characterized. Densified line patterns (width~3 μ m; spacing 50 μ m) were written at the center of 7% GelMA constructs (UV exposure times of 5s) containing human endothelial cells (HUVECs). Cell viability of encapsulated HUVECs was assessed using a standard live/dead assay (**Fig.3.2B**). Results demonstrate no significant differences between laser modified and non-modified control samples. We also found little to no cell death directly above and below the written lines, indicating the highly localized influence of the two-photon writing process. To characterize the morphology of encapsulated cells, HUVECs were encapsulated within 7% GelMA constructs at a cell density of 1 M/ml using a UV exposure time of 5s, and nuclei alignment was measured using immunostaining and ImageJ analysis.

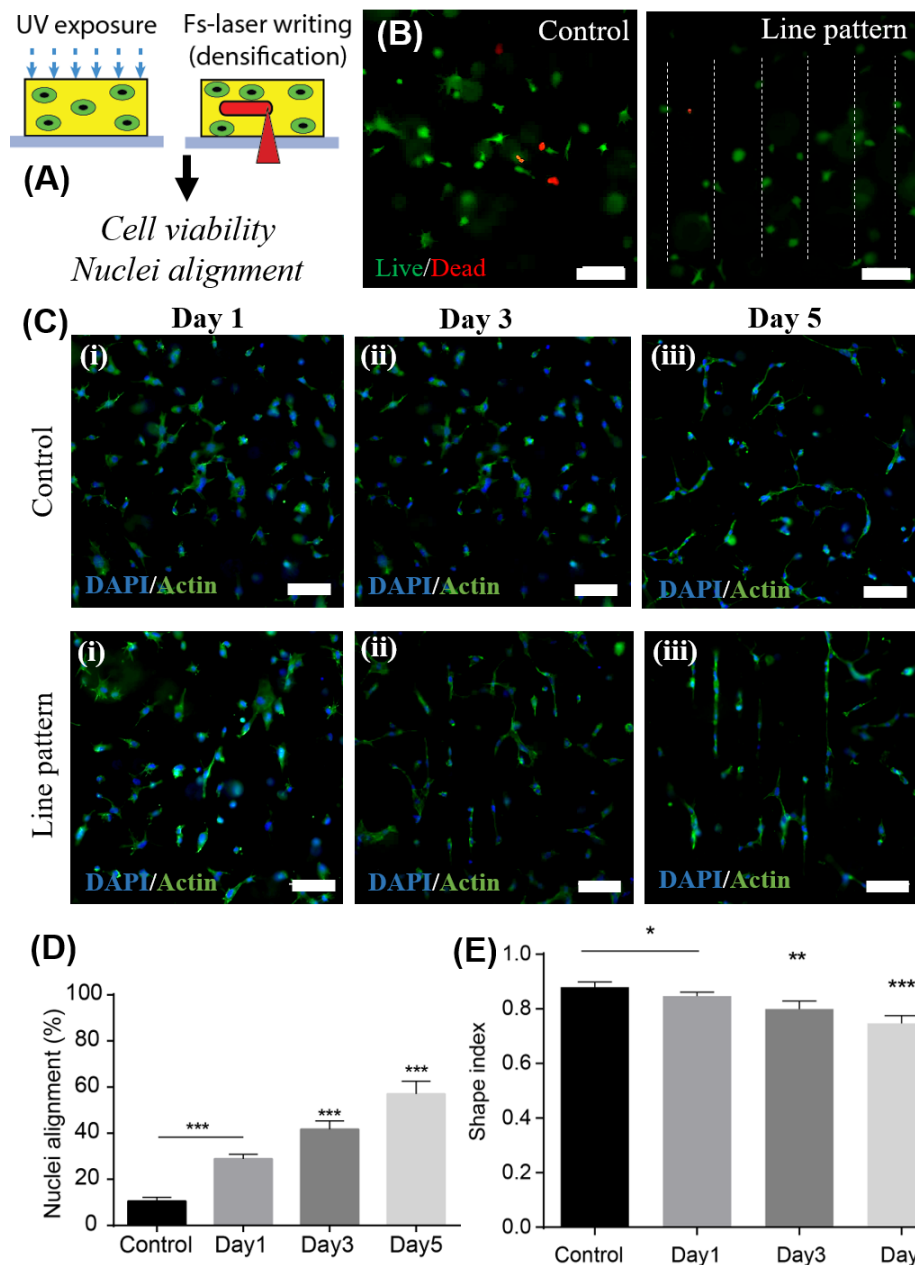
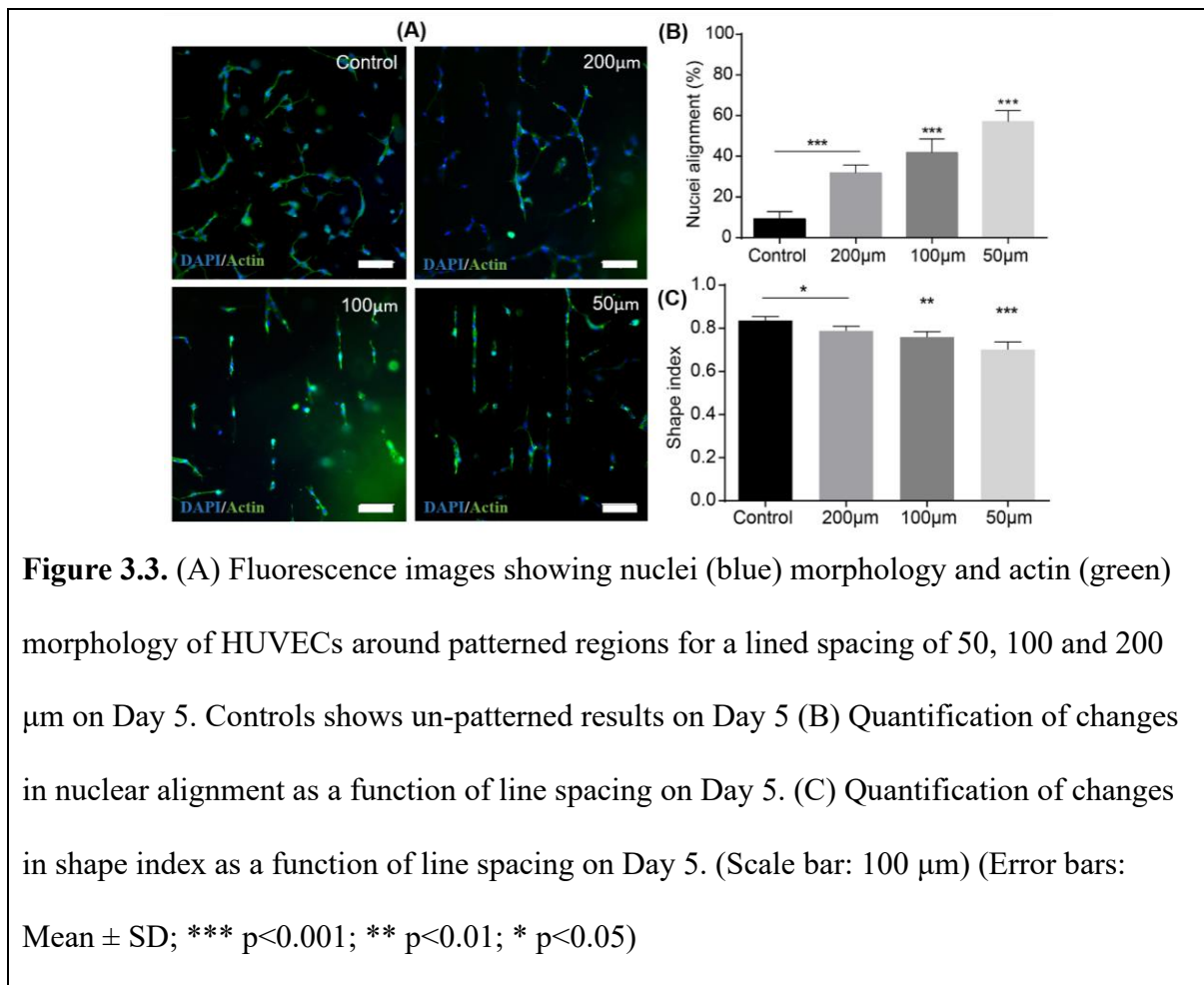


Figure 3.2. (A) Schematic of experimental design; cell-laden GelMA was partially crosslinked using a UV exposure time of 5s, followed by fs laser writing of densified line patterns at the center of the samples. (B) Characterization of cell viability 24hrs after fabrication using a live (green)-dead (red) assay. (Line spacing-50μm, dashed white lines) (C) Fluorescence images showing nuclei (blue) and actin (green) morphology of HUVECs

around un-patterned and patterned regions on (i) Day 1, (ii) Day 3 and (iii) Day 5. (D) Plot of nuclear alignment vs days in culture for patterned regions for a line spacing of 50 μm . (D) Plot of nuclear shape index vs days in culture for patterned regions for line spacing of 50 μm . (Scale bar: 100 μm) (Error bars: Mean \pm SD; *** $p < 0.001$; ** $p < 0.01$; * $p < 0.05$) Controls shows un-patterned results on Day 5

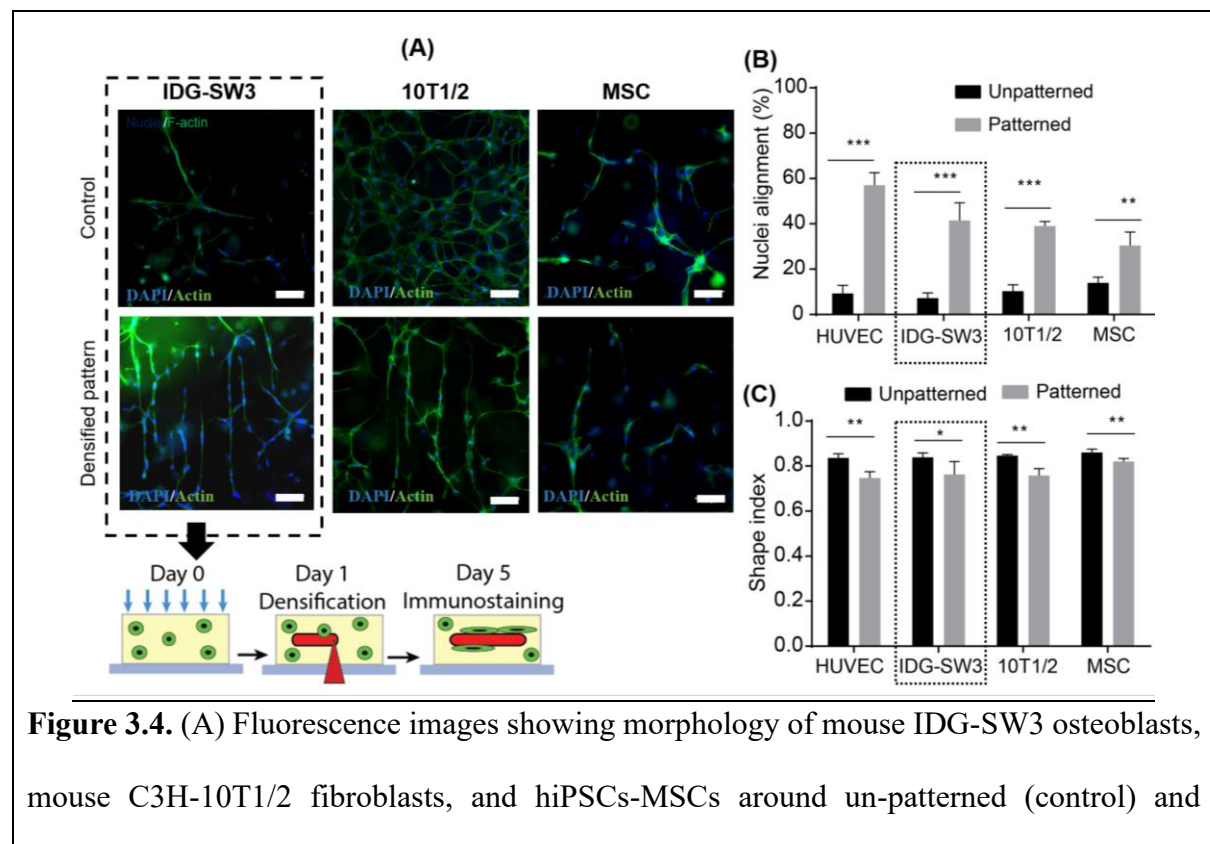


Briefly, cells whose nuclei orientation lie within 10° of the orientation of the fs-laser densified lines were considered aligned, and the degree of alignment was plotted in form of histograms displaying the relative percentage of aligned cells normalized with the total number of cells.

After 24 hours of culture, HUVECs near the densified lines start to spread. By day 3, they align along the direction of the densified lines, and the degree of alignment increases by day 5 (**Fig.3.2C**). Results show that for 50 μ m line spacing, percentage of cell alignment increase from $28.89\pm 2\%$ on day 1, to $41.74\pm 3.65\%$ on day 3, to $57.02\pm 5.51\%$ on day 5 respectively as compared to un-patterned control ($10.56\pm 1.63\%$) (**Fig. 3.2D**). Similar trend of an increase in nuclei alignment as a function of culture time can also be observed for 100 μ m and 200 μ m line spacing (data not shown). Nuclear shape index, that assumes values between 1 for ideal circular shape and decreasing values for elongated morphology, decreased as a function of culture time (**Fig. 3.2E**). The spacing between densified lines also influenced the degree of cell alignment. For day 5, as line spacing increases from 50 μ m to 200 μ m, the cell alignment drops from $57.02\pm 5.51\%$ to $31.92\pm 3.79\%$, although even with 200 μ m spacing, cell alignment is still significantly higher than control group (**Fig.3.3B**). Nuclear shape index also decreased with increased line spacing (**Fig.3.3C**). To investigate whether f-actin is involved in preferential cell alignment along densified lines, cytochalasin D (CytoD), a widely used inhibitor of actin dynamics, was introduced into the culture system at day 3 and day 6. Results show that cell alignment is inhibited in both cases as compared to control patterned group (**SI-3.4**). More work needs to be undertaken to elucidate the underlying mechanism related to localized nuclei elongation, and its influence on overall cell function.

3.4.3 Design flexibility of densification induced cell alignment method.

Densification induced cell-alignment across cell types. To test whether densification induced cellular alignment can be extended to other cell types, cell-laden GelMA samples were prepared using mouse 10T1/2s fibroblasts, mouse IDG-SW3 osteocytes, and human induced pluripotent stem cells-derived mesenchymal stem cells (hiPSC-MSCs). Similar to what we observed with HUVECs, results show that patterned regions show significantly higher percentage of cellular alignment for IDG-SW3 ($41.47 \pm 7.79\%$; $p < 0.001$), 10T1/2s ($39.07 \pm 1.96\%$; $p < 0.001$), and hiPSCs-MSCs ($30.45 \pm 5.94\%$; $p < 0.01$), as compared to the unpatterned regions (**Fig. 3.4**). A corresponding decrease in the mean nuclear shape index was also measured, which demonstrates a significant increase in cellular elongation along the patterned regions.

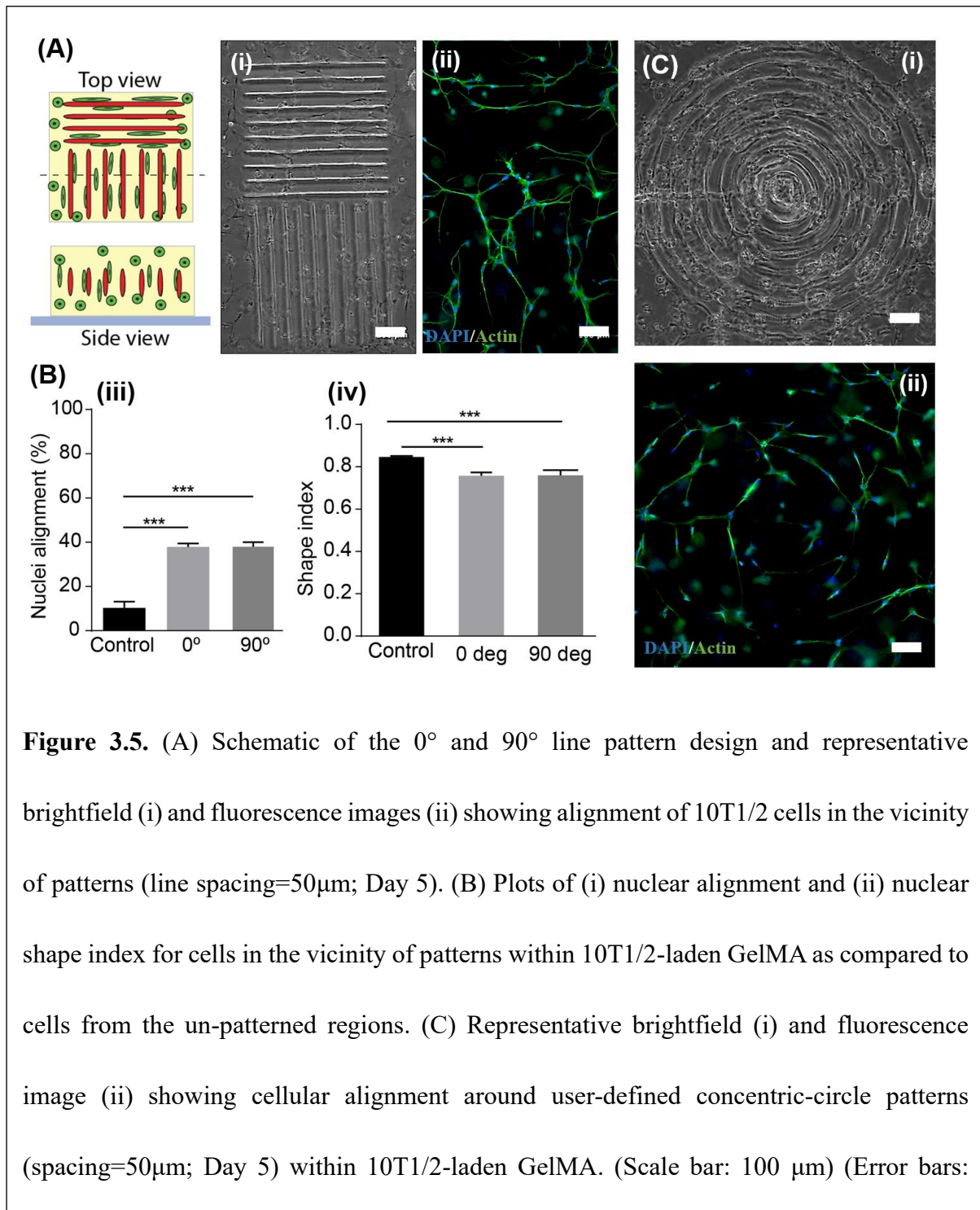


patterned regions on Day 5. (B) Characterization of changes in nuclear alignment between un-patterned and patterned regions for all cell types (line spacing=50 μ m; Day 5). Dashed square: IDG-SW3 were encapsulated on Day 0, cultured for 24 hrs, before introducing densified line patterns on Day 1, and immunostaining was performed on Day 5. For all other cells, densified lines were written on Day 0, and immunostaining was performed on Day 5. (C) Plot of nuclear shape index of different cell types for a pattern spacing of 50 μ m. (Scale bar: 100 μ m) (Error bars: Mean \pm SD; *** $p < 0.001$; ** $p < 0.01$; * $p < 0.05$)

Temporal flexibility of *in situ* densification. To demonstrate that densified lines can be introduced at any point during an active cell culture experiment, IDG-SW3-laden GelMA was prepared on Day 0, and densified line patterns were introduced on Day 1. Results show an increase in cellular alignment on day 5, demonstrating the temporal flexibility of this method to introduce physical guidance cues during active cell culture. (Dashed box in **Fig.3.4**).

Densification to align cells along user-defined directions. To demonstrate that laser-induced densification can be used to align encapsulated cells in any user-defined arbitrary alignment configurations, two experiments were conducted. The first experiment introduced two sets of densified lines (spacing-50 μ m) with 0° and 90° orientations adjacent to each other within a 10T1/2-laden GelMA (**Fig. 3.5A, B**). Direct written densified lines in 0° and 90° patterns do not overlap and they both are in the same plane at the center of the GelMA sample. Results showed significantly higher cellular alignment along 0° (37.61 \pm 1.62%) and 90° (37.72 \pm 2.04%) as compared to cell alignment in un-patterned regions (10.31 \pm 2.81%). Nuclear shape index demonstrated an increase in cellular elongation along 0° and 90° orientations compared with

un-patterned controls. The second experiment introduced densification in the form of a concentric circle pattern within 10T1/2-laden GelMA. Cells align remarkably well to the densified pattern, demonstrating that laser-induced densification can be used to align cells along any arbitrary paths (**Fig. 3.5C**). SI-3.6 shows other complicated patterns that can be generated using this technique.



Influence of out-of-plane densification on cell alignment. To assess the zone of influence of densified structure in the z-direction, images were taken at different z-planes above and below the focal plane of the densified line patterns for cell-laden samples. We observed that

densification of GelMA can only influence cell alignment in a z-range of about $60\mu\text{m}$ ($\pm 30\mu\text{m}$ on either side) (**Fig.3.6A**). We also observe higher cell spreading in layers closer to the top surface (surface closer to the nutrients), possibly explained by differences in nutrient diffusional limitations at varying depths. To evaluate how sample thickness influences the spreading and alignment of cells, densified line patterns were written at a depth of $80\mu\text{m}$ and $160\mu\text{m}$ with a line spacing of $50\mu\text{m}$. After 21 days of culture, cells within layer 1, closer to the surface, showed significant spreading as compared to cells in the vicinity of layer 2. Although the overall cellular alignment in layer 2 is much lower than layer 1 (**Fig.3.4B**), cells that are physically closer to the densified lines are elongated with close to 100% nuclear alignment. Encapsulated cells between layer 1 and 2 (depth range of $100\text{--}140\mu\text{m}$) do not show any influence of either densified layers, confirming localized influence even in multilayer pattern format.

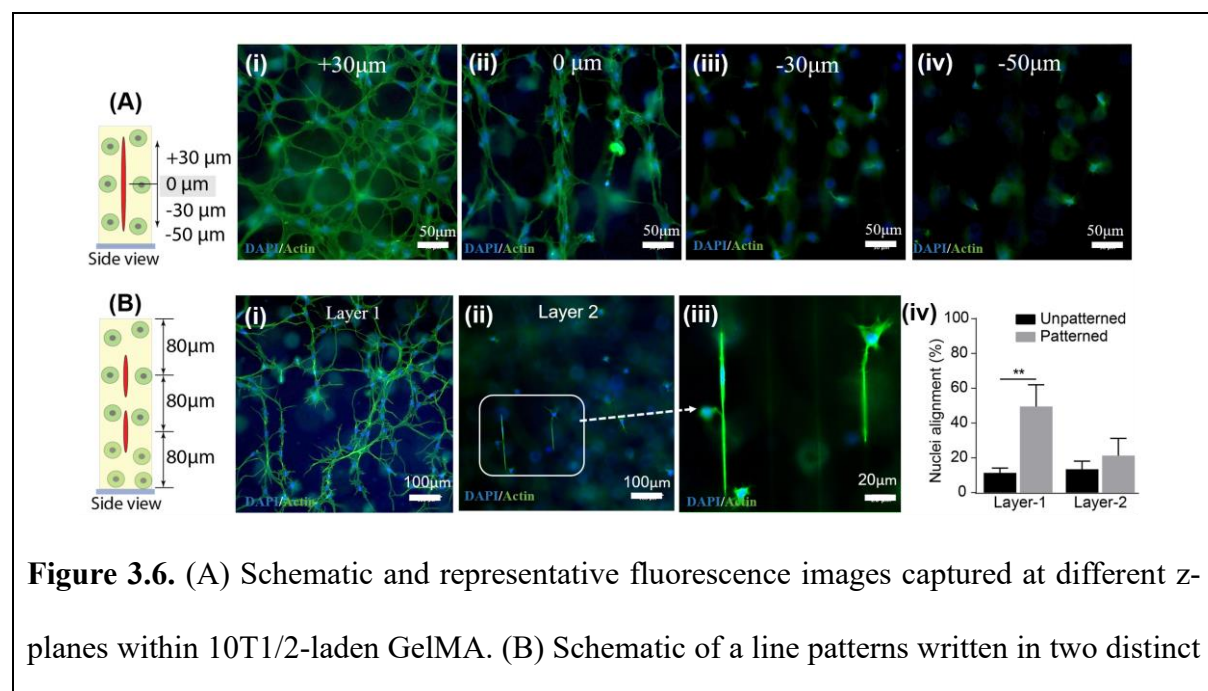
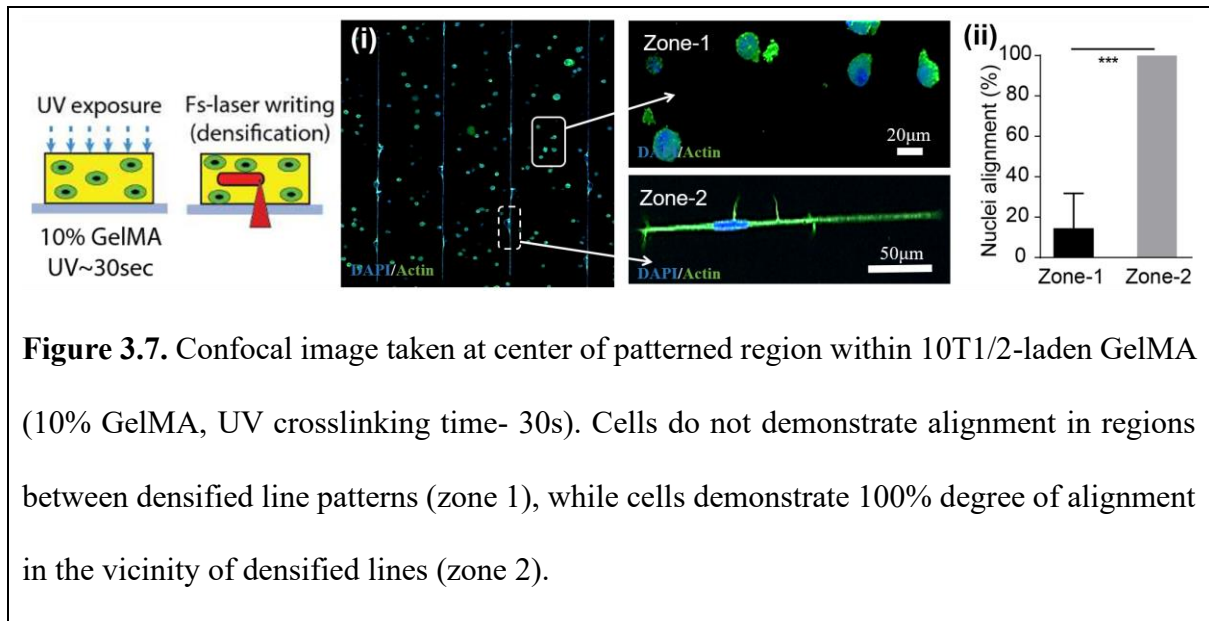


Figure 3.6. (A) Schematic and representative fluorescence images captured at different z-planes within 10T1/2-laden GelMA. (B) Schematic of a line patterns written in two distinct

layers. Fluorescence images from (i) layer 1 (80 μ m from the top surface), and (ii, iii) layer 2 (160 μ m from the top surface). (iv) Plot shows differences in nuclei alignment between layers 1 and 2 from un-patterned and patterned regions. (Error bars: Mean \pm SD; *** p<0.001; ** p<0.01)

Influence of GelMA stiffness on densification induced cell alignment. To assess the influence of global stiffness on cell alignment, we compared cell alignment results from 7% GelMA (2.27 \pm 1.29kPa) and 10% GelMA (8.71 \pm 1.64kPa) irradiated with the same UV exposure time of 30s. (SI-3.7) The higher global modulus of GelMA resulted in almost 100% degree of nuclei alignment for encapsulated 10T1/2s close to the densified line patterns (zone 2). Cells even 20 μ m away from the densified lines showed no nuclei alignment (zone 1) (**Fig. 3.7**). The overall cell spreading of 10% GelMA (30s) is limited as compared to both 7% GelMA (30s from SI-3.7, and 5s from Fig.3.4A). Thus, it is clear that global stiffness of GelMA prior to fs-laser densification also influences the cellular response.



3.5 Discussion

Femtosecond (fs) laser are capable of introducing internal modifications within transparent materials due to their unique nonlinear two-photon absorption property. In this work, we report material modification in form of densification within GelMA. Previously, fs laser writing has shown densification phenomenon within glass, polymers, silicone hydrogels and BSA protein solutions. In both silica and PMMA polymer, densification was linked to a change in refractive index[16, 21]. Similar to these report, we hypothesize that thermal accumulation induced by high repetition rate pulsed laser (80 MHz) results in the localized possible collapse and entanglement of chains at the laser focus within GelMA resulting in material densification that can be visualized by a change in refractive index [28]. researchers have hypothesized that the accumulated effect of the fs laser pulses results in additional localized crosslinking in the polymer network that expels water in the laser focus, causing localized densification of the hydrogel and a corresponding increase in the local refractive index.

In the ablation regime, we observe a void surrounded by a densified shell within GelMA hydrogel. This result also aligns well with similar studies with glass, silica and some thermoplastics that have demonstrated the presence of shockwaves and densified shell formation around voids[29]. Brightfield images clearly show the presence of a dark center line surrounded by a bright region and adjoining darker regions (**Fig. 3.1B**) that point to the creation of compaction and rarefaction waves during laser writing process.

Although there are no papers describing laser interaction with gelatin or GelMA, work related to the interactions of femtosecond (fs) lasers with high-water content hydrogels and silica glass materials has been reported. Upon fs laser irradiation, change in optical property such as refractive index within hydrogels has been reported [18, 30, 31]. Recently, laser induced the densification that results in the volume contraction of the BSA hydrogel and changes in topography was also reported [32]. Using silica glass materials, several groups have reported an increase in material density with modification of local refractive indices upon fs laser irradiation. Changes in refractive index have been attributed to the generation of shockwaves[33], the formation of color centers[34], and structural material modifications[35]. For hydrogels materials, the above mentioned phenomenon could also occur, however the exact mechanism of densification within hydrogel materials including naturally-derived GelMA is currently not understood.

Fs laser enabled material modifications within synthetic, semi-synthetic and natural hydrogels have been used to investigate fundamental cellular responses such as adhesion, migration, alignment and differentiation. In this work, we found that fs laser induced densification material modification within cell-laden GelMA is able to provide preferential localized control over cellular alignment within GelMA, a widely used naturally derived hydrogel. This is a new method to align cells in arbitrary patterns within cell-laden hydrogels. Previously, inspired by

the native extracellular matrix (ECM), significant research has been directed towards controlling the spatial alignment and organization of cells [36-39]. Although 2D micro/nano-patterns are widely used to align cells, controlling the organization of cells within a 3D hydrogels remains a challenge [38, 40]. Large scale or global alignment of cells within gels have been achieved via (i) partially constrained with matrigel or collagen gels [41, 42], (ii) use of external stimuli such as mechanical stretch[43], electrical impulse [44] and flow induced shear stress[45], or (iii) micropatterning using PDMS-mold with parallel grooves[40, 46]. All these methods involve complicated processing steps and do not provide local and/or user-defined control over cellular alignment. Two photon laser processing have also been used to pattern cell adhesive ligands within 3D gels to direct cellular migration and alignment [7], however this method requires specialized hydrogels, and are limited by low hydrogel-adhesive ligand conjugation efficiency. The densification approach does not require specialized chemical modification (photo-labile groups) [3, 13], inclusion of nanoparticle for enabling two-photon induced thermal degradation of micro-channels within hydrogels [12], or any external stimulation or guidance systems. The fs-laser enabled densification method allows the introduction of patterns during active cell culture providing temporal design flexibility. Fs-laser densification can be potentially a new tool to recreate localized variations in stiffness of 3D extracellular matrix by fs-laser densification. This will be important in elucidating new mechanisms of metastasis, as well as migratory behaviors during wound healing and development that have been shown to be

influenced by spatial and localized variations in matrix stiffness [47-49]. This novel method could be used to investigate cell behavior within 3D hydrogel systems.

3.6 Conclusion

In this work, we report a new material modification phenomenon coined as ‘fs-laser induced densification’ within widely used GelMA hydrogels. It was found that introduction of densified line-patterns within cell-laden GelMA resulted in preferential and localized cellular alignment. This method is capable of aligning variety of encapsulated cells in user-defined patterns. We show that densified patterns can be introduced during ongoing cell culture experiments. This first report of physical densification within cell-laden GelMA can be potentially extended to study cell behavior within a range of other photosensitive hydrogels.

3.7 Supplemental Information

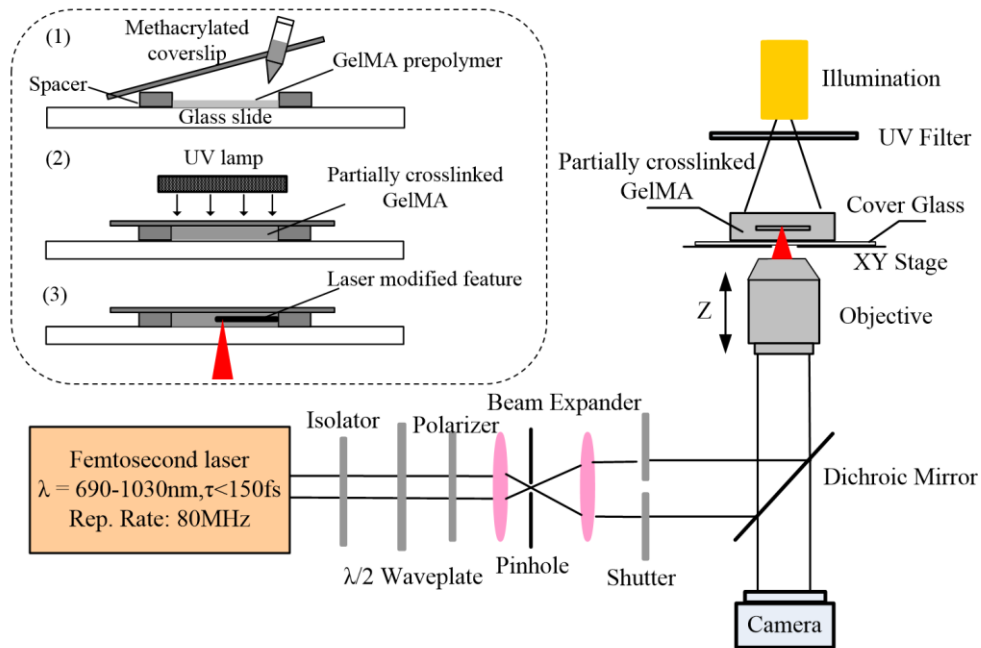


Figure SI-3.1: The experimental setup was integrating the femtosecond laser with an inverted microscope. The inset shown the steps of laser modification including (1) cell-laden prepolymer (2) partially crosslinking (3) laser processing.

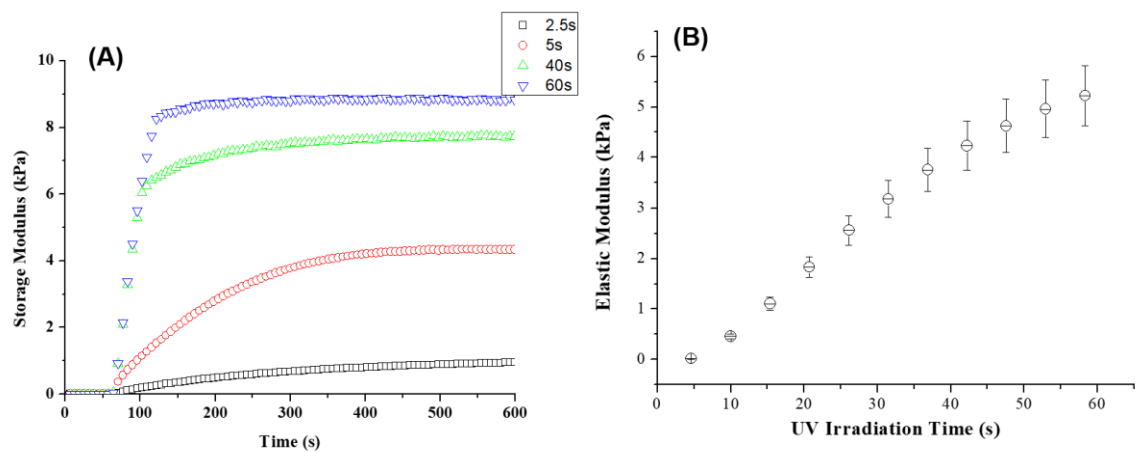


Figure SI-3.2 (A) Real-time changes in storage modulus for GelMA samples with varying UV exposure times, and (B) elastic modulus of partially crosslinking GelMA samples (UV time=2.5s, 5s, 10s, 20s, and 40s) and fully crosslinked GelMA samples (60s) after one day of incubation in DI water.

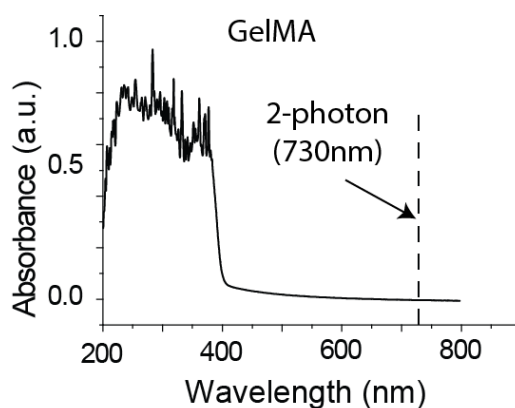


Figure SI-3.3 Absorption spectrum of GelMA prepolymer mixed with LAP photoinitiator.

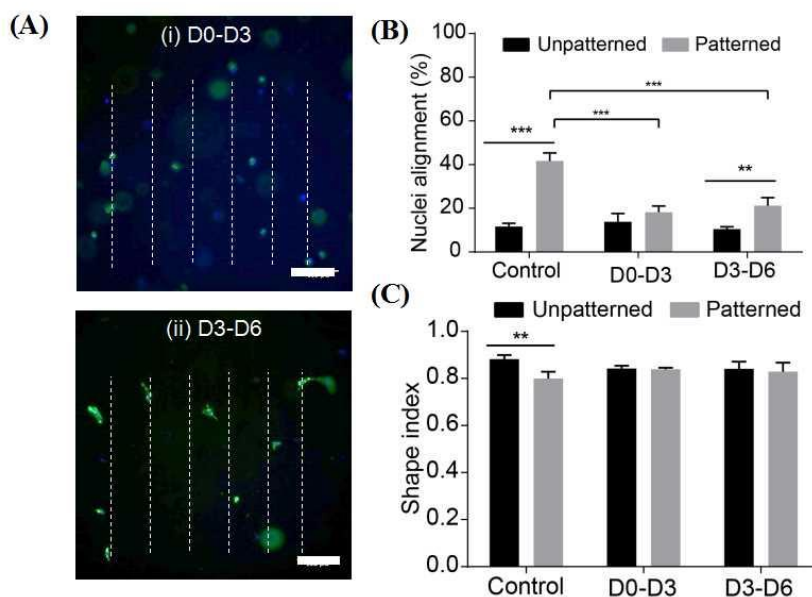


Figure SI-3.4 Quantification of nuclei alignment after additions of CytoD (inhibitor of actin dynamics), at different time points during active cell culture. (A)-(i) D0-D3: CytoD was added on Day 0, and image was obtained on Day 3, (A)-(ii) D3-D6: CytoD was added on Day 3 and

image was obtained on Day 6. (B) Plots of nuclear alignment after addition of actin dynamics inhibitor. (C) Nuclear shape index after addition of actin dynamics inhibitor, CytoD. (Scale bar: 100 μ m) (Error bars: Mean \pm SD; *** $p < 0.001$; ** $p < 0.01$)

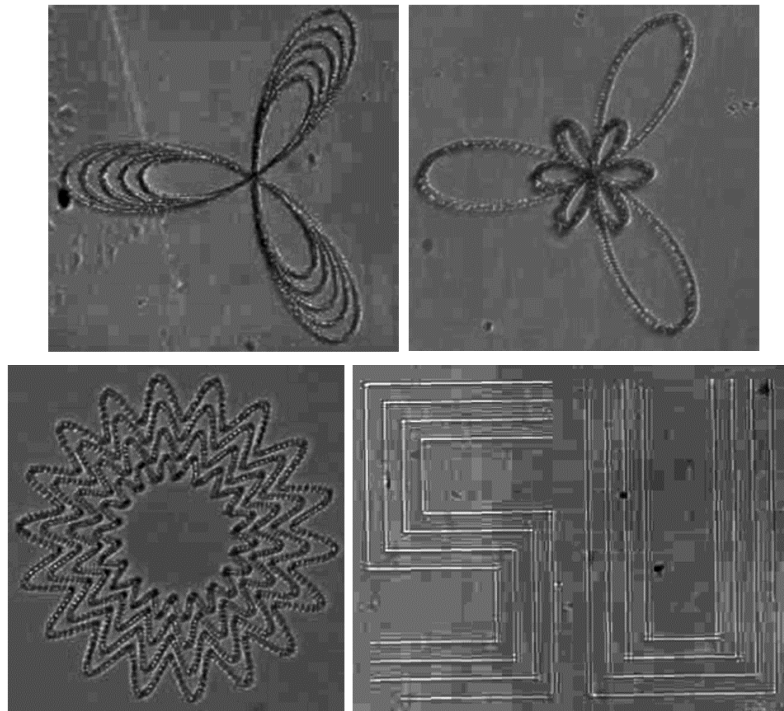


Figure SI-3.5 Complex user-defined patterns can be densified within GelMA samples.

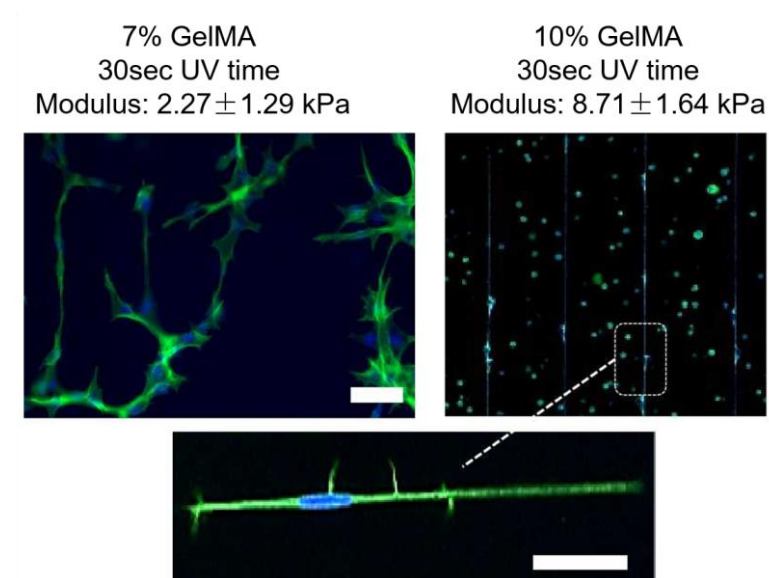


Figure SI-3.6 (A) Cellular alignment within 7% GelMA and (B) 10% GelMA under the same UV irradiation time of 30s (Scale bar: 50 μ m)

3.8 References

- [1] Edmondson R, Broglie JJ, Adcock AF, Yang L. Three-dimensional cell culture systems and their applications in drug discovery and cell-based biosensors. *Assay and drug development technologies* 2014;12:207-18.
- [2] Tam RY, Smith LJ, Shoichet MS. Engineering cellular microenvironments with photo-and enzymatically responsive hydrogels: Toward biomimetic 3D cell culture models. *Accounts of chemical research* 2017;50:703-13.
- [3] Pradhan S, Keller KA, Sperduto JL, Slater JH. Fundamentals of Laser-Based Hydrogel Degradation and Applications in Cell and Tissue Engineering. *Advanced healthcare materials* 2017.
- [4] Ovsianikov A, Mironov V, Stampfl J, Liska R. Engineering 3D cell-culture matrices: multiphoton processing technologies for biological and tissue engineering applications. *Expert review of medical devices* 2012;9:613-33.
- [5] Thiele J, Ma Y, Bruckers SMC, Ma S, Huck WTS. 25th anniversary article: designer hydrogels for cell cultures: a materials selection guide. *Advanced materials* 2014;26:125-48.
- [6] Sima F, Sugioka K, Vázquez RM, Osellame R, Kelemen L, Ormos P. Three-dimensional femtosecond laser processing for lab-on-a-chip applications. *Nanophotonics* 2018;7:613-34.

- [7] Lee S-H, Moon JJ, West JL. Three-dimensional micropatterning of bioactive hydrogels via two-photon laser scanning photolithography for guided 3D cell migration. *Biomaterials* 2008;29:2962-8.
- [8] Vogel A, Noack J, Hüttman G, Paltauf G. Mechanisms of femtosecond laser nanosurgery of cells and tissues. *Applied Physics B* 2005;81:1015-47.
- [9] Culver JC, Hoffmann JC, Poché RA, Slater JH, West JL, Dickinson ME. Three-dimensional biomimetic patterning in hydrogels to guide cellular organization. *Advanced materials* 2012;24:2344-8.
- [10] Gattass RR, Mazur E. Femtosecond laser micromachining in transparent materials. *Nature photonics* 2008;2:219.
- [11] Seliktar D. Designing cell-compatible hydrogels for biomedical applications. *Science* 2012;336:1124-8.
- [12] Hribar KC, Meggs K, Liu J, Zhu W, Qu X, Chen S. Three-dimensional direct cell patterning in collagen hydrogels with near-infrared femtosecond laser. *Scientific reports* 2015;5:17203.
- [13] Tibbitt MW, Kloxin AM, Dyamenahalli KU, Anseth KS. Controlled two-photon photodegradation of PEG hydrogels to study and manipulate subcellular interactions on soft materials. *Soft Matter* 2010;6:5100-8.
- [14] Brandenburg N, Lutolf MP. In Situ Patterning of Microfluidic Networks in 3D Cell-Laden Hydrogels. *Advanced Materials* 2016;28:7450-6.

- [15] Gandara-Montano GA, Stoy V, Dudič M, Petrák V, Haškovcová K, Knox WH. Large optical phase shifts in hydrogels written with femtosecond laser pulses: elucidating the role of localized water concentration changes. *Optical Materials Express* 2017;7:3162-80.
- [16] Chan JW, Huser T, Risbud S, Krol DM. Structural changes in fused silica after exposure to focused femtosecond laser pulses. *Optics letters* 2001;26:1726-8.
- [17] Kaehr B, Scrymgeour DA. Direct-write graded index materials realized in protein hydrogels. *Applied Physics Letters* 2016;109:123701.
- [18] Ding L, Blackwell RI, Künzler JF, Knox WH. Femtosecond laser micromachining of waveguides in silicone-based hydrogel polymers. *Applied optics* 2008;47:3100-8.
- [19] Ramirez LPR, Heinrich M, Richter S, Dreisow F, Keil R, Korovin AV, Peschel U, Nolte S, Tünnermann A. Tuning the structural properties of femtosecond-laser-induced nanogratings. *Applied Physics A* 2010;100:1-6.
- [20] Bille JF, Engelhardt J, Volpp H-R, Laghouissa A, Motzkus M, Jiang Z, Sahler R. Chemical basis for alteration of an intraocular lens using a femtosecond laser. *Biomedical optics express* 2017;8:1390-404.
- [21] Wochnowski C, Eldin MAS, Metev S. UV-laser-assisted degradation of poly (methyl methacrylate). *Polymer degradation and stability* 2005;89:252-64.
- [22] Träger J, Heinzer J, Kim HC, Hampp N. Polymers for in vivo tuning of refractive properties in intraocular lenses. *Macromolecular bioscience* 2008;8:177-83.

- [23] Takeshima N, Narita Y, Tanaka S, Kuroiwa Y, Hirao K. Fabrication of high-efficiency diffraction gratings in glass. *Optics letters* 2005;30:352-4.
- [24] Chen YX, Yang S, Yan J, Hsieh M-H, Weng L, Ouderkirk JL, Krendel M, Soman P. A Novel Suspended Hydrogel Membrane Platform for Cell Culture. *Journal of Nanotechnology in Engineering and Medicine* 2015;6:021002.
- [25] Chen YX, Cain B, Soman P. Gelatin methacrylate-alginate hydrogel with tunable viscoelastic properties. *Aims Materials Science* 2017;4:363-9.
- [26] Qin XH, Wang X, Rottmar M, Nelson BJ, Maniura-Weber K. Near-Infrared Light-Sensitive Polyvinyl Alcohol Hydrogel Photoresist for Spatiotemporal Control of Cell-Instructive 3D Microenvironments. *Advanced Materials* 2018.
- [27] Kuijpers AJ, Engbers GHM, Feijen J, De Smedt SC, Meyvis TKL, Demeester J, Krijgsveld J, Zaat SAJ, Dankert J. Characterization of the network structure of carbodiimide cross-linked gelatin gels. *Macromolecules* 1999;32:3325-33.
- [28] Morikawa J, Orie A, Hashimoto T, Juodkazis S. Thermal diffusivity in femtosecond-laser-structured micro-volumes of polymers. *Applied Physics A* 2010;98:551-6.
- [29] Zheng C, Chen T, Hu A, Liu S, Li J. Fabrication of 3D embedded hollow structures inside polymer dielectric PMMA with femtosecond laser. *International Society for Optics and Photonics*. p. 1001804.

- [30] Ding L, Blackwell R, Künzler JF, Knox WH. Large refractive index change in silicone-based and non-silicone-based hydrogel polymers induced by femtosecond laser micromachining. *Optics express* 2006;14:11901-9.
- [31] Ding L, Cancado LG, Novotny L, Knox WH, Anderson N, Jani D, Linhardt J, Blackwell RI, Künzler JF. Micro-Raman spectroscopy of refractive index microstructures in silicone-based hydrogel polymers created by high-repetition-rate femtosecond laser micromachining. *JOSA B* 2009;26:595-602.
- [32] Hernandez DS, Ritschdorff ET, Connell JL, Shear JB. In Situ Imprinting of Topographic Landscapes at the Cell–Substrate Interface. *Journal of the American Chemical Society* 2018;140:14064-8.
- [33] Schaffer CB, Brodeur A, Mazur E. Laser-induced breakdown and damage in bulk transparent materials induced by tightly focused femtosecond laser pulses. *Measurement Science and Technology* 2001;12:1784.
- [34] Hirao K, Miura K. Writing waveguides and gratings in silica and related materials by a femtosecond laser. *Journal of non-crystalline solids* 1998;239:91-5.
- [35] Chan JW, Huser T, Risbud S, Krol D. Structural changes in fused silica after exposure to focused femtosecond laser pulses. *Optics letters* 2001;26:1726-8.
- [36] Nikkhah M, Edalat F, Manoucheri S, Khademhosseini A. Engineering microscale topographies to control the cell–substrate interface. *Biomaterials* 2012;33:5230-46.

- [37] Jeon H, Simon CG, Kim G. A mini-review: cell response to microscale, nanoscale, and hierarchical patterning of surface structure. *Journal of Biomedical Materials Research Part B: Applied Biomaterials* 2014;102:1580-94.
- [38] Li Y, Huang G, Zhang X, Wang L, Du Y, Lu TJ, Xu F. Engineering cell alignment in vitro. *Biotechnology advances* 2014;32:347-65.
- [39] Hoffman BD, Grashoff C, Schwartz MA. Dynamic molecular processes mediate cellular mechanotransduction. *Nature* 2011;475:316.
- [40] Aubin H, Nichol JW, Hutson CB, Bae H, Sieminski AL, Cropek DM, Akhyari P, Khademhosseini A. Directed 3D cell alignment and elongation in microengineered hydrogels. *Biomaterials* 2010;31:6941-51.
- [41] Vader D, Kabla A, Weitz D, Mahadevan L. Strain-induced alignment in collagen gels. *PloS one* 2009;4:e5902.
- [42] Jang JM, Tran S-H-T, Na SC, Jeon NL. Engineering controllable architecture in matrigel for 3D cell alignment. *ACS applied materials & interfaces* 2015;7:2183-8.
- [43] Subramony SD, Dargis BR, Castillo M, Azeloglu EU, Tracey MS, Su A, Lu HH. The guidance of stem cell differentiation by substrate alignment and mechanical stimulation. *Biomaterials* 2013;34:1942-53.
- [44] Stoppel WL, Kaplan DL, Black Iii LD. Electrical and mechanical stimulation of cardiac cells and tissue constructs. *Advanced drug delivery reviews* 2016;96:135-55.

- [45] Rangarajan S, Madden L, Bursac N. Use of flow, electrical, and mechanical stimulation to promote engineering of striated muscles. *Annals of biomedical engineering* 2014;42:1391-405.
- [46] Norman JJ, Desai TA. Control of cellular organization in three dimensions using a microfabricated polydimethylsiloxane–collagen composite tissue scaffold. *Tissue engineering* 2005;11:378-86.
- [47] Cox TR, Erler JT. Remodeling and homeostasis of the extracellular matrix: implications for fibrotic diseases and cancer. *Disease models & mechanisms* 2011;4:165-78.
- [48] Kumar S, Weaver VM. Mechanics, malignancy, and metastasis: the force journey of a tumor cell. *Cancer and Metastasis Reviews* 2009;28:113-27.
- [49] Friedl P, Alexander S. Cancer invasion and the microenvironment: plasticity and reciprocity. *Cell* 2011;147:992-1009.

CHAPTER 4 : Embedded diffractive volume grating by femtosecond laser induced densification

4.1 Abstract

We report a new phenomenon coined as femtosecond laser induced densification. A new method, based on this phenomenon, was used to achieve three-dimensional refractive-index-modified microstructures within optically transparent hydrogels. A new phase diagram with ablation and densification hydrogel-modification regimes was generated by measuring the width of modified line-features as a function of laser dosage (scan speed, power). The changes in refractive index (RI) were obtained by measuring the diffraction efficiency ratio of grating's first and second orders. This method was extended to the fabrication of user-defined gratings such as grid, square and ring gratings, highlighting the potential flexibility of this method for making complex phase elements in hydrogels, and their potential integration to develop new biointegrated optical devices.

4.2 Introduction

Inspired by natural systems, microstructural modification has been exploited as a promising strategy to introduce new optical properties to conventional materials such as manipulation of light based on diffraction [1–4]. These structural photonic materials have become increasingly important in biomedical applications ranging from imaging to diagnostics to sensing [5–8]. This has motivated research towards developing photonic components that could seamlessly interface with the biological world [9–12]. Hydrogels, which biomimetically recapitulate physical, chemical, and mechanical properties of natural extracellular matrix (ECM), have been widely developed as a candidate material for implantable artificial muscles, cell scaffold and tissue organs [13–19]. As a result, several natural or synthetic hydrogels such as silk, collagen, chitosan, poly (ethylene glycol) diacrylate (PEGDA), polyacrylamide, polyacrylic acid, etc., have been used to develop new optical devices [8,20–24]. A range of 2D and 3D photonic components based on these hydrogels, such as light waveguides for relaying physiological signals, color switching sensor, concentrating devices for improved imaging, have been demonstrated [8,22,25–27].

Till date, fabrication methods such as soft lithography, nanoimprinting [28], E-beam lithography, interference lithography, digital projection lithography [18,29,30] and femtosecond laser processing [21] have been used to develop optical elements using hydrogels. However, current methods typically modify the hydrogel surfaces with micro/nanostructures to enable structural photonic applications. Since such surface structure are prone to damage,

there is a growing demand to have such structures inside the materials. Femtosecond laser processing, with its ability to locally induce material changes within transparent material, has been used to develop photonic microstructures embedded within glass, silica, sapphire, and polymers. However, this method has not been used to develop structural photonics embedded with biocompatible hydrogels.

In this work, we discover a new phenomenon called femtosecond laser induced densification within a model PEGDA hydrogel and utilize this phenomenon to introduce a refractive index change within the hydrogel to generate diffractive optical elements such as volume gratings including grid, square and ring gratings [19,31].

4.3 Methods

PEGDA prepolymer preparation: Poly (ethylene glycol) diacrylate (PEGDA, $M_n=700$) and phosphate buffered saline (PBS) were purchased from Sigma-Aldrich and used without further modifications. The photoinitiator, LAP, was synthesized using previously established protocol [19]. The prepolymer solution was composed of varying amounts of PEGDA (10% to 90%, v/v) with LAP (0.25%, w/v for all compositions). The prepolymer solution was mixed for 10 mins using a magnetic stirrer, filtered (pore size=0.2 μm), and used within 2 days after preparation. During the fabrication process, 30 μL of the prepolymer solution was pipetted on a microscopic glass slide (48 mm \times 24 mm, Fisher Scientific) that was surface modified using Sigmacote (Sigma-Aldrich). A PDMS spacer (Sigma-Aldrich) was placed between the

microscope slide (bottom) and a glass coverslip (top) to control the prepolymer layer thickness to be 1mm.

Optical and mechanical characterization of PEGDA: Refractive indices of crosslinked samples were directly measured using digital refractometer (Sper Scientific). To characterize absorption properties, absorption spectra of the hydrogel samples kept in plastic cuvettes were measured using scanning spectrophotometer from 250 to 1100 nm (Thermo Scientific). The absorption spectra in Fig. 4.1 are normalized. As for the swelling property, the hydrogels were immersed in PBS for 12hr was characterized by the fractal weight of the samples at the dried state and at the swelled state. The weight was measured using laboratory balance (Thermo Scientific). Mechanical properties were measured using a standard Rheometer (AR2000, TA Instruments, USA). Briefly, samples were prepared by casting the prepolymer solution in PDMS mold (8 mm diameter, 100 μm thickness) and exposing samples to UV light (output power 3.5 mw cm^{-2} , Ominicure S2000) for 10 seconds. The crosslinked samples were then transferred to the well plates and incubated in PBS for 24 hours to facilitate diffusion of uncrosslinked prepolymer. Next, samples were tested at 25 $^{\circ}\text{C}$ using 8 mm diameter bottom plate with a gap of 0.5 mm. Storage modulus (G') and loss modulus (G'') were measured at 0.5% strain for a range of 0.1-100 Hz. Elastic modulus was calculated by the following Equation (1) where the Poisson ratio τ was assumed as 0.33. The linear regions of both moduli recorded between 1 and 10 Hz were used to calculate the Elastic modulus (E) [19].

$$E = 2G(1 + \tau) \text{ Where } G = \sqrt{G'^2 + G''^2} \quad (1)$$

Femtosecond laser writing setup: Custom-built fs-laser platform was designed and built by combining a Ti:Sapphire fs laser (Coherent, Chameleon, USA) with a Zeiss Microscope (Observer Z1, Germany) (See Figure SI-3.1 in section 3).

Characterization of fabricated samples: Fabricated samples were characterized using phase-contrast microscope and confocal microscope. The samples for phase-contrast microscope (Leica DM6000, Germany) were kept hydrated. For obtaining confocal fluorescence images, fabricated PEGDA samples were submerged into Rhodamine B solution (10% w/v) for 2 mins, washed 3 times with PBS before confocal imaging (Zeiss observer X1). Then the samples are imaged using 10× objective through 3D scanning and reconstructed in microscope software.

Characterization of optical properties of fabricated devices: The details of the setup used to characterize the optical properties of printed devices is illustrated in **Figures S5.1**. The setup in Figure S5.1 is used to characterize the diffraction pattern and to measure diffraction efficiency.

4.4 Results and Discussion

To develop durable photonic devices, the hydrogel composition was optimized using the dual criteria of high optical transparency and mechanical stability. We investigated the optical loss for PEGDA hydrogels (MW=700, Sigma Aldrich) by choosing a range of concentration (10%, 30%, 50%, 70% and 90% v/v) in Fig. 4.1(A). PEGDA hydrogels with 10% concentration in

standard cuvette were opaque and white in color, indicating scattering across the visible spectrum. With increasing concentration, the PEGDA hydrogels became more transparent. Absorption spectrum in the visible range confirmed the strong dependency on concentration of the polymer as shown in Fig. 4.1(B). PEGDA hydrogels of 10% concentration had an absorption of 0.4, while the absorption gradually dropped down to 0.2 with increasing concentration over 50%. Similar trend was observed with the refractive index (RI) in Fig. 4.1 (C). The RI increased linearly with the prepolymer concentration reaching to 1.48 for 90% PEGDA hydrogels. Besides the optical properties, we also measured the mechanical properties of the hydrogels using rheometer in Fig. 4.1 (D). The elastic modulus of PEGDA hydrogels increased with higher concentration; for 90% PEGDA modulus was 176 kPa. We performed swelling test to investigate the stability of the optical properties in the aqueous environment. The swelling ratio in Fig. 4.1 (D) increased as PEGDA concentration increased from 1.05 to 1.51. The size of the hydrogel discs also increased with increasing PEGDA concentration in the inset of Fig. 4.1 (D), whereas their circular shapes were maintained with almost no deformation. Despite swelling, no change in transparency was observed. Considering their transparency and mechanical stability, we chose 90% PEGDA for the following studies.

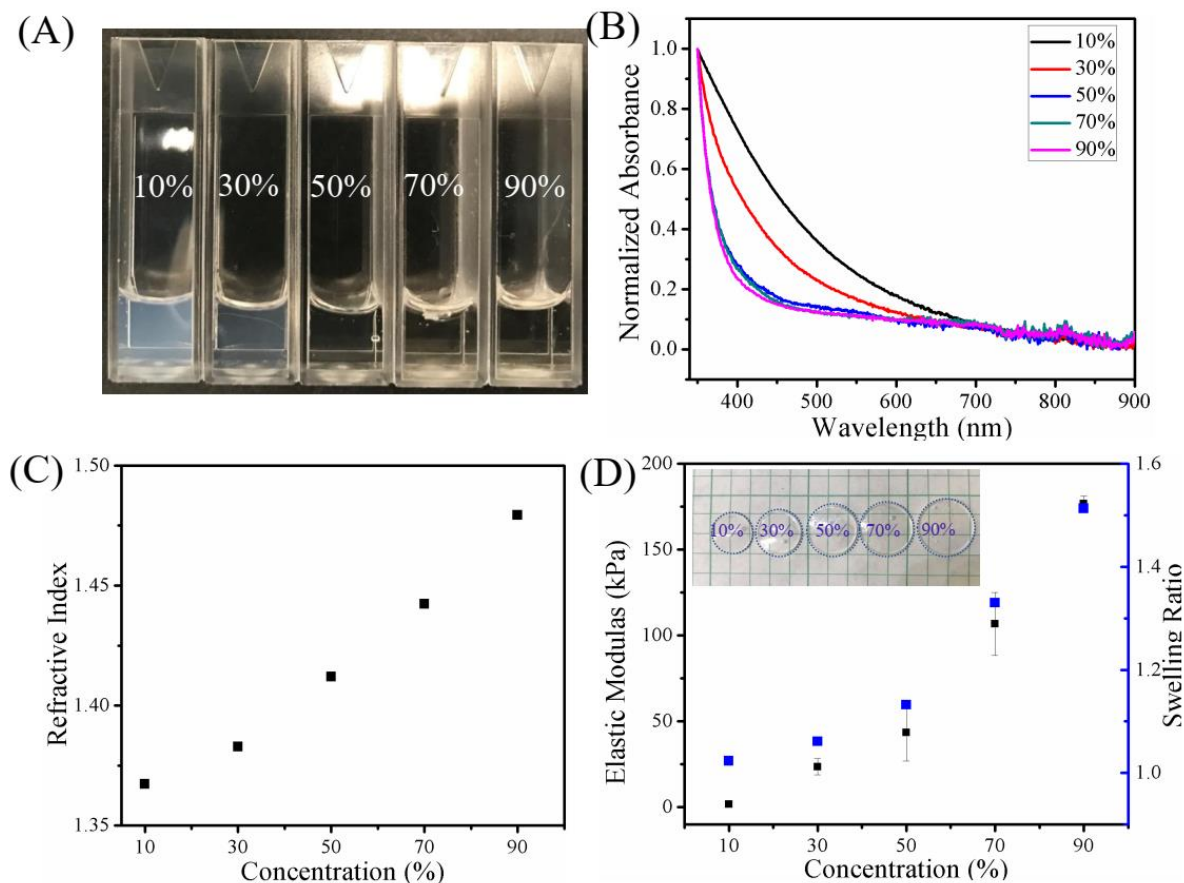


Figure 4.1 Characterization of PEGDA hydrogels with different concentration. (A) Optical transparency and (B) absorption spectrum in visible spectrum. (C) RI. The RI increased from 1.35 to 1.48 with the concentration increasing of hydrogel. (D) Mechanical stability. With increasing concentration, the elastic modulus and the swelling ratio increases, with no changes in the optical transparency.

To fabricate embedded microstructures within hydrogel discs, the processing is done in two steps. In the first step, the prepolymer solution of 90% PEGDA with 0.25% photoinitiator lithium phenyl-2,4,6-trimethylbenzoylphosphinate (LAP), was pipetted between two glass slides with a 1mm thick PDMS

spacer and then partially crosslinked under UV exposure (Ominicure S2000) at 3.5 mW cm^{-2} for 10 seconds. In the second step, a femtosecond laser of wavelength 730 nm and pulse duration 140 fs, repetition rate at 80 MHz (Coherent, USA), were tightly focused by a high numerical aperture (NA=0.55, Zeiss, Germany) objective lens to process the PEGDA hydrogel discs in Fig. 4.2 (A). For fabricating the user-defined pattern, the laser focal spot was moved by the XY stage and the Z stage on objective lens under control of a customized Visual Basic Code as shown in Fig. 4.2 (A). Laser dosage was changed by modulated the average power of the laser using an attenuator (Thorlabs) or by modulating the scanning speed of the XY stage.

During the processing experiments, three material modification regimes namely partial-crosslinking, densification and ablation were identified as a function of laser exposure dosage as shown in Fig. 4.2 (B). In the partial-crosslinking regime in Fig. 4.2 (B)-(i), free acrylate groups are likely left behind as the conversion of the acrylate double bond into covalent bonds is not complete after UV crosslinking step as shown in Fig. 4.2 (B)-(i). With increased fs-laser dosage however, we observe densification within the hydrogel as seen in Fig. 4.2(B)-(ii). Due to the absorption of LAP at 365 nm, the tightly focused femtosecond laser at 730 nm at lower dosage drives two-photon crosslinking of partially crosslinked PEGDA by converting the remaining free acrylate groups into covalent double bonds. The densification processing likely results in collapse and compaction of PEGDA chains and appears brighter as compared with the rest of the PEGDA as shown in the phase contrast image in Fig. 4.2 (C)-(ii). Further increasing the laser dosage caused ablated cracks or voids in the hydrogel discs as shown in Fig. 4.2 (B)-(iii) and Fig. 4.2 (C)-(iii). To identify processing conditions to reliably obtain

densification and the resulting RI change within PEGDA hydrogels we systematically varied the laser dosage in terms of scanning stage speed and laser power and measured the width of the modified line patterns. In Fig. 4.2 (D), an increase in laser power, while the scanning speed is constant, leads to continuous material modification shifting from densification to ablation. The width of the densified lines and the ablated micro-cracks increased. In Fig. 4.2 (E), increasing scanning speed while the laser power is constant, results in a decrease of laser dosage, therefore decreasing the line width. To ensure reliable fabrication of densified lines, we chose fabrication parameter at 200 mW, 1000 $\mu\text{m/s}$ for following studies.

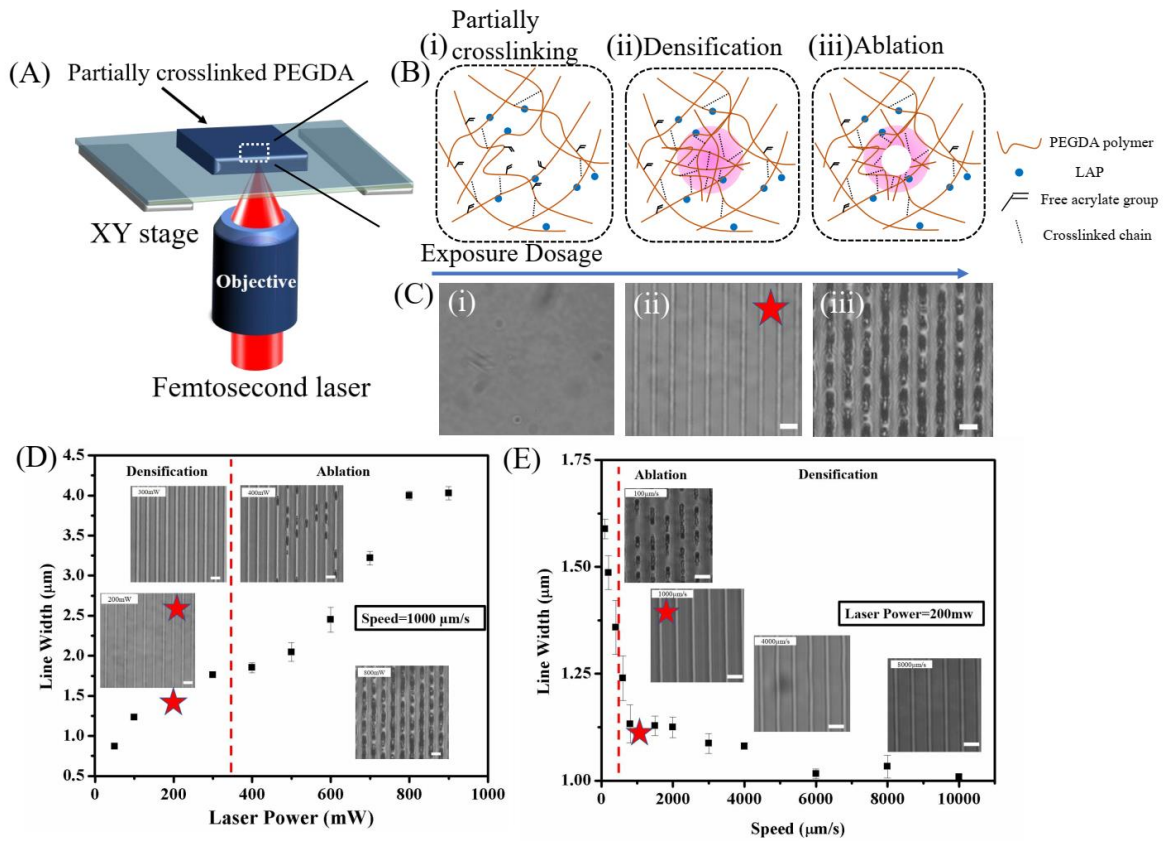


Figure 4.2 (A) Schematic of femtosecond laser processing and (B) associated material modification within (i) partially crosslinked PEGDA hydrogel. With increasing laser dosage, the partially crosslinked hydrogel goes from (ii) densification to (iii) ablation. (C) The phase contrast images (top-view) of the fs-laser written features inside the PEGDA hydrogel. Material modification phase diagram: Line width is plotted as a function of laser dosage by varying either (D) fabrication speed or (E) laser power.

Optimized laser power and scanning speeds were used to obtain microstructures within PEGDA. An image of the fabricated phase grating in PEGDA hydrogel disc is shown in Fig. 4.3 (C). The period d of the grating is $10\ \mu\text{m}$, and the region that appears brighter than surrounding materials was induced by femtosecond laser densification. The image is captured using a phase-contrast microscope which indicates that the RI is higher than the surrounding materials. The width a of the laser modified line is approximately $1\ \mu\text{m}$. The duty ratio $\rho=a/d$ is 1:10 here. To obtain the cross-sectional image of the densified microstructures, the side of the hydrogel disc was directly cut using a sharp razor blade for observation. Figure 4.3 (D) shows the cross-sectional side-view of the volume grating which shows the depth h of the volume grating to be $14.52\ \mu\text{m}$.

The RI change between densified and unmodified PEGDA can be represented by $n+\Delta n$, where n is the RI of unmodified PEGDA.. We investigated the RI difference by shining He-Ne laser beam with $632.8\ \text{nm}$ and $11\ \text{mW}$ on the volume grating and measured the energy distribution of the diffraction orders in Fig. 4.3 (B). The diffraction pattern is shown in Fig. 4.3 (E), which is captured using CMOS

camera on the other side of the sample. We quantified the RI change Δn by measuring the diffraction efficiency at 0th, 1st and 2nd diffraction orders. The efficiency as the function of the RI change, is derived from Fourier Optics as explained below [32].

For a phase grating, its transmission function can be written as:

$$t(x, y) = (e^{i(\phi+\Delta\phi)} - e^{i\Delta\phi}) \text{rect}\left(\frac{x}{a}\right) \otimes \frac{1}{d} \text{comb}\left(\frac{x}{d}\right) + e^{i\phi} \quad (1)$$

Where the original phase $\phi = \frac{2\pi(n+\Delta n)h}{\lambda}$, the RI induced phase difference $\Delta\phi = \frac{2\pi\Delta nh}{\lambda}$, h is the grating depth, d is the period of the grating and a is the linewidth.

Here we assume the laser induced RI change is uniform in the modified region. The diffraction spectrum $F[t(x, y)]$ of Equation (1) can be calculated through Fourier transformation and the actual diffraction energy distribution $I(x, y)$ is the product of the diffraction spectrum conjugates.

$$I(x, y) = \langle F[t(x, y)] F^*[t(x, y)] \rangle \quad (2)$$

Based on Equation (2), the efficiency of m^{th} diffraction order, η_m , can be calculated by

$$\begin{cases} \eta_0 = 1 - 2\rho(1 - \rho)(1 - \cos \Delta\phi) \\ \eta_{m \geq 1} = \frac{1}{m^2 \pi^2} (1 - \cos 2m\pi\rho)(1 - \cos \Delta\phi) \end{cases} \quad (3)$$

Where ρ is the duty ratio of the volume grating, that is 1:10 here.

According to Equation (3), Figure 4.3 (F) shows the theoretical relationship between RI and intensity ratio. By comparing the measured light intensities of diffraction orders 1st and 0th, we can determine the RI change within the densified grating region. Figure 4.3 (F) shows the ratio between intensity of the

1st and 0th order is 0.01087, and the corresponding RI change calculated through equations is about 0.0051. This value demonstrates that laser induced densification phenomenon not only change the mechanical properties but can also change the optical property (RI). Therefore, this is very promising technology to make embedded diffraction components within hydrogels for biophotonics applications.

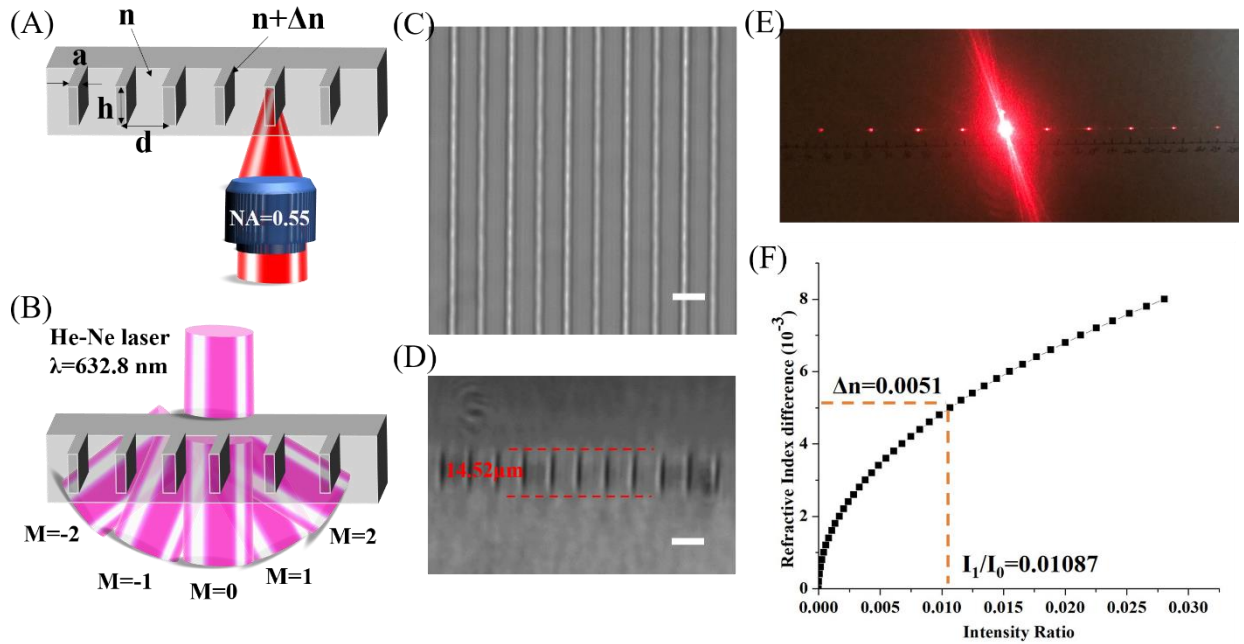


Figure 4.3 (A) Schematic of fs laser 3D writing inside hydrogel. n is the RI of hydrogels. Δn is the RI change due to laser induced densification. (B) Sketch of grating diffracting using He-Ne laser beam of 632.8 nm. Phase contrast images of diffraction grating at (C) top view and (D) side view. (E) Optical photograph of grating's diffraction pattern. (F) Intensity ratio between 0th diffraction order and 1st diffraction order and theoretical calculation of corresponding RI change. Scale bar 10 μm

Next, we fabricated several volume beam shapers including grid, square and ring gratings inside PEGDA hydrogel using laser induced densification. The microscopic images of the grid, square and ring gratings are shown in Fig. 4.4, which are taken with a phase contrast microscope. To further demonstrate their densified patterns, we image these structures by staining the samples with Rhodamine B and then reconstructed their fluorescence images under laser scanning confocal microscope, shown in the second row of Fig. 4.4. The fluorescence intensity of densified patterns is obviously stronger than surrounding materials, which indicates that there are more dense polymer networks. Their optical properties in terms of diffraction patterns, shown in the third row of Fig. 4.4, are probed by a collimated He-Ne laser, which is normally incident to the sample surfaces. For the grid and square 2D gratings, obvious and symmetrical diffraction points are observed while for the ring grating, the far-field diffraction pattern shows an intense central beam (0^{th} order) and, two close high-order cone beams. Some of the diffraction points are distorted due to the misalignment of the He-Ne laser. These special shapes gratings can be used for beam shaping applications.

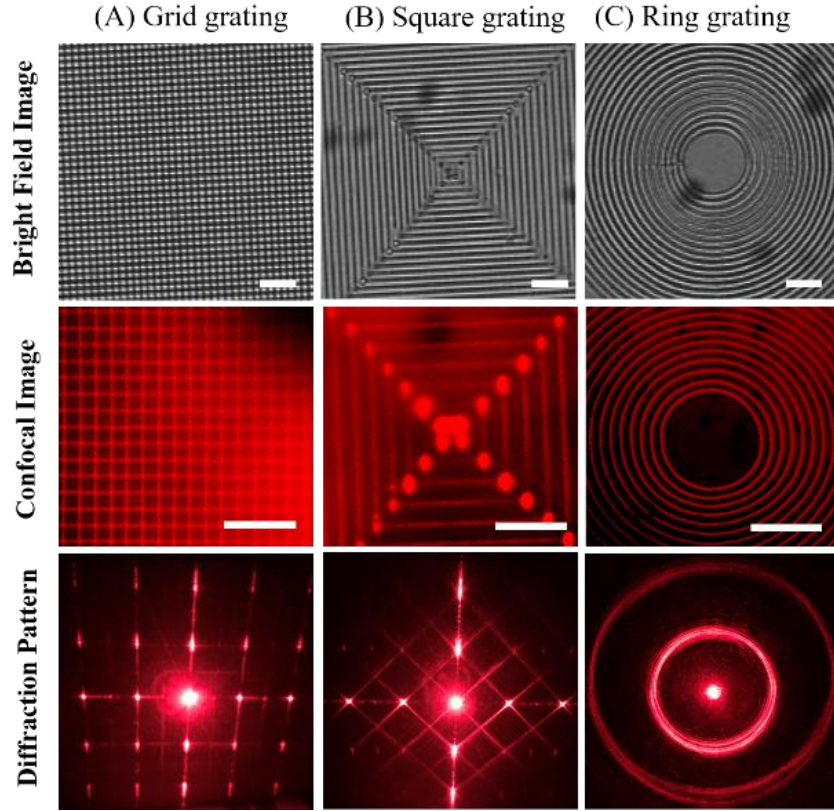


Figure 4.4 Different diffraction gratings including (A) 2D linear grating (B) square grating and (C) circular grating are fabricated inside PEGDA hydrogel by laser induced densification. The bright field illustrates clear microfeatures within partially crosslinked hydrogel. The confocal images of diffraction elements using Rhodamine B staining presents the density difference of the embedded microstructures. The optical photograph of the patterns captured at far field shows the diffraction property of these microstructures. Scale bar: 50 μm

4.5 Conclusion

In summary, we observed effective RI change within a PEGDA hydrogel using femtosecond laser induced densification phenomenon. The origin of the optical effects may arise from the

laser induced phase separation of the water and the polymer, leading to a denser material at the laser modified regions. The RI change in the PEGDA hydrogel was calculated to be 0.0051. Laser induced densification technique can fabricate beam shapers and this could be a potential method for biointegrated photonics.

4.6 References

- [1] Poleshchuk A G, Churin E G, Koronkevich V P, Korolkov V P, Kharissov A A, Cherkashin V V., Kiryanov V P, Kiryanov A V., Kokarev S A and Verhoglyad A G 1999 Polar coordinate laser pattern generator for fabrication of diffractive optical elements with arbitrary structure *Appl. Opt.* **38** 1295
- [2] Swanson G J 1989 *Binary Optics Technology : The Theory and Design of Multi-level Diffractive Optical Elements* (MASSACHUSETTS INST OF TECH LEXINGTON LINCOLN LAB)
- [3] Gale M T 1997 Replication techniques for diffractive optical elements *Microelectron. Eng.* **34** 321–39
- [4] Gale M T, Rossi M, Schütz H, Ehbets P, Herzig H P and Prongué D 1993 Continuous-relief diffractive optical elements for two-dimensional array generation *Appl. Opt.* **32** 2526
- [5] Shan D, Gerhard E, Zhang C, Tierney J W, Xie D, Liu Z and Yang J 2018 Polymeric biomaterials for biophotonic applications *Bioact. Mater.* **3** 434–45
- [6] Vörös J, Ramsden J J, Csúcs G, Szendro I, De Paul S M, Textor M and Spencer N D

- 2002 Optical grating coupler biosensors *Biomaterials* **23** 3699–710
- [7] Chao W, Kim J, Rekawa S, Fischer P and Anderson E H 2009 Demonstration of 12 nm Resolution Fresnel Zone Plate Lens based Soft X-ray Microscopy *Opt. Express* **17** 17669
- [8] Xiong R, Luan J, Kang S, Ye C, Singamaneni S and Tsukruk V V. 2020 Biopolymeric photonic structures: Design, fabrication, and emerging applications *Chem. Soc. Rev.* **49** 983–1031
- [9] Sanchez-Dealcazar D, Romera D, Castro-Smirnov J, Sousaraei A, Casado S, Espasa A, Morant-Miñana M C, Hernandez J J, Rodríguez I, Costa R D, Cabanillas-Gonzalez J, Martinez R V. and Cortajarena A L 2019 Engineered protein-based functional nanopatterned materials for bio-optical devices *Nanoscale Adv.* **1** 3980–91
- [10] Huang T, Xu H, Jiao K, Zhu L, Brown H R and Wang H 2007 A novel hydrogel with high mechanical strength: A macromolecular microsphere composite hydrogel *Adv. Mater.* **19** 1622–6
- [11] Lawrence B D, Cronin-Golomb M, Georgakoudi I, Kaplan D L and Omenetto F G 2008 Bioactive silk protein biomaterial systems for optical devices *Biomacromolecules* **9** 1214–20
- [12] Kotwal A and Schmidt C E 2001 Electrical stimulation alters protein adsorption and nerve cell interactions with electrically conducting biomaterials *Biomaterials* **22** 1055–64

- [13] Zhang Y S and Khademhosseini A 2017 Advances in engineering hydrogels *Science* (80-.). **356**
- [14] Elisseeff J 2008 Hydrogels: Structure starts to gel *Nat. Mater.* **7** 271–3
- [15] Kopeček J 2007 Hydrogel biomaterials: a smart future? *Biomaterials* **28** 5185–92
- [16] Kamata H, Akagi Y, Kayasuga-Kariya Y, Chung U Il and Sakai T 2014 “Nonswellable” hydrogel without mechanical hysteresis *Science* (80-.). **343** 873–5
- [17] El-Sherbiny I M and Yacoub M H 2013 Hydrogel scaffolds for tissue engineering: Progress and challenges *Glob. Cardiol. Sci. Pract.* **2013** 38
- [18] Xiong Z, Kunwar P and Soman P 2021 Hydrogel-Based Diffractive Optical Elements (hDOEs) Using Rapid Digital Photopatterning *Adv. Opt. Mater.* **9** 2001217
- [19] Xiong Z, Li H, Kunwar P, Zhu Y, Ramos R, McLoughlin S, Winston T, Ma Z and Soman P 2019 Femtosecond laser induced densification within cell-laden hydrogels results in cellular alignment *Biofabrication* **11** 35005
- [20] Yin M J, Yao M, Gao S, Zhang A P, Tam H Y and Wai P K A 2016 Rapid 3D Patterning of Poly(acrylic acid) Ionic Hydrogel for Miniature pH Sensors *Adv. Mater.* **28** 1394–9
- [21] Sun Y L, Dong W F, Niu L G, Jiang T, Liu D X, Zhang L, Wang Y S, Chen Q D, Kim D P and Sun H B 2014 Protein-based soft micro-optics fabricated by femtosecond laser direct writing *Light Sci. Appl.* **3** e129–e129
- [22] Choi M, Choi J W, Kim S, Nizamoglu S, Hahn S K and Yun S H 2013 Light-guiding hydrogels for cell-based sensing and optogenetic synthesis in vivo *Nat. Photonics* **7** 987–

- [23] Wu Z L, Moshe M, Greener J, Therien-Aubin H, Nie Z, Sharon E and Kumacheva E 2013 Three-dimensional shape transformations of hydrogel sheets induced by small-scale modulation of internal stresses *Nat. Commun.* **4** 1–7
- [24] Tadepalli S, Slocik J M, Gupta M K, Naik R R and Singamaneni S 2017 Bio-Optics and Bio-Inspired Optical Materials *Chem. Rev.* **117** 12705–63
- [25] Qin X H, Wang X, Rottmar M, Nelson B J and Maniura-Weber K 2018 Near-Infrared Light-Sensitive Polyvinyl Alcohol Hydrogel Photoresist for Spatiotemporal Control of Cell-Instructive 3D Microenvironments *Adv. Mater.* **30** 1705564
- [26] Choi M, Humar M, Kim S and Yun S H 2015 Step-Index Optical Fiber Made of Biocompatible Hydrogels *Adv. Mater.* **27** 4081–6
- [27] Xiong Z, Kunwar P and Soman P 2020 Hydrogel-Based Diffractive Optical Elements (hDOEs) Using Rapid Digital Photopatterning *Adv. Opt. Mater.* 2001217
- [28] Pal R K, Kurland N E, Wang C, Kundu S C and Yadavalli V K 2015 Biopatterning of silk proteins for soft micro-optics *ACS Appl. Mater. Interfaces* **7** 8809–16
- [29] Xiong Z, Liu H, Tan X, Lu Z, Li C, Song L and Wang Z 2014 Diffraction analysis of digital micromirror device in maskless photolithography system *J. Micro/Nanolithography, MEMS, MOEMS* **13** 043016
- [30] Zhang Y, Luo J, Xiong Z, Liu H, Wang L, Gu Y, Lu Z, Li J and Huang J 2019 User-defined microstructures array fabricated by DMD based multistep lithography with dose

modulation *Opt. Express* **27** 31956

- [31] Xiong Z and Soman P 2020 User-defined and localized cellular alignment using femtosecond laser hydrogel densification *Frontiers in Ultrafast Optics: Biomedical, Scientific, and Industrial Applications XX* vol 11270 (International Society for Optics and Photonics) p 1127009
- [32] Li Q-K, Lu Y-M, Hua J-G, Yu Y-H, Wang L, Chen Q-D, Juodkazis S and Sun H-B 2017 Multilevel phase-type diffractive lens embedded in sapphire *Opt. Lett.* **42** 3832–5

CHAPTER 5: Hydrogel-based diffractive optical elements (hDOEs) using rapid digital photopatterning*

5.1 Abstract

Hydrogels, due to their optical transparency and biocompatibility, have emerged as an excellent alternative to conventional optical materials for biomedical applications. Advances in microfabrication techniques have helped convert conventional hydrogels into optically functional materials such as hydrogel-based diffraction optical elements (hDOEs). However, key challenges related to device customization and ease/speed of fabrication need to be addressed to enable widespread utility and acceptance of hDOEs in the field. Here, we report rapid printing of customized hDOEs on polyethylene glycol diacrylate (PEGDA) hydrogel using digital photopatterning; a novel method that combines simulated computer-generated hologram (SCGH) and projection photolithography. To showcase the versatility of this approach, a range of hDOEs are demonstrated, including 1D/2D diffraction gratings, Dammann grating, Fresnel zone plate (FZP) lens, fork-shaped grating and computer-generated hologram (CGH) of arbitrary pattern. Results demonstrate that printed hDOEs exhibit optical performance that is comparable with devices made with conventional materials. This versatile

*Adapted from: Z. Xiong, P. Kunwar, P. Soman, Hydrogel-based diffractive optical elements (hDOEs) using rapid photopatterning, *Advanced Optical Materials*, 9 (2), 2001217 (2021)

*Reprinted as permitted by John Wiley & Sons, Inc author agreement for personal use.

strategy can be potentially implemented with other photosensitive hydrogels to achieve user-defined hDOEs in a time-efficient and cost-effective fashion.

5.2 Introduction

Hydrogels, which recapitulate biophysical and biochemical properties of extracellular matrix, have made significant impact in many biomedical fields, such as, drug delivery, regenerative medicine, tissue engineering, bio-sensing, flexible electronics and microfluidics [1–6]. Continued advances in polymer chemistry have demonstrated that functional properties can be introduced within hydrogels to transform them into ‘smart’ materials. This has led to the development of hydrogels with customizable properties such as the abilities to change shapes, resist mechanical forces, release target enzymes and exhibit electrical, magnetic as well as optical properties [7–14].

Inspired by natural systems, microstructural modification has been exploited as a promising strategy to introduce new optical properties to conventional materials such as manipulation of light based on diffraction or diffraction optical elements (DOEs) [15–18]. These DOEs have become increasingly important in biomedical applications ranging from imaging to diagnostics to sensing [19–22]. In the past decades, the DOEs are mostly made of conventional optical materials such as glass, semiconductor, and metals. Nonetheless, the inherent lack of mechanical flexibility and biocompatibility of these materials render their use difficult for *in vitro* and *in vivo* biophotonics applications. Hydrogels, due to their unique optical transparency and biocompatibility, provides a good alternative to conventional optical materials. Several natural and synthetic hydrogels, such as, silk, chitin, chitosan, bovine serum albumin, polyacrylamide, polyacrylic acid and PEGDA have been used to make hydrogel based DOEs

or hDOEs with optical performance comparable to conventional materials [22–28]. However, competing challenges such as high resolution, ease/cost of manufacturing, and customization of design based on target applications, prevent its widespread use in the field.

At present, hDOEs such as diffraction grating, holographic components, and Fresnel zone plates (FZP) are fabricated using indirect and direct methods [7,22,26,29–31]. Indirect methods, such as mask-based photolithography, inverse opals, soft lithography, and nanoimprinting, require use of expensive physical masks, and time-consuming iterative optimization to fabricate hDOEs. On the other hand, direct methods such as electron beam lithography, direct laser writing, and multi-beam interference lithography do not require physical mask to fabricate high-resolution hDOEs, however challenges with scalability and long processing/fabrication times remain. The aforementioned challenges have to be addressed to meet the high demand for hDOEs in the field; this would require an ability to rapidly design and manufacture customized hDOEs based on the needs of target applications.

In this work, we report the design and printing of customized DOEs on synthetic PEGDA hydrogel using digital photopatterning technology which combines digital projection photolithography[32–39] with computer-generated holography[40–42]. In this work, simulated computer-generated holography (SCGH) was used to generate customized digital patterns based on DOE designs, and these digital patterns were uploaded onto a Digital Micromirror Device (DMD) to generate virtual masks (instead of conventional physical masks) to enable rapid printing of hDOEs. To highlight the broad applicability of this method, a range of

diffractive devices such as 1D/2D diffraction gratings, Dammann grating, FZP lens, fork-shaped grating and computer-generated hologram (CGH) of arbitrary pattern were designed, printed and their optical performance were compared to DOEs made using conventional materials. To our knowledge, this is the first report introducing SCGH and DMD based digital projection photolithography to print customized hDOEs. This versatile easy-to-implement fabrication strategy can be potentially extended to print hDOEs using other photosensitive hydrogels.

5.3.Results

5.3.1 Digital projection photolithography setup

The setup consists of three main components: the DLP development kit (DLP 1080p 9500 UV, Texas Instruments, USA), a UV lamp (Ominicure S2000, Canada) and an UV 10× projection lens (Thorlabs, USA) (**Figure 5.1**). Light irradiated from UV lamp was filtered to obtain a central wavelength 405 nm, and further homogenized, collimated and expanded by illumination optics before directing onto the Digital Micromirror Device (DMD). The DMD used in this system consists of 1920×1080 array of micromirrors with single pixel resolution of 10.8 μm . To fabricate customizable diffractive micro-optics, digital masks were designed and uploaded onto the DMD. The DMD generates virtual masks which dynamically modulates the irradiated UV light into customized light patterns. A projection lens was used to de-magnify the light patterns and project them onto PEGDA prepolymer between the bottom glass slide and top coverslip, which facilitate selective crosslinking of exposed areas. All micro-optics elements

reported in this study required an exposure time of 2 seconds and an UV light intensity of 70 mW cm^{-2} .

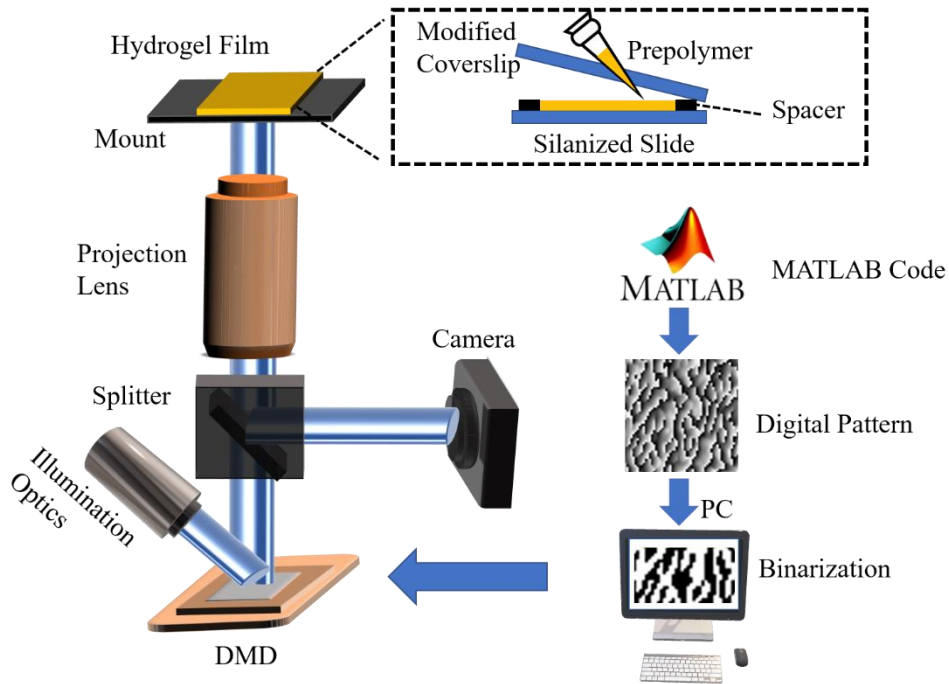


Figure 5.1. Schematic of digital projection photolithography setup that consists of illumination optics, DMD, beam splitter, projection lens, CMOS camera and sample mount. The digital mask for customized diffractive optics, generated using MATLAB algorithm (Section 2.2), was fed to the DMD to generate virtual digital mask for UV light modulation via the DMD. Inset shows the setup for hydrogel film; Prepolymer solution is sandwiched between methacrylated coverslip and silanized microscope slide with PDMS spacer for thickness control.

5.3.2 Design of DOEs using simulated computer-generated holography

Customized MATLAB algorithms based on computer generated holography were written to generate digital masks for printing customized diffractive micro-optical devices in PEGDA.

The generic process flow includes 4 steps (**Figure 5.2**): (1) User design type/specifications, (2) simulated computer-generated holography (SCGH), (3) interference pattern generation and (4) digital mask for DMD. For instance, in step 1, the user can specify design type as ‘diffraction’ (1D or 2D) and the spacing of grating as inputs. In step 2, the input parameters will be used as initial conditions for the SCGH codes in MATLAB. In this case, the SCGH of diffraction grating is the interference between two plane waves, where the angle between two beams determine the groove spacing. In step 3, the set angle is used to generate the interference pattern with defined groove spacing. Finally, in step 4, the interference pattern will be binarized to generate a digital mask for the DMD. This generic process was followed to design and print 1D and 2D diffraction gratings, Dammann grating, Fresnel zone plate, fork-shaped grating and computer-generated hologram of arbitrary pattern in model PEGDA hydrogel. This strategy allows the generation of micro-optical elements with predefined or customized optical properties. For each diffractive micro-optical element, details of masks are presented in **Section 2** while theoretical models to generate corresponding SCGH are described in section **SI-3**.

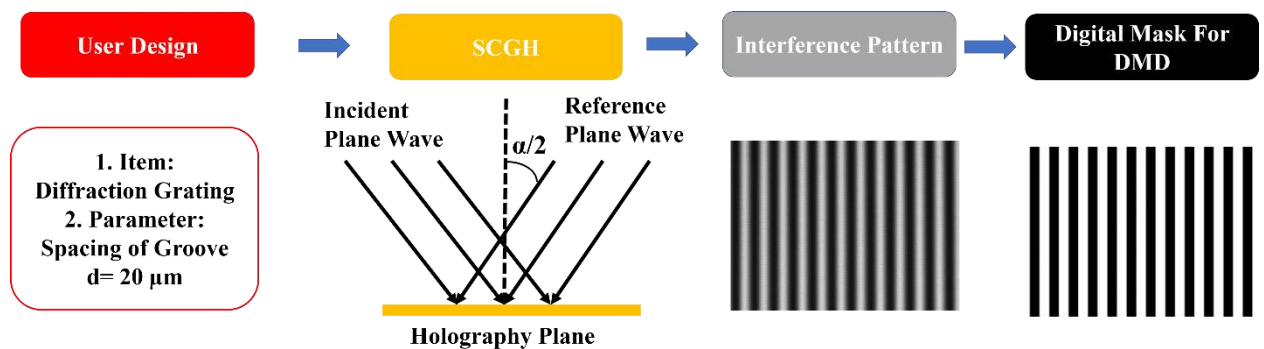


Figure 5.2. Generic process flow to generate customized digital mask based on defined inputs.

Here, 1D diffraction grating is chosen as a case study.

5.3.3 Optical and mechanical characterization of PEGDA

Any material used for making DOEs should exhibit high optical transparency, a refractive index (RI) higher than the background, as well as robust mechanical properties. To meet these requirements, we investigated different concentrations of PEGDA mixed in phosphate buffered saline (PBS) (10, 30, 50, 70 and 90%, v/v). Transmission spectroscopy showed a strong dependency of concentration of PEGDA on its optical transparency (**Figure 5.3A**). PEGDA hydrogels above 50% (v/v) had an optical transmission efficiency over 80% in the visible range (400-700 nm). At the concentration below 30%, PEGDA hydrogels pipetted in standard cuvette showed white color possibly due to strong scattering loss in the visible spectrum (Inset in Figure 5.3A). This results from the polymerization induced phase separation of polymer and solvent, as reported by other groups as well [43,44].

The refractive index (RI) of PEGDA increased linearly with the prepolymer concentration reaching a maximum of 1.48 and 1.46 for 90% crosslinking and uncrosslinked PEGDA respectively (Figure 5.3B). The increase in RI has been reported in the literature as a result of photo-polymerization [44]. As compared to conventional phase-type diffractive optics made in silica/glass where the background RI is typically air, uncrosslinked PEGDA (RI=1.46) is close to RI range of mammalian tissue (~1.35-1.45) [45]; this may be beneficial for *in vivo* biophotonic applications. Results show that a Δ RI of 0.0145 will require a thickness of 20 μ m

to achieve the necessary π phase shift [46] and diffraction/optical performance; use of simple PDMS spacer made this possible.

The elastic modulus increased with higher concentrations of prepolymer solution. (Figure 5.3C) Low PEGDA concentration samples require constant hydration and often crack during handling. Since 90% PEGDA possessed maximum transparency and ΔRI , and was found to be mechanically robust and easy to handle, this composition was chosen for this study.

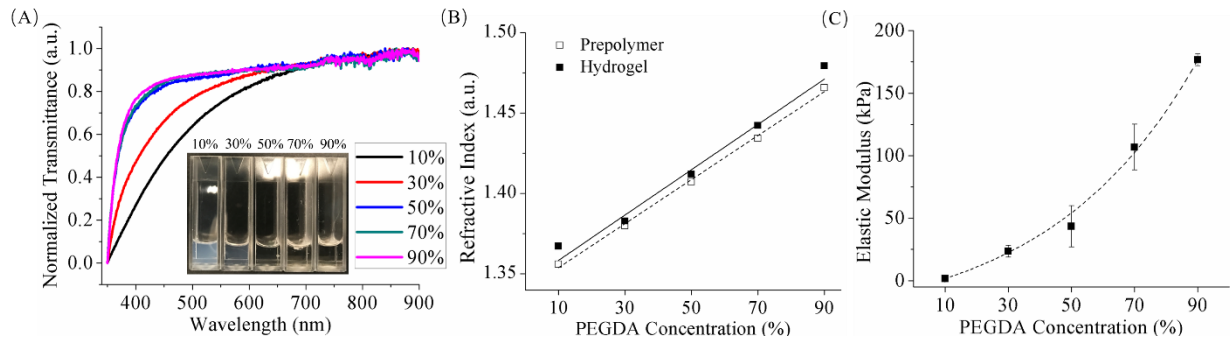


Figure 5.3. Optical and mechanical characteristics of PEGDA hydrogels with varying prepolymer concentrations. (A) Optical transmission spectrum of PEGDA hydrogels. Inset shows photographs of PEGDA hydrogels in cuvette. (B) Refractive indices (RI) of crosslinked (solid) and uncrosslinked (dashed) PEGDA. (C) Elastic modulus of crosslinked PEGDA samples.

5.3.4 Diffraction grating

Diffraction grating is a diffractive optical device with a periodic structure that splits incident light into several beams in different directions based on the spacing of the periodic structure

and the wavelength of the light. Conventional amplitude type phase grating, that consists of an array of transparent and opaque grooves, has lower diffraction efficiency due to loss of light blocked by opaque grooves [47]. As a result, phase-type transmission grating, that consists of π phase transparent grooves, are widely used in the field as they exhibit higher diffraction efficiency. In this work, we designed 1D and 2D phase type transmission gratings based on the relationship between dispersion angle and groove spacing. The property of dispersion when light is normally incident on the micro-optics structures is given by:

$$d \sin \theta_n = n\lambda \quad (1)$$

where d is the groove spacing, n is the diffraction order, λ is the wavelength of the incident light, and θ_n is the diffraction angle of n^{th} diffraction order from the normal.

The digital masks of the gratings were generated as described in **section 2.2**. 1D grating was simulated using interference holography between two plane waves while 2D grating utilized crossed addition of two 1D gratings. The theoretical models of 1D and 2D grating are presented in **SI-3 (A)**. The spacing of the interference fringe pattern (d), similar to the groove spacing input, is determined by the angle α between the two plane waves as given below

$$d = \frac{\lambda}{2\sin(\frac{\alpha}{2})} \quad (2)$$

In this work, the grooves were designed either to be parallel (1D grating) or perpendicular (2D grating). The inputs for groove spacing is $20 \mu\text{m}$ while the wavelength of incident light is 632.8 nm . Based on the **Equation 2**, we calculated the desired angle 1.813° and used it as the initial

parameter for the MATLAB algorithm to generate digital masks (Figure 5.2). The designed patterns of 1D and 2D gratings served as digital masks for the DMD during photo-patterning of PEGDA (**Figure 5.4A**). Printed samples were characterized using optical microscopy (**Figure 5.4B**), phase contrast microscopy (**Figure 5.4C**), and SEM (**Figure 5.4D**). For both 1D and 2D grating, the photo-patterning was able to replicate the 20 μm spacing. SEM images for 2D grating however show some deformation of the pattern possible due to artifacts of sample preparation.

To test the optical performance (angular dispersion) of PEGDA gratings, samples were placed on a slide holder. A monochromatic laser source (632.8 nm) was used to irradiate the samples at a normal angle of incidence, and transmitted diffraction patterns modulated by the gratings were captured on a screen located 100 mm away from the sample and recorded by a digital camera (**Figure S5.1**). Figure 5.4E show the diffraction patterns and their diffraction orders. 1D grating consists of symmetrical spots located on the opposite sides of the screen (X axis), while the diffraction of 2D grating split multiple spots on the horizontal and vertical planes (X and Y axes).

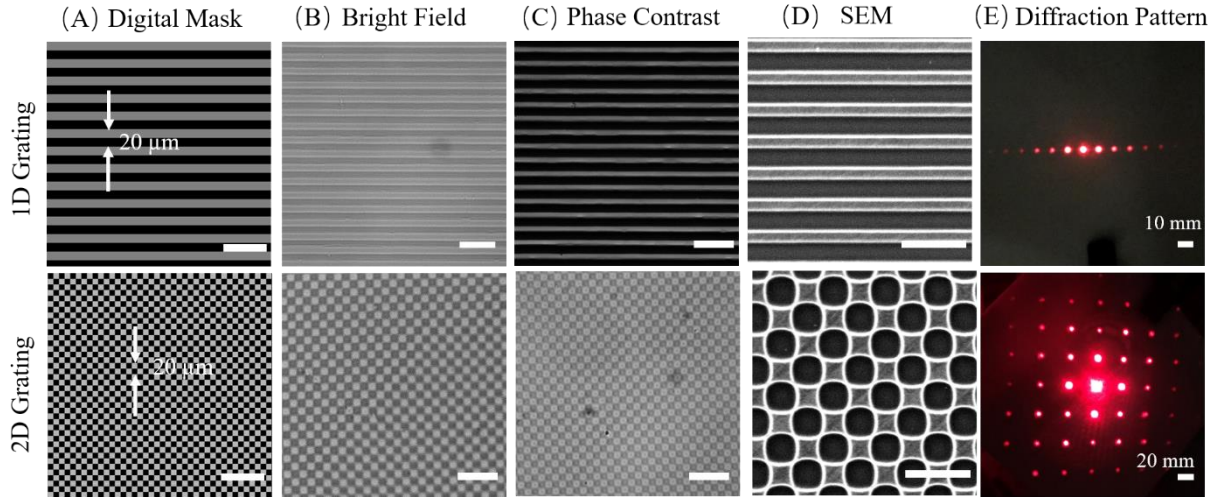


Figure 5.4. Photo-patterning of 1D and 2D diffraction/transmission grating and characterization of their optical properties. (A) Designed patterns. The fabricated grating microstructures were characterized using bright-field microscopy (B), phase contrast microscopy (C) and SEM (D). (E) 2D views of grating diffraction pattern using 632.8 nm He-Ne laser at normal incidence illumination. Scale bar for A-D: 50 μm .

5.3.5 Dammann grating (Beam Splitter)

Beam splitters are binary-phase Fourier holograms able to convert a single incident beam into an array of identical beamlets at its Fourier plane. Although several methods have been implemented to construct such a device, the most popular one is still the binary diffraction gratings proposed by Dammann. This grating, also known as Dammann Grating (DG), splits the incoming beam into several diffraction orders. At the Fourier plane, these diffraction orders are focused into an array of spots with the same intensity [47].

Similar with the 2D diffraction grating design described in **Section 2.4**, 2D DG was constructed by using two crossed 1D DG with 5×5 beam splitting. The digital masks were developed via SCGH which simulates Fourier holography of the beam array with DG and array beams having identical intensity distribution. To design DG masks, iterative Fourier transformation was used with the end condition that is Intensity uniformity, $U < 1\%$ Please refer to Equation 4 and section **SI-3** for details. The optimized digital mask is shown in **Figure 5.5A**.

Printed PEGDA samples were characterized using microscopy and SEM. The phase contrast between crosslinked pattern of DG (white) and surrounding uncrosslinked prepolymer (black) can be seen in Figure 5.5C. As mentioned earlier, SEM images show slight deformation of the pattern due to artifacts during sample preparation. The optical performance of DG patterns in PEGDA samples was evaluated as described in Section 2.4 (Figure 5.5E). Results show that the input laser beam is split into 5×5 unique intensity spots. Since the scattering light from central 0th diffraction order affects the intensity profile, we chose the left first column spots and bottom row spots for characterizing the intensity profile along X and Y direction shown in Figure 5.5F. The intensity uniformity U (Equation 5) along X direction and Y direction are 0.05 and 0.13. These experimental results match well with the theoretical uniformity (U) of 0.01. The slight mismatch could be from scattering at the 0th central diffraction order. PEGDA DG devices can be potentially used for parallel imaging and/or stimulation applications in biophotonics.

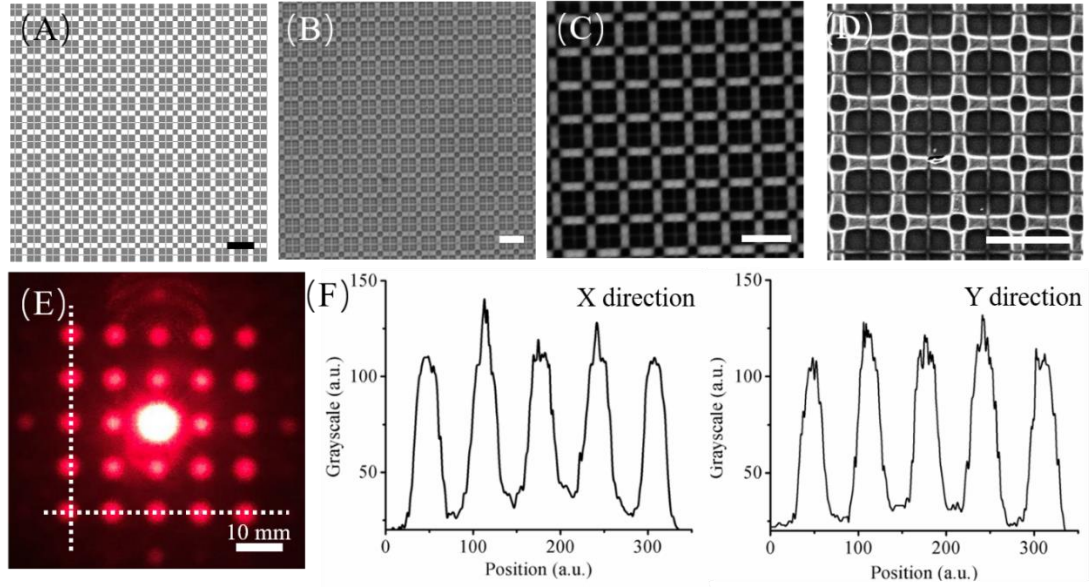


Figure 5.5. Photo-patterning of PEGDA DG device and its optical characterization. (A) Designed mask pattern of 5×5 DG. The fabricated structure was characterized using bright-field microscopy (B) and phase contrast microscopy (C). (D) SEM image shows the close-up view of the micro-structure. (E) Beam splitting performance and intensity cross-section (dotted lines in E) of individual beams along X and Y axis (F). Scale bar A-D: 20 μm .

5.3.6 Fresnel zone plate

Fresnel zone plate (FZP) is a flat/planar lens that consists of a series of radially symmetric rings which diffract light to interfere within a focal length at the center to realize an image. Conventional amplitude type FZP, which consists of alternate transparent and opaque zones, diffracts light from the transparent zones, while phase type FZP, also known as Kinoform phase-type lens, replaces the opaque zones with phase shifting transparent zones [46]. This

results in a higher diffraction efficiency for phase type FZP as compared to amplitude type FZP; as a result, phase type FZP has been widely used in integrated optics and biomedicine.

In this work, we designed a phase type FZP with binary microstructure. The mask pattern of FZP displayed on the DMD is designed using SCGH which simulates the interference between spherical wave and plane wave. (refer to **SI-3C** for details). The radius of successive zones were determined by the distance (f) between dot light source and the holographic plane according to **Equation S12**. In fact, (f) is also the focal length of FZP according to **Equation 6** in section 5. Radius were calculated using the equation $r^2 = fN\lambda$, where r is radius of successive zones, N varying from 1 to 10, λ is the wavelength of light taken as 632.8nm, f is the expected primary focal length as 15.82 mm. The designed mask of FZP consists of 10 zones in which the inner ring of the FZP contains 200 pixels and 3 pixels as the outer ring (**Figure 5.6A**). Bright-field microscopy image of FZP (**Figure 5.6B**) shows a series of concentric annular rings, although the contrast between odd and even zones is difficult to distinguish due to the transparency of PEGDA. SEM image shows strong contrast between the annular grooves (black zones) and the crosslinked hydrogel rings (white zones) (**Figure 5.6C**).

The optical characteristics including light focusing and imaging performance of fabricated FZP were tested using He-Ne laser setup (**Figure S5.1**) and optical setup (**Figure S5.2**) respectively. The image of the focused beam can be seen in **Figure 5.6D**. The FZP produces a clear and well-defined focal spot with concentric diffractive rings whose full width at half maximum (FWHM) is around 18 μm (**Figure 5.6E**). An image of the capital letter “H” was used to analyze the

imaging performance of FZP lens; Figure 5.6E shows a good quality image at the primary focusing length of 15.82 mm. To analyze optical properties at secondary focusing lengths, optical microscope set-up (Figure S5.2) was used; in this setup the light source was replaced with He-Ne laser to measure the focusing lengths (**red solid line in** Figure 5.6G). The experimental results match well with theoretical results (**black dashed line in** Figure 5.6G) calculated using Equation 6. Imaging performance under these focusing lengths were also characterized. As the focusing length decreased, the image size of “H” and corresponding diffraction efficiency decreases. (**Inset in** Figure 5.6G) The diffraction efficiency at the primary focus is around 35.7% which has the slight mismatch with the theoretical result 40.5% calculated by Equation 5, possibly attributed to absorption and scattering of the device. These results demonstrate that the fabricated FZP exhibits visible light focusing and imaging.

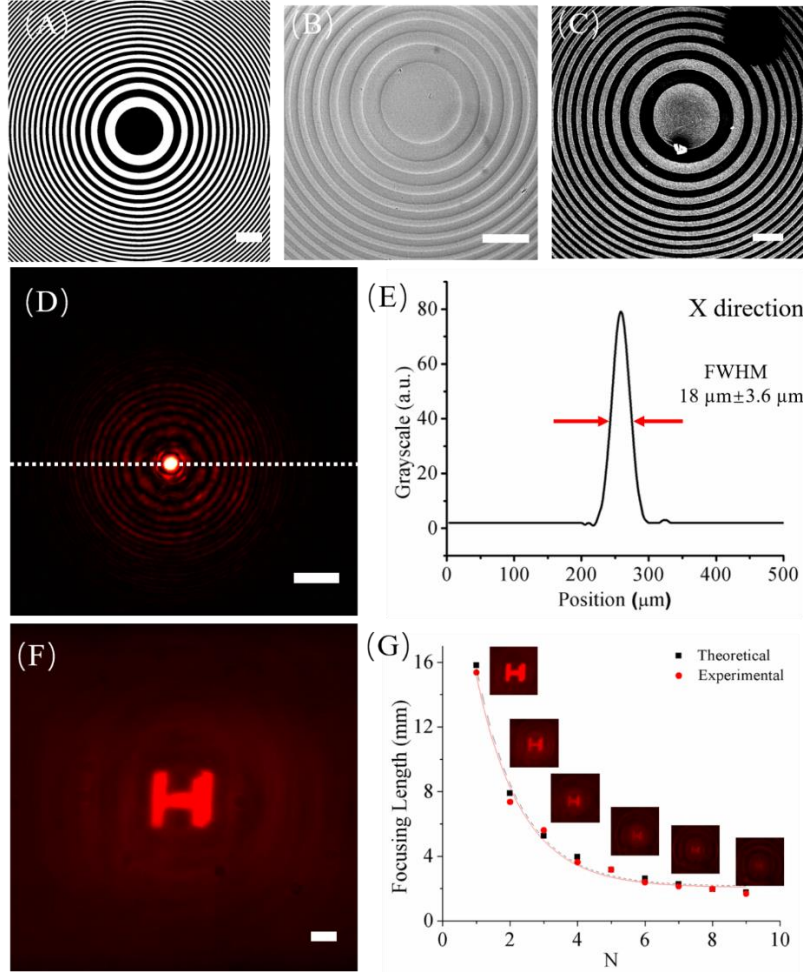


Figure 5.6. Photo-patterning of FZP in PEGDA and characterization of its optical properties.

(A) Designed digital mask of FZP. Images of FZP fabricated from PEGDA were obtained using bright-field microscopy (B) and SEM (C). (D) Image of light focusing by FZP using He-Ne laser. (E) Intensity cross section of focal spot along X direction (dashed line in D). (F) Imaging performance of FZP using a capital letter 'H'. (G) Theoretical and experimental results of primary and secondary focusing lengths. Inset shows the imaging performance for different focus lengths. Scale bar: 100 μm .

5.3.7 Fork-shaped grating

Diffractive optical elements such as spiral phase plate, helical axion, computer-generated holograms (CGH) as well as fork-shaped gratings can be used to generate the optical vortex beam. The transverse cross-sections of the optical vortices are associated with isolated point singularities with helical phase wavefront around them. The central singular point of the helix possesses undefined phase and therefore the intensity vanishing, leading to the characteristic donut beam intensity profile [48]. In biomedical photonics, this special property is often used to manipulate biological cells and proteins [49].

Here, we generate a binary CGH by simulating the interference of optical beams carrying a spiral phase and a tilted wave to obtain a fork grating (also called a vortex grating) which can be utilized to construct the optical vortex beam. The theoretical model of the simulation is presented in **SI-3 (D)**. The vortex grating contains partially approximately parallel lines and has a bifurcated structure (a fork-like pattern) at the center of the pattern, as shown in **Figure 5.7A**. Phase contrast image shows the fork grating (white) and uncrosslinked prepolymer (black) in Figure 5.7C.

The optical characteristics of the fork grating in PEGDA was analyzed using He-Ne laser setup (Figure S5.1). The intensity pattern of the zero and first order diffraction is shown in Figure 5.7E, while the intensity distribution of the first diffraction order at the focus is shown in Figure 5.7F. The intensity is distributed in a donut shape, with the intensity of zero at the center (Figure 5.7G). The FWHM of the central gap is around 14.4 μm . The performance of the hydrogel-based fork grating to reconstruct the optical vortex beam demonstrates that it can be potentially

applied for optical trapping and manipulation of single cell or particle in biophotonic integrated system.

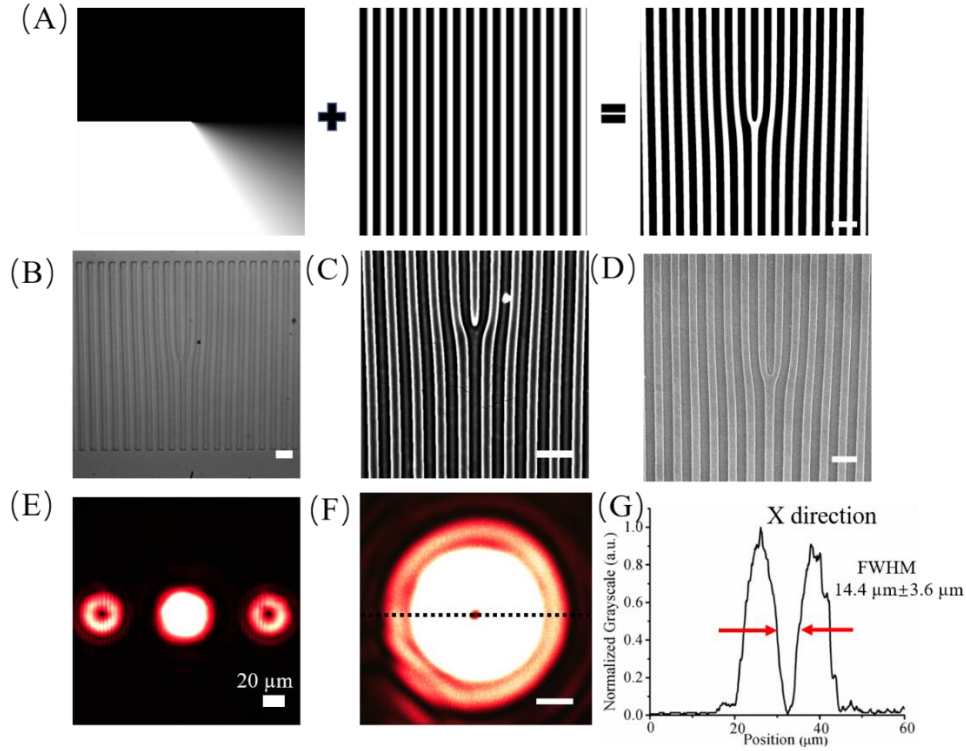


Figure 5.7. Photo-patterning of fork grating and characterization of its optical properties. (A) Generation of digital mask of fork grating by simulating the interference between the optical beams carrying vortex phase and a tilted plane wave. The fabricated fork grating was characterized using bright-field (B) and phase contrast microscopy (C). (D) SEM image. (E) Optical characterization of diffraction pattern (0th and 1st diffraction orders) of fork grating using He-Ne laser. (F) Donut beam of fork grating at the focus and (G) its cross-section of intensity profile in X direction. Scale bar A-D and F: 100μm.

5.3.8 Computer generated hologram (CGH) of arbitrary user-defined pattern

Digital masks of all optical components described in **section 2** were CGHs generated from SCGH technique and then printed on PEGDA films, and subsequently reconstructed by coherent laser source to obtain the desired diffractive patterns. CGH is a kind of diffractive optical element that offers the possibility of creating display systems using digitally generating holographic interference patterns to reconstruct any arbitrary user-defined object [40,50]. To demonstrate the versatility of proposed digital photopatterning, we designed and fabricated the CGH of pattern ‘Syracuse University (SU) Logo’ shown in **Figure 5.8A**. Its digital mask was obtained by simulating the interference between Fourier pattern of SU logo and tilted plane wave (Figure 5.8B). The Fourier pattern of SU logo is generated by iterative Fourier transformation and optimization using Gerchberg-Saxton (GS) algorithm [51]. (Details are reported in **SI-3E**). The digital mask, which consists of an array of vertically microgrooves, was used as input pattern in digital projection photolithography and printed on hydrogel film. Figure 5.8C and Figure 5.8D are bright field image and phase contrast image of the printed device respectively. Figure 5.8E shows a close-up image of these microstructures with a feature resolution of 1 μm . The reconstruction of the CGH was characterized using the experimental set-up described in Figure S5.1. The fabricated device was mounted on a slide holder with a white screen located 100 mm away to capture the diffraction pattern. The white screen was aligned parallel to the surface plane of the hologram substrate and a digital camera was placed in front of the screen. The coherent laser beam at 632.8 nm were normally positioned behind the hologram incident to the substrate. In the transmission mode, the first order diffraction

pattern consisted of two symmetrical SU logo diffraction patterns located on the opposite sides of the center (zero order) (Figure 5.8F). The intensity of left and right sides in Figure 5.8F is slightly weak because of non-uniform illumination from He-Ne laser which follows a standard Gaussian intensity distribution. These results indicate that CGH made in PEGDA can be potentially used to record and reconstruct any arbitrary pattern.

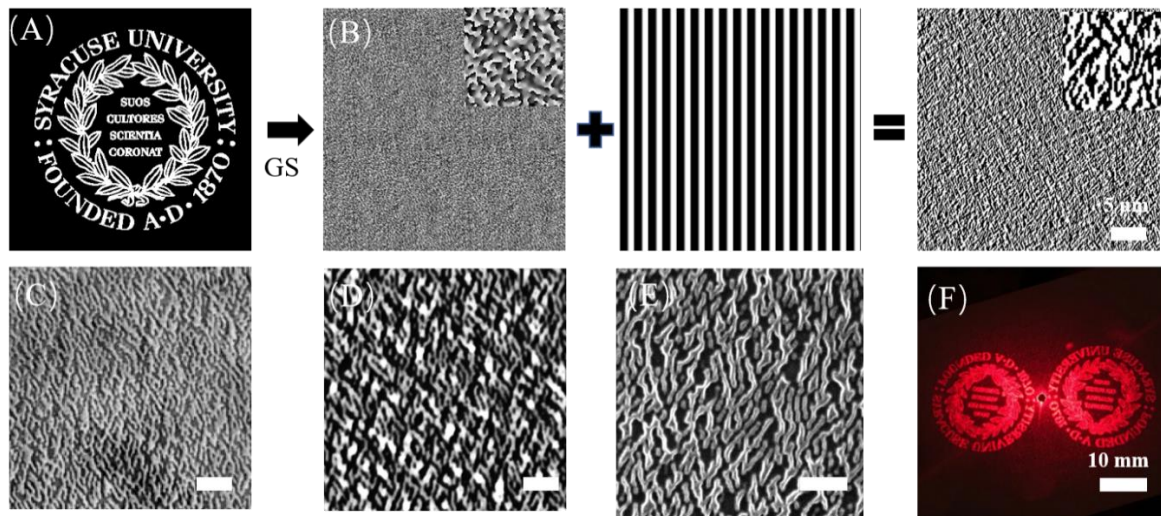


Figure 5.8. Photo-patterning of CGH in PEGDA and characterization of its optical properties.

(A) Desired reconstructed pattern of ‘Syracuse University (SU) Logo’. (B) Generation of digital mask of CGH using the GS algorithm. The CGH of SU logo is interfered with the tilted plane wave to obtain the digital mask for DMD. The fabricated CGH samples were characterized using bright field (C), phase contrast microscopy (D), and SEM (E). (F) The reconstructed diffraction pattern of CGH using He-Ne laser. Scale bar C-E: 20 μm .

5.3.9 Robustness characterization of the printed hDOEs

To address concerns related to the robustness of the printed hDOEs, several control experiments were performed using Dammann Grating (DG) as a model hDOE. To assess the effects of water evaporation through PDMS, DG hDOEs were photo-patterned on PEGDA, and the ‘as printed’ samples (with sealed PDMS spacer) were left in air for 7 days. Brightfield images (**top row – Fig. S5.10**) show that the structure does not change during this period. Diffraction properties of the ‘as printed’ samples, tested using 632.8 nm He-Ne laser at normal incidence illumination, show that the changes in their optical (beam splitting) performance is not significant (**bottom row – Fig. S5.10**). To assess the effect of PDMS spacer removal, DG hDOEs were printed on Day 1, PDMS spacer was removed and the unreacted prepolymer was washed away, and samples were dehydrated in the desiccator for 1, 2, 3 and 4 hours (**top row: Fig. S5.11**). After the dehydration per each hour, samples were rehydrated in prepolymer solution (**middle row: Fig. S5.11**), and the diffraction properties were characterized. Results show that the changes in their optical (beam splitting) performance is not significant. (**bottom row: Fig. S5.11**). In another experiment, samples were printed on Day 1 and the optical performance of ‘as printed’ sample was obtained. Then, PDMS spacer was removed and the unreacted prepolymer was washed away, and samples were dehydrated in the desiccator for 4 hours before characterizing their optical performance. Then, sample was dehydrated for 7 more days in the desiccator and then the sample was rehydrated for few minutes and its optical performance was characterized. Results show that the changes in their optical (beam splitting) performance is not significant. These control experiments show that PEGDA 90% hDOE samples are robust, and the pattern

fidelity and associated optical performance does not change during the dehydration and the rehydration processes.

To assess the effects of long-term laser exposure on printed hDOEs, samples were irradiated for several hours using the He-Ne laser (11mW), however no changes were recorded in the structure and the optical performance of hDOEs. To simulate long exposure durations, we repeated the same experiment with a femtosecond laser (wavelength: 800 nm, frequency: 80 MHz, pulse duration: 140 fs) with 1 W power. **(Fig. S5.12)** After more than 1 hour of exposure, pattern fidelity or the optical performance did not change. Only when a focused laser beam was used, the structure was ablated.

5.4. Discussion

Compact sizes of DOEs, widely used to gain control over light beam properties, are particularly attractive in miniaturization of complicated optical systems. In recent years, hydrogels have emerged as a promising material to develop hDOEs for a range of biomedical applications such as *in vivo* waveguides for light delivery, optical biosensors, optogenetic therapy, and optofluidic devices [22]. Unlike traditional materials which are stiff, difficult to process, and often non-biocompatible, hydrogel exhibits a unique hydrated network of cross-linked hydrophilic polymers making them optically transparent, inert, flexible and biocompatible. However, hDOEs are not widely accepted in the field due to the challenges involved in design and fabrication of customized hDOEs for achieving target optical performance that is comparable to that of conventional materials. In this work, we demonstrate a new design and fabrication

method to convert a widely used photosensitive hydrogel (PEGDA) into an array of optically functional hDOEs, which can be potentially used in the aforementioned applications.

Using PEGDA as our model hydrogel materials, we use digital photopatterning which integrates SCGH (for design of hDOEs) and digital projection photolithography (for fabrication of hDOEs) into a seamless and generic workflow for printing customized hDOEs. Based on user specifications/inputs, digital masks were generated using SCGH and patterned on PEGDA. The ability to customize and rapidly fabricate hDOEs was demonstrated by printing 1D/2D diffraction gratings, Dammann grating, Fresnel Zone Plate (FZP), fork-shaped grating and computer-generated hologram. As compared to conventional indirect methods such as molding, physical mask-based photolithography and dry etching, which are expensive and require exclusive access to microfabrication cleanroom facilities, digital photo-patterning is fast (~2sec per device) and customizable (no need to create a new master mold or a physical mask). As compared to conventional direct methods such as electron beam lithography, interference lithography and femtosecond laser micromachining, our method is inexpensive (no need for specialized and expensive instruments) and easy to implement (no need for technical expertise to operate the patterning platform effectively). As with other technologies, this patterning method also balances feature resolution and exposure overall size. To achieve high feature resolution (1 μm), the printing area in our setup was 2 mm \times 1 mm. Although sub-micron feature resolution is possible by this technology with the use of higher magnification objectives such as 20 \times and 50 \times , this aspect has not been investigated in this report. In the future,

this method can be scaled up by using high-resolution XY scanning and incorporating step-stitching printing strategy.

The optical performance of hDOEs, patterned in this work, was found to be comparable with DOEs made using conventional polymeric materials and fabrication methods as explained below. For instance, 1D/2D phase-type gratings show similar angular dispersion function as transmission grating fabricated (Figure 5.4E), while the transmission efficiency is over 70% which is higher than conventional amplitude type gratings which is less than 50% [26,52]. PEGDA Dammann grating shows 5×5 uniform beamlets at its Fourier plane (Figure 5.5). The intensity uniformity along X and Y direction is smaller than 20% comparable to previously reported Dammann grating made from resin [53–55]. PEGDA FZP (Section 2.6) has similar focusing and imaging function with reported FZP made from photoresist, protein and silk materials [26,28,46]. Experimental diffraction efficiency of PEGDA FZP is 35%; this is close to the theoretically calculated efficiency of 40% and higher than the one reported by amplitude based FZP made in silk materials. PEGDA fork gratings presented a uniform optical vortex beam; devices with similar optical performance have been used for particle and cell manipulation [49,56]. Reconstruction of CGH in PEGDA can precisely record most of the optical information from the input in form of the ‘Syracuse University’ logo. The current design can be further improved by optimizing the algorithm used for SCGH. Although only 5 DOEs were presented in this work, any user-defined DOEs can be generated through SCGH and rapidly printed out using proposed high-resolution photolithography platform.

The potential use of hDOEs in the field is highlighted by the following examples. For instance, photonic microstructure printed on a glucose-selective hydrogel film changed its Bragg diffraction upon exposure to glucose. This film was combined with commercial contact lenses for point-of-care monitoring of glucose using smartphones [23]. In another study, DOEs made from silk hydrogel were developed to monitor both *in vitro* and *in vivo* drug release based on hydration-based diffraction [25]. In another study, soft diffractive micro-optics, called ‘microscale kinoform phase-type lens’ were generated by printing bovine serum albumin (BSA) protein on polydimethylsiloxane (PDMS) films. Laser shaping and imaging function were achieved using these flexible, stretchable, biocompatible and biodegradable lenses, with potential use in foldable optical devices [28]. Lastly, a recent review highlights the use of optically-functional devices such as waveguides, optical fibers, photonic crystals, and plasmonic structures by hydrogels doped with luminescent agents [57]. We envision that instead of replacing conventional photonic materials, hDOEs can be potentially used in applications that require a combination of optical performance and biocompatibility, biological inertness, and mechanical flexibility.

5.5. Conclusion

DOEs, which enable control over light via microstructural organization, have been widely used in imaging, diagnostics and biosensing. Recently, the demand for hydrogel based DOEs has surged as an alternative to conventional DOEs. To enable widespread use of hDOEs, key challenges related to customization and ease/speed of manufacturing need to be addressed. In

this work, we report a new strategy to rapidly design and fabricate customized hDOEs using digital photopatterning technology. This facile approach enabled fast prototyping of hDOEs with optical performance comparable to optical devices made from conventional materials. This strategy can be potentially used to convert any photosensitive biomaterials into user-defined DOEs on demand, and help advance the use of hDOEs in integrative biophotonics and optofluidics applications in the future.

5.6. Experimental Section

PEGDA prepolymer preparation: Poly (ethylene glycol) diacrylate (PEGDA, Mn=700) and PBS were purchased from Sigma-Aldrich and used without further modifications. The photoinitiator, LAP, was synthesized using previously established protocol. The prepolymer solution was composed of varying amounts of PEGDA (10% to 90%, v/v) with LAP (0.25%, w/v for all compositions). The prepolymer solution was mixed for 10 mins using a magnetic stirrer, filtered (pore size=0.2 μ m), and used within 2 days after preparation. Before fabrication, 30 μ L of the prepolymer solution was pipetted on a microscopic glass slide (48 mm \times 24 mm, Fisher Scientific) that was surface modified using Sigmacote (Sigma-Aldrich). A PDMS spacer was placed between the microscope slide (bottom) and methacrylated glass coverslip (top) to control the prepolymer layer thickness to be 20 μ m. **(Figure 5.1 inset)** The coverslip (top) was surface modified to ensure adhesion of crosslinked PEGDA layers during photo-patterning.

Synthesis of photoinitiator: Lithium phenyl-2,4,6-trimethylbenzoylphosphinate (LAP) was synthesized in a two-step process according to established protocols [58]. At room temperature and under argon, 2,4,6-trimethyl-benzoyl chloride (4.5g, 25 mmol) was added dropwise to continuously stirred dimethyl phenylphosphonite (4.2g, 25 mmol). The reaction mixture was then stirred for 24 h and an excess of lithium bromide (2.4g, 28 mmol) into 50ml of 2-butanone was added to the reacted mixture which was then heated up to 50 °C. After 10 mins, a solid precipitate was observed. The mixture was cooled to room temperature, allowed to rest overnight and then filtered. The filtrate was washed with 2-butanone (3x with 25 ml) to remove unreacted lithium bromide and dried under vacuum to obtain LAP (6.2g, 22 mmol, 88%)

Methacrylation of glass coverslip: Glass coverslips were immersed into 10% (w/v) NaOH solution for 30min, and washed in DI water, 75% (v/v) ethanol, and 100% ethanol (performed twice for 3min for each wash). The coverslip was subsequently dried using nitrogen. The dried coverslips then underwent methacrylation by immersing them for 12h in a solution comprised of 85mM 3-(Trimethoxysilyl) propyl methacrylate (TMSPM, Sigma) and ethanol solution with acetic acid (pH 4.5). Finally, the coverslips were washed with ethanol three times and baked for 1h at 100°C.

Optical and mechanical characterization of PEGDA: Refractive indices of prepolymer and crosslinked samples were measured with digital refractometer (Sper Scientific). To measure optical transparency, prepolymer were prepared in standard 1 cm-wide disposable cuvettes, and optical attenuation was measured using scanning spectrophotometer from 250 to 1100 nm

(Thermo Scientific). Mechanical properties were measured using a standard Rheometer (AR2000, TA Instruments, USA). Briefly, samples were prepared by casting the prepolymer solution in PDMS mold (8 mm diameter, 100 μm thickness) and exposing samples to UV light (output power 70 mw cm^{-2} , Ominicure S2000) for 2 minutes. The crosslinked samples were then transferred to the well plates and incubated in ultra-pure DI water for 24 hours to facilitate diffusion of uncrosslinked prepolymer. Next, samples were tested at 25 $^{\circ}\text{C}$ using 8 mm diameter bottom plate with a gap of 0.5 mm. Storage modulus (G') and loss modulus (G'') were measured at 0.5% strain for a range of 0.1-100 Hz. Elastic modulus was calculated by the following **Equation 3** where the Poisson ratio τ was assumed as 0.33. The linear regions of both moduli recorded between 1 and 10 Hz were used to calculate the Elastic modulus (E) [59].

$$E = 2G(1 + \tau) \text{ Where } G = \sqrt{G'^2 + G''^2} \quad (3)$$

Characterization of printed devices: (1) Characterization of micro-patterns. Printed micro-patterns for all devices were characterized using optical microscope, phase-contrast microscope and scanning electron microscope (SEM). The samples for optical microscope (Observer X1, Zeiss, Germany) and phase-contrast microscope (Lecia DM6000, Germany) were kept hydrated. For obtaining SEM images, printed PEGDA samples were separated from their PDMS spacer, washed 3 times with PBS to wash out the unreacted prepolymer, before lyophilizing in a freeze dryer (Labconco, Kansas City, MO) for 24hours. Then the samples were sputter coated with a layer of gold (35 seconds) and imaged under SEM with 8kV eV. (JEOL5600, Japan).

(2) Characterization of optical properties. The details of the setup used to characterize the optical properties of printed devices is illustrated in **Figures S5.1 and S5.2**. The setup in Figure S5.1 is used to characterize the diffraction pattern and diffraction efficiency while the setup in Figure S5.2 is used to characterize the imaging performance of FZP. **Equations 4, 5 and 6** were used to characterize the optical properties of selected DOEs as described below:

Dammann grating: Intensity uniformity of array beams output from Dammann grating [47]

$$U = \frac{I_{max} - I_{min}}{I_{max} + I_{min}} \quad (4)$$

Where U is defined as intensity uniformity, I_{max} is the maximum grayscale intensity of single spot and I_{min} is the minimum grayscale intensity of single spot.

Fresnel Zone Plate (FZP): Diffraction efficiency of FZP is given by[46,60]

$$\eta(n) = \frac{\sin^2\left(\frac{\pi}{n}\right)}{\frac{\pi}{n}} = \text{sinc}^2(1/n) \quad (5)$$

Where η is defined as diffraction efficiency of phase type FZP and n is the level of zone rings which is 2 in this work.

Focusing length of phase type FZP

$$f = \frac{r_N^2}{N\lambda} \quad (6)$$

Where r_N is the radius of successive zones (here is the radius of first ring), f is the focusing length, λ is the wavelength and N is positive integer which is from 1 to 10 in this work.

5.7 Supporting Information

SI-1 Setup to test the optical performance of hDOEs.

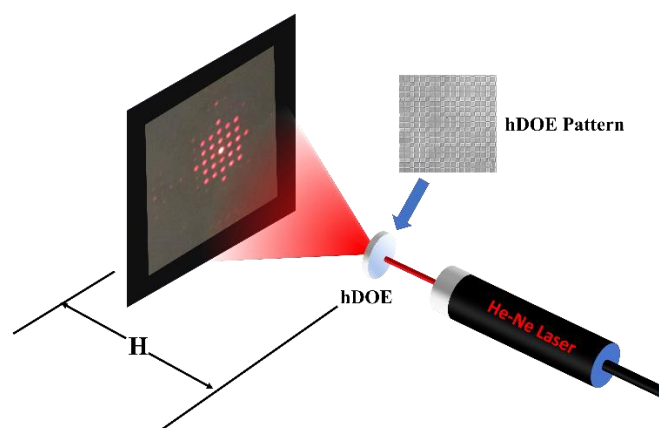


Figure S5.1 Setup to test the optical performance of hDOEs using He-Ne laser. The diffractive optical element was directly illuminated by coherent laser source. An imaging screen was used to capture the diffraction patterns.

SI-2 Setup to test imaging performance of hDOEs.

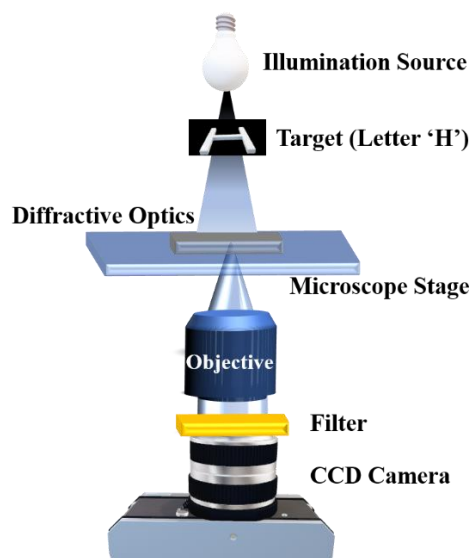


Figure S5.2 Setup to test imaging performance of hDOEs under bright-field microscope. The target, letter ‘H’, was illuminated by bright-field illumination source and imaged by diffractive optics, Fresnel Zone Plate. The image was captured by a CCD camera with objective. A filter was used to block non-visible spectrum.

SI-3 Theoretical model to generate digital mask designs using computer generated holography

(A) Diffraction grating

In order to obtain the digital mask of diffraction grating, we used the computer-generated holography method programmed in MATLAB. The details are shown in Fig. 5.1 and the supporting theoretical model is explained as follows.

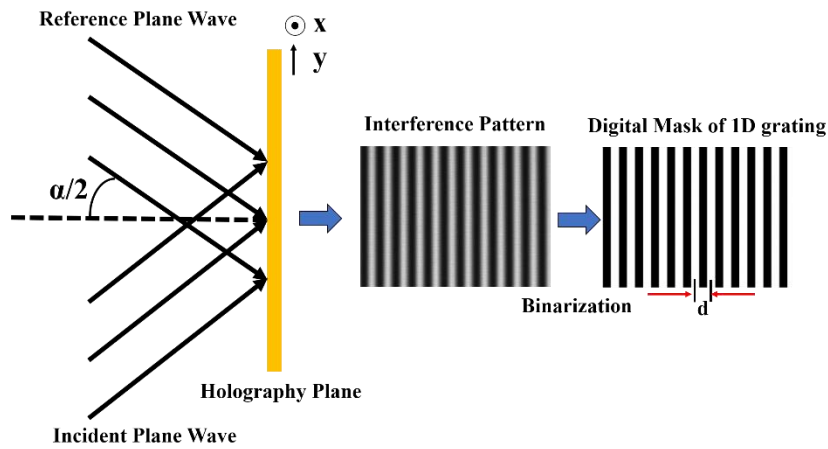


Figure S5.3 Schematic of 1D grating mask design based on two beams holographic interference.

Incident plane wave

$$O(x, y) = O_0 \exp(i\phi_o(x, y)) ; \text{ where } \phi_o(x, y) = \frac{2\pi}{\lambda} \sin(\frac{\alpha}{2})x \quad (1)$$

Reference plane wave

$$R(x, y) = R_0 \exp(i\phi_R(x, y)); \text{ where } \phi_R(x, y) = \frac{2\pi}{\lambda} \sin\left(\frac{\alpha}{2}\right)x \quad (2)$$

Where $O(x, y)$ is the wave equation of the incident light, $R(x, y)$ is the wave equation of the reference light, ϕ represents their phase which is determined by their incident angle α .

For the holographic interference, the intensity distribution $I(x, y)$ of the interference pattern is calculated using the equation

$$I(x, y) = (O + R)(O^* + R^*) = R_0^2 + O_0^2 + 2R_0O_0\cos(\phi_R - \phi_O) \quad (3)$$

The pattern is determined by the phase of the incident and reference lights

$$\phi_R - \phi_O = \frac{2\pi}{\lambda} 2 \sin\left(\frac{\alpha}{2}\right)x = 2m\pi, \text{ where } m=1, 2, \dots, m \quad (4)$$

Therefore, the period d of the interference pattern is calculated as follows

$$d = \frac{\lambda}{2 \sin\left(\frac{\alpha}{2}\right)} \quad (5)$$

2D grating can be designed by simply adding two 1D gratings as shown in **Figure S5.4**.

In the Figure, color red and black represents 1 (corresponds to phase π), while white color represents 0 (0 corresponds to phase 0). After their addition, their transmissions are determined by the conditions shown below in **Figure S5.4**.

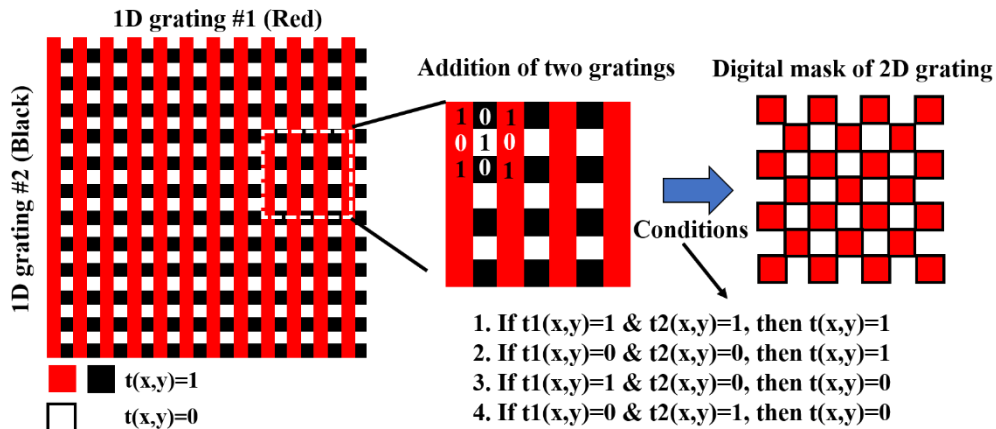


Figure S5.4 Schematic of 2D grating design.

(B) Dammann Grating (Beam Splitter)

Figure S5.5 shows the general shape of a 1D DG. For simplicity we set the period of the grating to unity and require the grating period to be symmetric with respect to the origin. The transmission function has only two values 1 and -1, corresponding to phase value 0 and π respectively. Thus, the grating is characterized by its N transition points, x_1, x_2, \dots, x_N , where the phase jump occurs. The transition points are the variable parameters that are determined by the design procedure such as the diffraction order.

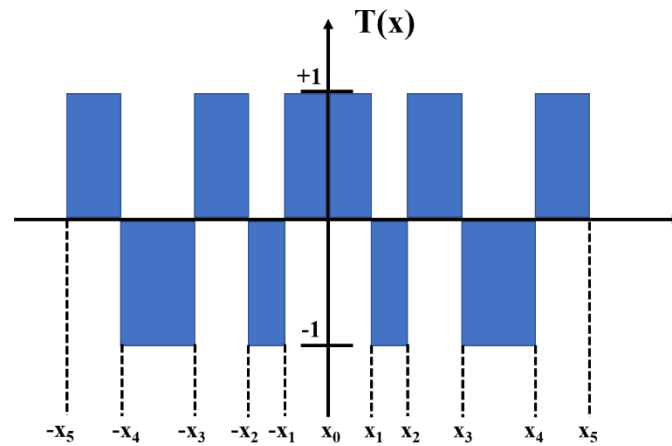


Figure S5.5 One period of transmission function of 1D binary DG.

Due to the symmetry requirements, the positive and negative diffraction orders have the same intensity. DG with N transition points will have $2N+1$ diffraction orders which may be specified in the design. The transmission function $T(x)$ of the grating can be written as

$$T(x) = \sum_{n=0}^N (-1)^n \text{rect}\left(\frac{x - (x_{n+1} + x_n)/2}{x_{n+1} - x_n}\right) \quad (6)$$

The negative part from -N to 0 is chosen symmetrically. By Fourier-transformation of Equation (6), the amplitudes of the diffraction orders can be calculated to be

$$t_m = \frac{1}{\pi m} \sum_{n=0}^N (-1)^n [\sin(2\pi m x_{n+1}) - \sin(2\pi m x_n)] \quad (7)$$

The intensity of the diffraction order is $|t_m|^2$. For a perfect design of a DG, we require the intensity uniformity of the diffraction orders ($m \leq N$) to be smaller than 1%. In this work, N is

2. The iteration Fourier transformation is run using Gercheberg-Saxtion(GS) algorithm which is used to obtain the local optimized result. As we set the period to be unity, the transition points x_0, x_1, x_2, x_3 and x_4 are 0, 0.034837, 0.3869454, 0.6516349 and 1. Therefore, the ratio of width between each transition point is 1:9:7:9 as shown in **Figure S5.6**. Similarly, 2D DG is designed by the addition of two 1D DGs as shown in Figure S5.6. In the Figure, color red and black represents 1, while white color represents 0 (where 1 and 0 correspond to phase π and 0 respectively). Their transmissions (t) are determined by the conditions shown in Figure S5.6.

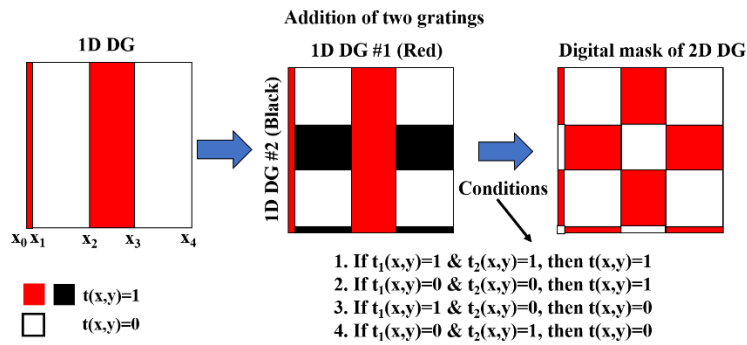


Figure S5.6 Schematic of mask design of 2D DG.

(C) Fresnel Zone Plate (FZP)

In order to generate the digital mask of FZP, we used the computer-generated holography technique. The FZP is obtained through the holographic interferences between incident spherical and reference plane waves. The details are shown in **Figure S5.7** and theoretical model is explained as follows.

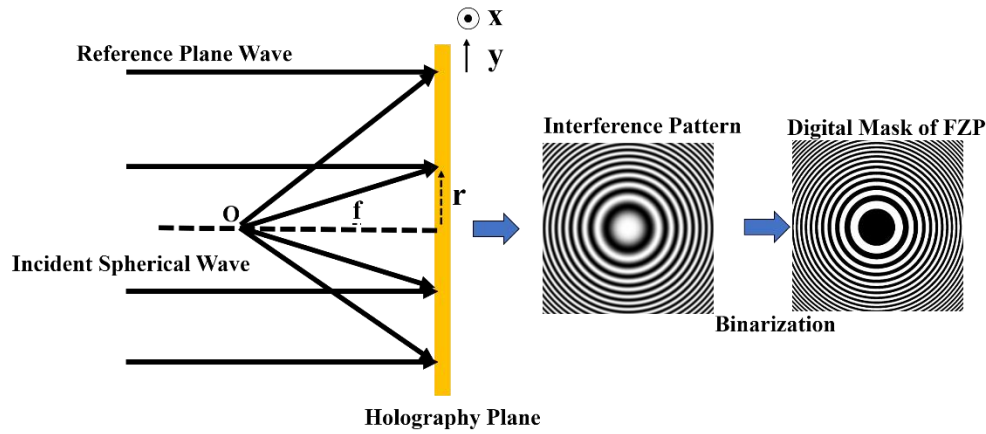


Figure S5.7 Schematic of mask design of FZP based on the interference between spherical and plane waves.

$$O(x, y) = O_0 \exp(i\phi_o(x, y)) ; \text{ where } \phi_o(x, y) = \frac{2\pi}{\lambda} \frac{r^2}{2f} \text{ and } r = \sqrt{x^2 + y^2} \quad (8)$$

$$R(x, y) = R_0 \exp(i\phi_R(x, y)); \text{ where } \phi_R(x, y) = 0 \quad (9)$$

Where $O(x, y)$ is the wave equation of the incident light, $R(x, y)$ is the wave equation of the reference light, ϕ represents their phases which are determined by the position r in holographic plane.

For the holographic interference, the intensity distribution $I(x, y)$ of interference pattern is calculated as

$$I(x, y) = (O + R)(O^* + R^*) = R_0^2 + O_0^2 + 2R_0O_0\cos(\phi_R - \phi_O) \quad (10)$$

The pattern is determined by the phase of incident light and reference light

$$\phi_R - \phi_O = \frac{2\pi}{\lambda} \frac{r^2}{2f} = m\pi, \text{ where } m=1, 2, \dots, m \quad (11)$$

Therefore, the radius of zone rings of FZP is

$$r^2 = fm\lambda \quad (12)$$

Where f is the distance between dot source and holographic plane, the primary focusing length of FZP; m is the interference pattern order.

(D) Fork Grating (FG)

In order to obtain the digital mask of FG, we used the computer-generated holography technique in MATLAB. The FG is generated via holographic interferences between incident, spiral, and reference plane waves. The details are shown in **Figure S5.8** and theoretical model is explained as follows.

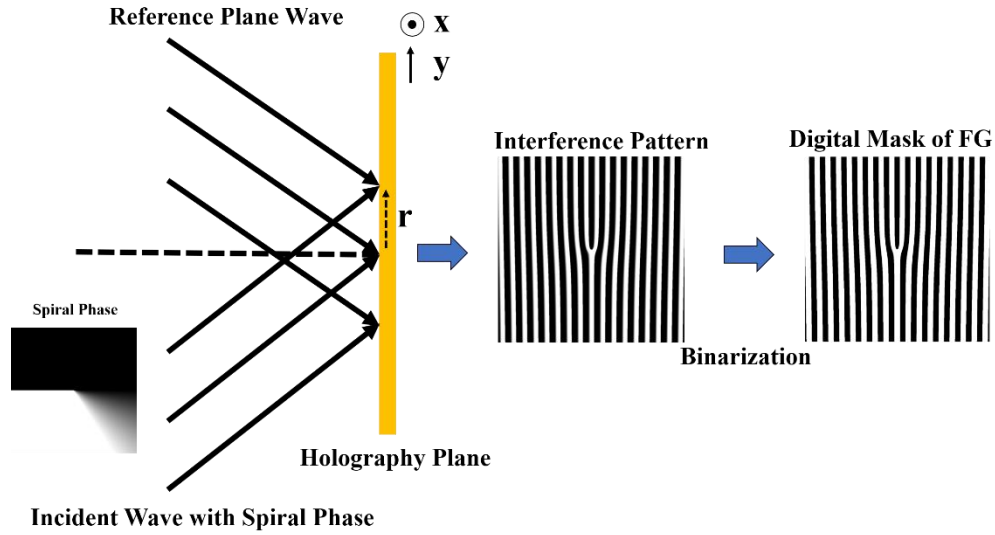


Figure S5.8 Schematic of mask design of FG based on the interferences between wave with spiral phase and plane waves.

$$O(x, y) = O_0 \exp(i\phi_o(x, y)) ; \text{ where } \phi_o(x, y) = \varphi, x = r\cos(\varphi) \text{ and } y = r\sin(\varphi) \quad (13)$$

$$R(x, y) = R_0 \exp(i\phi_R(x, y)); \text{ where } \phi_R(x, y) = \frac{2\pi}{\lambda} \sin(\alpha)x \quad (14)$$

Where the $O(x, y)$ is the wave equation of the incident light, $R(x, y)$ is the wave equation of the reference light and ϕ represents their phase, φ is the azimuth angle in the cylindrical coordinate, r is the radial distance in the cylindrical coordinate and α is the incident angle of plane wave.

The intensity distribution $I(x, y)$ of interference pattern is calculated as

$$I(x, y) = (O + R)(O^* + R^*) = R_0^2 + O_0^2 + 2R_0O_0\cos(\phi_R - \phi_O) \quad (15)$$

The pattern is determined by the phase of incident light and reference light

$$\phi_R - \phi_O = \frac{2\pi}{\lambda} \sin(\alpha) r \cos(\varphi) - \varphi = m\pi, \text{ where } m=1, 2, \dots, m \quad (16)$$

(E) Computer-generated hologram of user-defined object

In order to obtain the digital mask of CGH, we used the computer-generated holography technique. The CGH is obtained through the holographic interference between the Fourier pattern of user-defined object with reference plane wave. The details are shown in **Figure S5.9** and theoretical model is explained as follows.

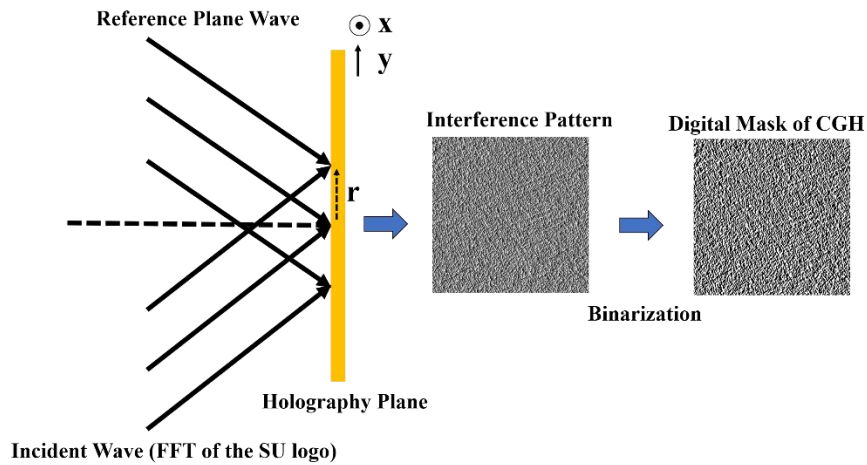


Figure S5.9 Schematic of mask design of CGH based on the interference between Fourier pattern of object and plane wave.

Incident wave

$$O(x, y) = FFT(S(x, y)) = O_0 \exp(i\phi_o(x, y)) \quad (13)$$

Reference plane wave

$$R(x, y) = R_0 \exp(i\phi_R(x, y)); \text{ where } \phi_R(x, y) = \frac{2\pi}{\lambda} \sin(\alpha)x \quad (14)$$

Where $O(x, y)$ is the wave equation of the incident light which is the Fourier transformation pattern of $S(x, y)$, $S(x, y)$ is the optical field distribution of a user-defined object, $R(x, y)$ is the wave equation of the reference light and α is the incident angle of plane wave.

The intensity distribution $I(x, y)$ of interference pattern is calculated

$$I(x, y) = (O + R)(O^* + R^*) = R_0^2 + O_0^2 + 2R_0O_0\cos(\phi_R - \phi_O) \quad (15)$$

The pattern is determined by the phase of incident light and reference light

$$\phi_R - \phi_O = m\pi, \text{ where } m=1, 2, \dots, m \quad (16)$$

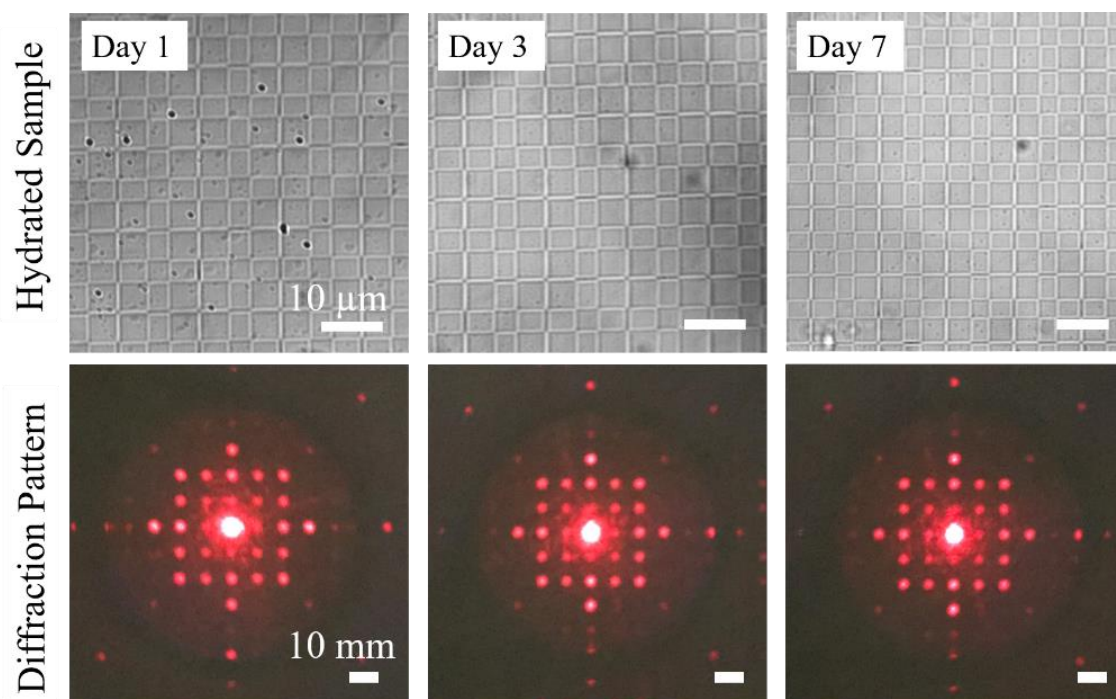


Figure S5.10 Testing the effect of water evaporation on ‘as printed’ Damman grating DOEs

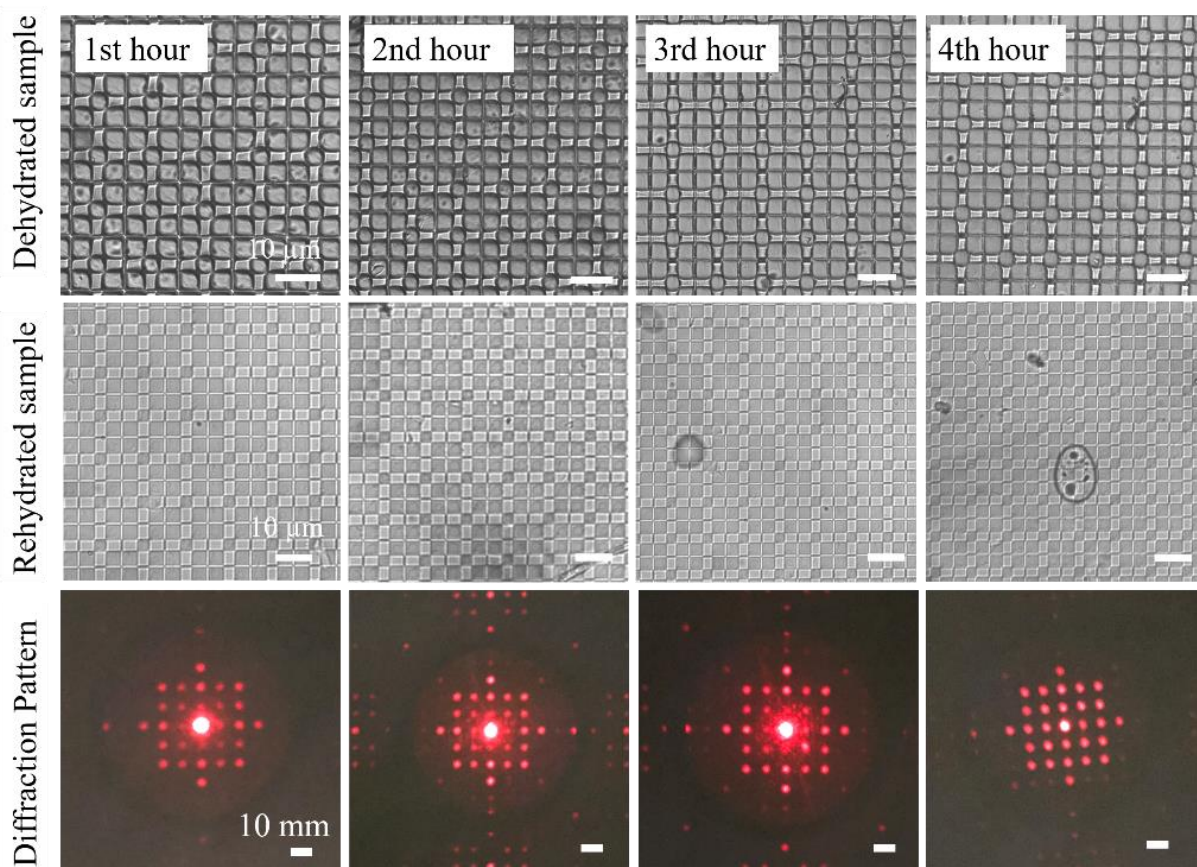


Figure S5.11 Testing the robustness of the Dammann grating DOEs under repeated dehydration and rehydration processes

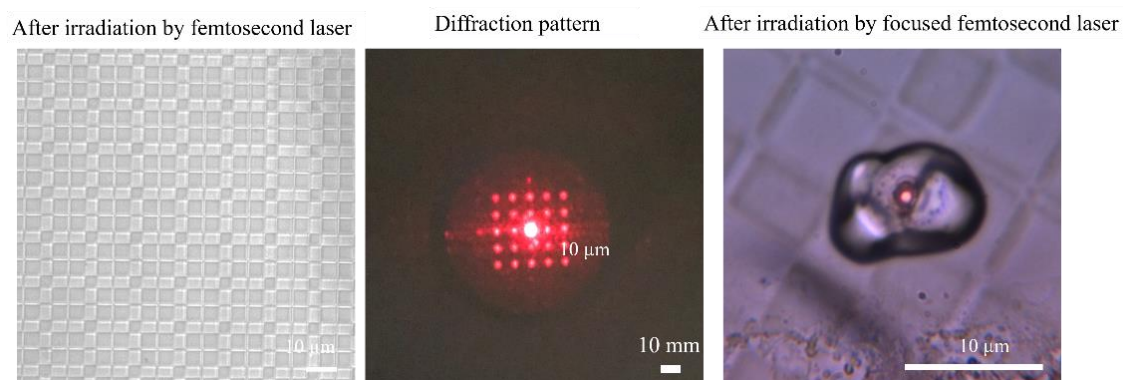


Figure S5.12 Testing the durability of the Dammann grating DOEs under femtosecond laser irradiation (Wavelength: 800nm, Pulse duration: 140fs, Repetition rate: 80MHz, Power: 1W).

5.8. References

- [1] Zhang Y S and Khademhosseini A 2017 Advances in engineering hydrogels *Science* (80-.). **356**
- [2] Elisseeff J 2008 Hydrogels: Structure starts to gel *Nat. Mater.* **7** 271–3
- [3] Kopeček J 2007 Hydrogel biomaterials: a smart future? *Biomaterials* **28** 5185–92
- [4] El-Sherbiny I M and Yacoub M H 2013 Hydrogel scaffolds for tissue engineering: Progress and challenges *Glob. Cardiol. Sci. Pract.* **2013** 38
- [5] Kunwar P, Xiong Z, Zhu Y, Li H, Filip A and Soman P 2019 Hybrid Laser Printing of 3D, Multiscale, Multimaterial Hydrogel Structures *Adv. Opt. Mater.* **7** 1900656
- [6] Xiong Z, Li H, Kunwar P, Zhu Y, Ramos R, McLoughlin S, Winston T, Ma Z and Soman

- P 2019 Femtosecond laser induced densification within cell-laden hydrogels results in cellular alignment *Biofabrication* **11** 35005
- [7] Sanchez-Dealcazar D, Romera D, Castro-Smirnov J, Sousaraei A, Casado S, Espasa A, Morant-Miñana M C, Hernandez J J, Rodríguez I, Costa R D, Cabanillas-Gonzalez J, Martinez R V. and Cortajarena A L 2019 Engineered protein-based functional nanopatterned materials for bio-optical devices *Nanoscale Adv.* **1** 3980–91
- [8] Huang T, Xu H, Jiao K, Zhu L, Brown H R and Wang H 2007 A novel hydrogel with high mechanical strength: A macromolecular microsphere composite hydrogel *Adv. Mater.* **19** 1622–6
- [9] Lawrence B D, Cronin-Golomb M, Georgakoudi I, Kaplan D L and Omenetto F G 2008 Bioactive silk protein biomaterial systems for optical devices *Biomacromolecules* **9** 1214–20
- [10] Kotwal A and Schmidt C E 2001 Electrical stimulation alters protein adsorption and nerve cell interactions with electrically conducting biomaterials *Biomaterials* **22** 1055–64
- [11] Hoare T R and Kohane D S 2008 Hydrogels in drug delivery: Progress and challenges *Polymer (Guildf)*. **49** 1993–2007
- [12] Zhang Y, Yang B, Zhang X, Xu L, Tao L, Li S and Wei Y 2012 A magnetic self-healing hydrogel *Chem. Commun.* **48** 9305–7
- [13] Zhou K, Bisoyi H K, Jin J, Yuan C, Liu Z, Shen D, Lu Y, Zheng Z, Zhang W and Li Q

- 2018 Light-Driven Reversible Transformation between Self-Organized Simple Cubic Lattice and Helical Superstructure Enabled by a Molecular Switch Functionalized Nanocage *Adv. Mater.* **30** 1800237
- [14] Zheng Z, Yuan C, Hu W, Bisoyi H K, Tang M, Liu Z, Sun P, Yang W, Wang X and Shen D 2017 Light-patterned crystallographic direction of a self-organized 3d soft photonic crystal *Adv. Mater.* **29** 1703165
- [15] Poleshchuk A G, Churin E G, Koronkevich V P, Korolkov V P, Kharissov A A, Cherkashin V V., Kiryanov V P, Kiryanov A V., Kokarev S A and Verhoglyad A G 1999 Polar coordinate laser pattern generator for fabrication of diffractive optical elements with arbitrary structure *Appl. Opt.* **38** 1295
- [16] Swanson G J 1989 *Binary Optics Technology : The Theory and Design of Multi-level Diffractive Optical Elements* (MASSACHUSETTS INST OF TECH LEXINGTON LINCOLN LAB)
- [17] Gale M T 1997 Replication techniques for diffractive optical elements *Microelectron. Eng.* **34** 321–39
- [18] Gale M T, Rossi M, Schütz H, Ehbets P, Herzig H P and Prongué D 1993 Continuous-relief diffractive optical elements for two-dimensional array generation *Appl. Opt.* **32** 2526
- [19] Shan D, Gerhard E, Zhang C, Tierney J W, Xie D, Liu Z and Yang J 2018 Polymeric biomaterials for biophotonic applications *Bioact. Mater.* **3** 434–45

- [20] Vörös J, Ramsden J J, Csúcs G, Szendro I, De Paul S M, Textor M and Spencer N D 2002 Optical grating coupler biosensors *Biomaterials* **23** 3699–710
- [21] Chao W, Kim J, Rekawa S, Fischer P and Anderson E H 2009 Demonstration of 12 nm Resolution Fresnel Zone Plate Lens based Soft X-ray Microscopy *Opt. Express* **17** 17669
- [22] Xiong R, Luan J, Kang S, Ye C, Singamaneni S and Tsukruk V V. 2020 Biopolymeric photonic structures: Design, fabrication, and emerging applications *Chem. Soc. Rev.* **49** 983–1031
- [23] Elsherif M, Hassan M U, Yetisen A K and Butt H 2018 Glucose Sensing with Phenylboronic Acid Functionalized Hydrogel-Based Optical Diffusers *ACS Nano* **12** 2283–91
- [24] Yetisen A K, Naydenova I, da Cruz Vasconcellos F, Blyth J and Lowe C R 2014 Holographic sensors: three-dimensional analyte-sensitive nanostructures and their applications *Chem. Rev.* **114** 10654–96
- [25] Zhou Z, Shi Z, Cai X, Zhang S, Corder S G, Li X, Zhang Y, Zhang G, Chen L, Liu M, Kaplan D L, Omenetto F G, Mao Y, Tao Z and Tao T H 2017 The Use of Functionalized Silk Fibroin Films as a Platform for Optical Diffraction-Based Sensing Applications *Adv. Mater.* **29** 1–7
- [26] Pal R K, Kurland N E, Wang C, Kundu S C and Yadavalli V K 2015 Biopatterning of silk proteins for soft micro-optics *ACS Appl. Mater. Interfaces* **7** 8809–16

- [27] Yin M J, Yao M, Gao S, Zhang A P, Tam H Y and Wai P K A 2016 Rapid 3D Patterning of Poly(acrylic acid) Ionic Hydrogel for Miniature pH Sensors *Adv. Mater.* **28** 1394–9
- [28] Sun Y L, Dong W F, Niu L G, Jiang T, Liu D X, Zhang L, Wang Y S, Chen Q D, Kim D P and Sun H B 2014 Protein-based soft micro-optics fabricated by femtosecond laser direct writing *Light Sci. Appl.* **3** e129–e129
- [29] Kurland N E, Dey T, Kundu S C and Yadavalli V K 2013 Precise patterning of silk microstructures using photolithography *Adv. Mater.* **25** 6207–12
- [30] Nie Z and Kumacheva E 2008 Patterning surfaces with functional polymers *Nat. Mater.* **7** 277–90
- [31] Humar M, Kwok S J J, Choi M, Yetisen A K, Cho S and Yun S H 2017 Toward biomaterial-based implantable photonic devices *Nanophotonics* **6** 414–34
- [32] Sun C, Fang N, Wu D M and Zhang X 2005 Projection micro-stereolithography using digital micro-mirror dynamic mask *Sensors Actuators, A Phys.* **121** 113–20
- [33] Xiong Z, Liu H, Chen R, Xu J, Li Q, Li J and Zhang W 2018 Illumination uniformity improvement in digital micromirror device based scanning photolithography system *Opt. Express* **26** 18597
- [34] Xiong Z, Liu H, Tan X, Lu Z, Li C, Song L and Wang Z 2014 Diffraction analysis of digital micromirror device in maskless photolithography system *J. Micro/Nanolithography, MEMS, MOEMS* **13** 043016
- [35] Zhang Y, Luo J, Xiong Z, Liu H, Wang L, Gu Y, Lu Z, Li J and Huang J 2019 User-

- defined microstructures array fabricated by DMD based multistep lithography with dose modulation *Opt. Express* **27** 31956
- [36] Grigoryan B, Paulsen S J, Corbett D C, Sazer D W, Fortin C L, Zaita A J, Greenfield P T, Calafat N J, Gounley J P, Ta A H, Johansson F, Randles A, Rosenkrantz J E, Louis-Rosenberg J D, Galie P A, Stevens K R and Miller J S 2019 Multivascular networks and functional intravascular topologies within biocompatible hydrogels *Science* (80-.). **364** 458–64
- [37] Tumbleston J R, Shirvanyants D, Ermoshkin N, Janusiewicz R, Johnson A R, Kelly D, Chen K, Pinschmidt R, Rolland J P, Ermoshkin A, Samulski E T and DeSimone J M 2015 Continuous liquid interface production of 3D objects *Science* (80-.). **347** 1349–52
- [38] Zheng X, Lee H, Weisgraber T H, Shusteff M, DeOtte J, Duoss E B, Kuntz J D, Biener M M, Ge Q, Jackson J A, Kucheyev S O, Fang N X and Spadaccini C M 2014 Ultralight, ultrastiff mechanical metamaterials *Science* (80-.). **344** 1373–7
- [39] Kunwar P, Jannini A V S, Xiong Z, Ransbottom M J, Perkins J S, Henderson J H, Hasenwinkel J M and Soman P 2020 High-Resolution 3D Printing of Stretchable Hydrogel Structures Using Optical Projection Lithography *ACS Appl. Mater. Interfaces* **12** 1640–9
- [40] Lee W-H 1979 Binary computer-generated holograms *Appl. Opt.* **18** 3661–9
- [41] Leith E N 1969 *Introduction to Fourier Optics* vol 15 (Roberts and Company Publishers)
- [42] Wyrowski F 1990 Diffractive optical elements: iterative calculation of quantized, blazed

phase structures *J. Opt. Soc. Am. A* **7** 961

- [43] Wu Y H, Park H B, Kai T, Freeman B D and Kalika D S 2010 Water uptake, transport and structure characterization in poly(ethylene glycol) diacrylate hydrogels *J. Memb. Sci.* **347** 197–208
- [44] Choi M, Choi J W, Kim S, Nizamoglu S, Hahn S K and Yun S H 2013 Light-guiding hydrogels for cell-based sensing and optogenetic synthesis in vivo *Nat. Photonics* **7** 987–94
- [45] Bolin F P, Preuss L E, Taylor R C and Ference R J 1989 Refractive index of some mammalian tissues using a fiber optic cladding method *Appl. Opt.* **28** 2297
- [46] Chen Q D, Wu D, Niu L G, Wang J, Lin X F, Xia H and Sun H B 2007 Phase lenses and mirrors created by laser micronanofabrication via two-photon photopolymerization *Appl. Phys. Lett.* **91** 171105
- [47] Krackhardt U and Streibl N 1989 Design of dammann-gratings for array generation *Opt. Commun.* **74** 31–6
- [48] Cai X, Wang J, Strain M J, Johnson-Morris B, Zhu J, Sorel M, O’Brien J L, Thompson M G and Yu S 2012 Integrated compact optical vortex beam emitters *Science* (80-.). **338** 363–6
- [49] Jeffries G D M, Edgar J S, Yiqiong Z, Shelby J P, Christine F and Chiu D T 2007 Using polarization-shaped optical vortex traps for single-cell nanosurgery *Nano Lett.* **7** 415–20

- [50] Slinger C, Cameron C and Stanley M 2005 Computer-generated holography as a generic display technology *Computer (Long. Beach. Calif)*. **38** 46–53
- [51] Zalevsky Z, Dorsch R G and Mendlovic D 1996 Gerchberg–Saxton algorithm applied in the fractional Fourier or the Fresnel domain *Opt. Lett.* **21** 842
- [52] Alqurashi T, Montelongo Y, Penchev P, Yetisen A K, Dimov S and Butt H 2017 Femtosecond laser ablation of transparent microphotonic devices and computer-generated holograms *Nanoscale* **9** 13808–19
- [53] Wang W, Zhou C and Jia W 2008 High-fidelity replication of Dammann gratings using soft lithography *Appl. Opt.* **47** 1427–9
- [54] Chen Q-D, Lin X-F, Niu L-G, Wu D, Wang W-Q and Sun H-B 2008 Dammann gratings as integratable micro-optical elements created by laser micronanofabrication via two-photon photopolymerization *Opt. Lett.* **33** 2559
- [55] Li Y, Watanabe W, Tamaki T, Nishii J and Itoh K 2005 Fabrication of Dammann gratings in silica glass using a filament of femtosecond laser *Japanese J. Appl. Physics, Part 1 Regul. Pap. Short Notes Rev. Pap.* **44** 5014–6
- [56] Gahagan K T and Swartzlander G A 1996 Optical vortex trapping of particles *Conf. Proc. - Lasers Electro-Optics Soc. Annu. Meet.* **21** 155–6
- [57] Umar M, Min K and Kim S 2019 Advances in hydrogel photonics and their applications *APL Photonics* **4** 120901
- [58] Fairbanks B D, Schwartz M P, Bowman C N and Anseth K S 2009 Photoinitiated

polymerization of PEG-diacrylate with lithium phenyl-2,4,6-trimethylbenzoylphosphinate: polymerization rate and cytocompatibility *Biomaterials* **30** 6702–7

- [59] Qin X H, Wang X, Rottmar M, Nelson B J and Maniura-Weber K 2018 Near-Infrared Light-Sensitive Polyvinyl Alcohol Hydrogel Photoresist for Spatiotemporal Control of Cell-Instructive 3D Microenvironments *Adv. Mater.* **30** 1705564
- [60] Buralli D A, Morris G M and Rogers J R 1989 Optical performance of holographic kinoforms *Appl. Opt.* **28** 976

CHAPTER 6 : Fabrication of multiscale hydrogel constructs using multiscale DMD-SLA/HLP technology*

6.1 Abstract

Precision micropart is an umbrella term which includes microfluidic devices, molds, and parts several inches in size with some features at the micro- or nanoscale. At present, most of precision microparts with broad applications in cell biology, drug screening, cellular therapy, toxicity testing rely on a photolithography manufacturing method. This method requires the use of sophisticated cleanroom microfabrication facilities and high technical expertise. Although 3D printing has been used to digitally print such microparts, current 3D printing technologies cannot match the printing resolution necessary research applications. The new proprietary technology Hybrid Laser Printing (Chapter 2) can digitally print microparts with build sizes of $2\text{cm} \times 1\text{cm}$ with a feature/channel resolution of $\sim 1\mu\text{m}$. However, many microparts require larger build size while maintaining the high-resolution requirements. This work has designed and built a new multiscale DMD-SLA platform that can interface with HLP and realize a built area of $6\text{ cm} \times 3\text{ cm}$ with a resolution of $1\mu\text{m}$. This work will provide the foundation to provide high-resolution, on-demand, and customized microparts and microdevices without the necessity of using microfabrication cleanroom facilities. Furthermore, a key unmet need of low-volume and low-cost precision microparts provided at rapid turnaround times can be potentially met by this technology.

*This work is sponsored by NSF SBIR Phase I and permitted by 3D Microfluidics LLC.

6.2 Introduction

Due to their ability to manipulate and analyze single cells, microfluidic devices have been used for drug delivery, droplet microfluidics, DNA synthesis, Point Of Care (POC) diagnostics, microarray applications (gene sequencing), fundamental biological research, drug testing, assays for assessing infection, toxicity, cell invasiveness, signaling profiles, differentiation potential, regenerative medicine (scaffolds/textured surfaces for stem cells), as well as tissue chips, organoids research, single cell sorting and analysis, rare cell capture and many others [1–7]. Although there are many ways to make microfluidic devices such as thermoforming (hot embossing, injection molding), laser writing, and newer 3D printing methods, photolithography remains the gold standard for manufacturing high-resolution microfluidic devices for most applications mentioned above [2,8–15].

Photolithography is used to fabricate microfluidic devices using polydimethylsiloxane (PDMS) materials. These devices are typically several centimeters in size with channel or feature resolution of few micrometers. Making these devices involves labor intensive multi-step processes such as dry/wet etching, soft lithography (replica casting using PDMS), punching inlet/outlet access ports, and plasma bonding with a glass substrate. Several of these steps require the use of expensive and exclusive equipment housed in a microfabrication cleanroom facility. This method is slow, expensive, difficult to automate and require high level of technical expertise. This is not ideal for the life sciences research community, that requires quick and cost-effective prototyping of high-resolution devices customized for target applications.

Despite the widespread need, work that requires high-resolution microfluidic devices is largely restricted to customers with expertise in photolithography and access to expensive and exclusive cleanroom facilities. Even among these customers with access to microfabrication facilities, practical constraints such as high costs and high turn-around times, have prevented widespread adoption of high-resolution microfluidic devices.

Compared to the photolithography, additive manufacturing, or 3D printing methods such as Fused Deposition Modeling (FDM), MultiJet Modeling (MJM) and stereolithography (SLA), can provide customized microfluidic devices in a cost effective and quick manner. Already, biologists, chemists, and engineering researchers, with no previous experience in microfabrication or cleanroom-based technologies, have designed and printed customized microfluidic for their own niche applications. However, these applications are limited to millifluidic regime rather than truly microfluidic regime due to the low printing resolution of current methods (typically $>100\mu\text{m}$). Therefore, there is a need to develop new printing methods capable of manufacturing high-resolution microfluidic devices that matches or come close to the current gold standard of photolithography.

The proprietary hybrid laser printing (HLP) technology, which can potentially replace the current gold standard of photolithography, combines the quick and large-scale printing capability of Continuous Liquid Interface Production (CLIP) with precision processing of additive multiphoton polymerization (MPP) and subtractive multiphoton ablation (MPA) into a single versatile machine. However the build area is limited to $2\text{cm} \times 1\text{cm}$, which limits its

utility for many applications. In this work, we develop a new multiscale DMD-SLA modality which can be integrated with current HLP technology to achieve a large build area of $6\text{ cm} \times 3\text{ cm}$ while maintaining a high resolution of $\sim 1\text{-}3\text{ }\mu\text{m}$.

6.3 Multiscale stereolithography System

The HLP technology, described in Chapter 2, has two challenges before it can be used for making microparts for real-world applications. The first being the development of a new material library that can not only be processed by HLP technology but also exhibit acceptable biocompatibility for a range of biomedical applications. The second being the scaling up of the print area by at least 3 folds from its current size . In this work, we have solved the first ‘materials’ challenge by developing new formulations of photocrosslinkable polymers with acceptable mechanical properties. The second ‘scalability’ challenge was addressed by designing a new multiscale DMD-stereolithography module that can interface with the HLP module (**Figure 6.1**). Similar to any 3D printing platform, conventional digital micromirror device (DMD) based 3D printing sytem also have to balance print size/area and print resolution. Typical, for a print size of 1cm^2 , you can achieve a resolution of $10\mu\text{m}$. As you scale up and increase print size, the resolution decreases by the same amount. In this work, we develop a novel DMD-SLA system with printingresolution of $10\text{ }\mu\text{m}$ while maintanang a large print area of $6\text{ cm} \times 3\text{ cm}$. In the future, this could be integrated with MPP and MPA modes of HLP to realize a fully automated HLP 2.0 machine with high printing area while maintaining $1\mu\text{m}$ printing resolution.

This new system consists of a multiscale light engine which includes an illumination subsystem, a projection subsystem, an accessory opto-mechanical assembly as well as a GUI control interface. This modular design ensures high flexibility of print area and resolution based on the requirements for target applications. Although the proprietary design is not presented in this work, the resulting capabilities are highlighted below. The uniformity of the illumination system is over 95%, with distortion of the projection system less than 0.05%, and a vertical printing speed of 120mm/hr when a high-power LED is used as the light source.

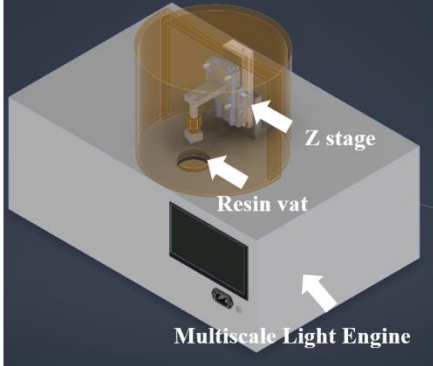
Multiscale System	Specifications	
	Light source	LED 365 nm/ Laser 405nm
	Printing dimension	62.1 × 34.8 × 50 mm
	XY resolution	10 μm
	Z resolution	3 μm
	Material	PEGDA
	GUI interface	Labview
	Distortion	<0.1%
	Speed	40-100+ mm/hr
	File	STL, PNG

Figure 6.1 Multiscale microstereolithography module. The novel multiscale system, which consists of a multiscale light engine, resin vat and Z stage, upgrades CLIP in original HLP system with higher resolution down to 10 μm and fast/largescale fabrication.

To validate the system performance, we have printed 3D models (**Figure 6.2**) such as Mayan pyramid and the Empire State Building. From the digital microscope (HIROX, Japan) images, the small features such as the steps of the pyramid and the windows of the building, can be easily distinguished. From the SEM (JEOL5600, Japan) images, the features crosslinked via

single pixel light exposure can be also differentiated from the zoomed in image of the pyramid.

The total printing time for one model takes less than 5 mins proving a proof of the systems' rapid printing capability.

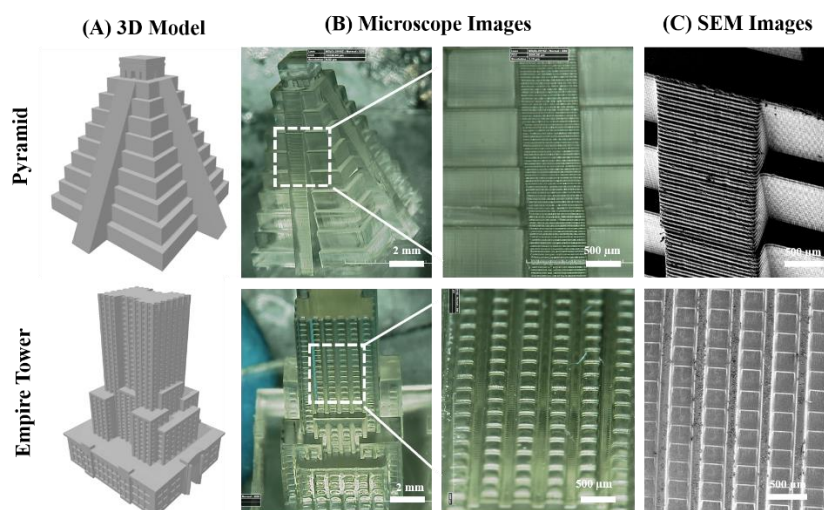


Figure 6.2 Printed 3D models (Mayan pyramid and Empire State building). (A) 3D CAD models are printed using multiscale system and imaged under digital microscope (B) and using SEM (C).

6.4 3D Microfluidic Chips

Through an iterative material discovery and development, we have optimized a photopolymer formulation that can reliably use to print 3D models (**Figure 6.2**). For this work, a series of photo-initiators and photo-absorbers with varying concentrations were used. Specifically, photoabsorber decreases the light penetration during the printing process; this is important to develop hollow features, such as microchannels, without any defects, such as clogging of the

channel, due to over-crosslinking. For the photoabsorber, the following criteria was used (1) optimal spectral overlap with light source, (2) colorless (transparency is important for many biomedical applications), & (3) solubility in polymer. The optimized formulation was used to print 3D microfluidic models (**Figure 6.3**). Post-printing, the models were cleaned with Ethanol and compressed nitrogen gas, and then post-cured under UV lamp for 60s (Ominicure S2000, Canada). To visualize the internal channels, green and red food dye was perfused and HIROX was used to take images. Results demonstrate that dye can perfuse within channels without any diffusion within the material; this is important as diffusion is observed in most hydrogel which does not satisfy the criteria for use in the field of microfluidics.

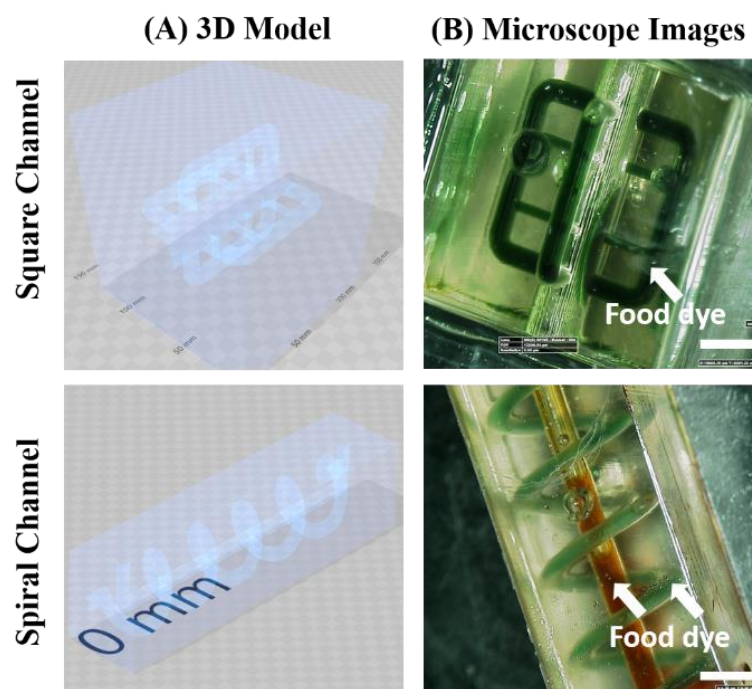


Figure 6.3 Printed 3D microfluidic models (square and spiral channel). (A) 3D CAD models are printed using multiscale system and (B) imaged under digital microscope. Green and red dye flowing inside the microchannels. Scale bar: 500 μm .

To further verify the system resolution and printing flexibility, we have used the proposed material composition to fabricate single pixel (10 μm) width (Figure 6.4 (A)) microchannels and complex microfluidic alveoli-like model (Figure 6.4 (B)). In Figure 6.4 (B), the food dye flows easily through the side channels (10 μm) between the two main channels (100 μm). This result proves that our multiscale system can reach to the theoretical resolution as specified in Figure. 6.1. In Figure 6.4 (B), a complicate alveoli model is fabricated with embedded air sac (Red dye). The user-defined channel shapes with flowing green dye proves that the multiscale system can print the microfluidic device with customized shapes with high design flexibility in 3D.

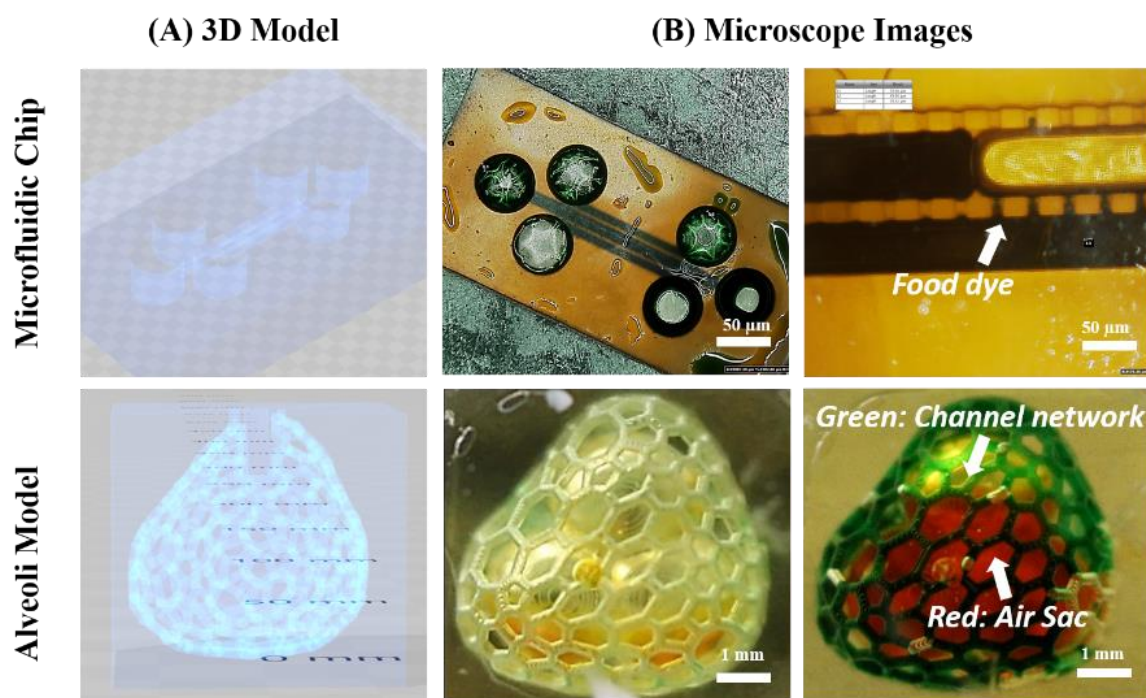


Figure 6.4 Printed 3D microfluidic chips (microchannel and Alveoli). (A) 3D CAD models are printed using multiscale system and (B) imaged under digital microscope. Green and red dye flowing inside the microchannels.

Using this new multiscale DMD-SLA system, the print area was increased from $2\text{ cm} \times 1\text{ cm}$ to $6\text{ cm} \times 3\text{ cm}$, while the resolution was maintained at $10\text{ }\mu\text{m}$ as compared to conventional system's resolution of more than $50\text{ }\mu\text{m}$. At present, we have not integrated and automated a new HLP that combines multiscale DMD-SLA with HLP. This future work can potentially replace the need of exclusive and expensive microfabrication cleanroom facilities and help democratize the use of sophisticated microfluidic devices and microparts.

To show that integration between new DMD-SLA and HLP is possible, we choose a real-world case study. The customer need was to enable co-culture of multiple cells with defined cell-cell connection on top of a multi-electrode array located at the bottom of a 6-well plate. Based on customer specifications, multiscale DMD-SLA was used to print an insert with height of 1.5 cm and a diameter of 2.5 cm . Insert consist of three micro culture wells with $200\text{ }\mu\text{m}$ diameter with partition walls to enable culture of two different cell types with two media formulations. The subtractive mode of HLP was used to ablate several microchannels $5\text{ }\mu\text{m}$ in width; upon cell culture, these microchannels would enable cell-cell connection between inter- and motor-neurons. Such a device is not possible with any other current 3D printing method. In the future the integrated DMD-SLA and HLP system will allow automated printing of microparts that are

either (i) technically challenging to print, and/or (ii) extremely time consuming to manufacture, and/or (iii) not possible with current technologies We believe that such printers will open doors to widespread commercialization.

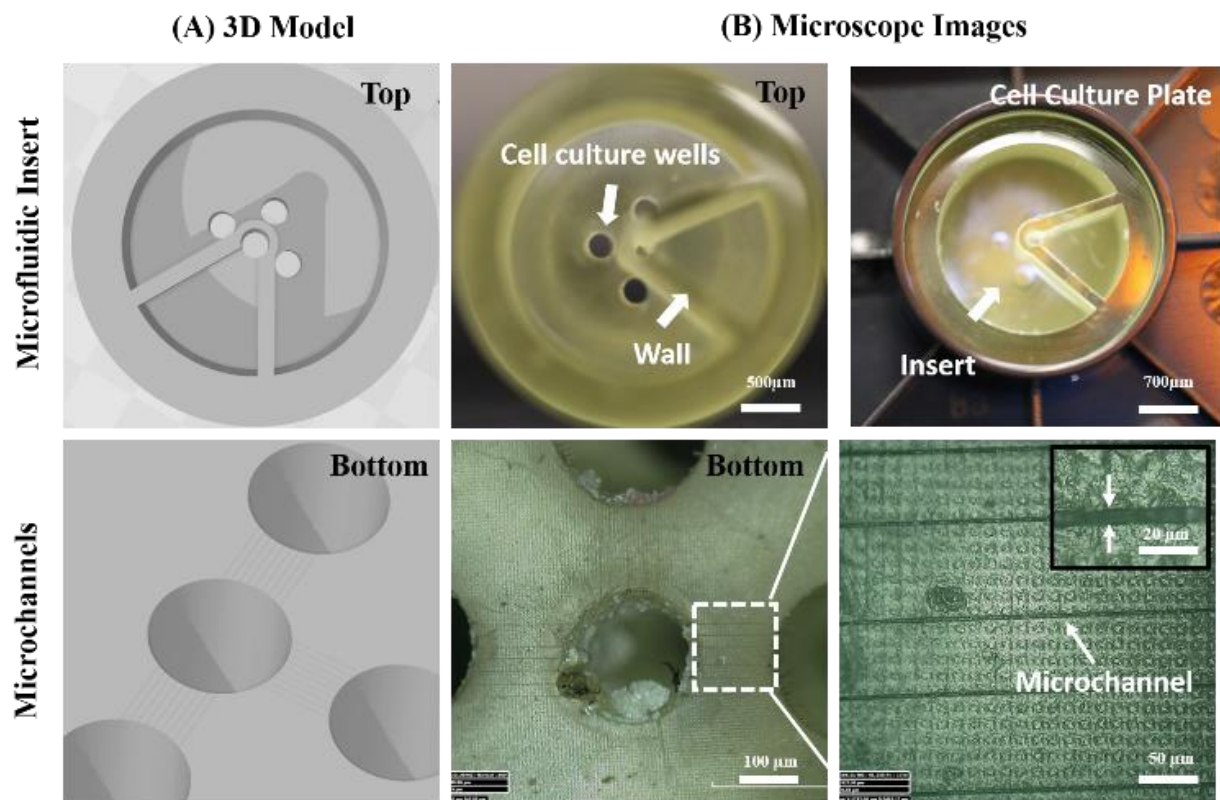


Figure 6.5 Printed 3D microfluidic insert. (A) 3D CAD models are printed using multiscale system and (B) imaged under digital microscope.

6.5 References

- [1] Ho C M B, Ng S H, Li K H H and Yoon Y-J 2015 3D printed microfluidics for biological applications *Lab Chip* **15** 3627–37
- [2] Au A K, Huynh W, Horowitz L F and Folch A 2016 3D-printed microfluidics *Angew. Chemie Int. Ed.* **55** 3862–81

- [3] He Y, Wu Y, Fu J, Gao Q and Qiu J 2016 Developments of 3D printing microfluidics and applications in chemistry and biology: a review *Electroanalysis* **28** 1658–78
- [4] Nichol J W, Koshy S T, Bae H, Hwang C M, Yamanlar S and Khademhosseini A 2010 Cell-laden microengineered gelatin methacrylate hydrogels *Biomaterials* **31** 5536–44
- [5] Wu F and Dekker C 2016 Nanofabricated structures and microfluidic devices for bacteria: from techniques to biology *Chem. Soc. Rev.* **45** 268–80
- [6] Lu Y, Mapili G, Suhali G, Chen S and Roy K 2006 A digital micro-mirror device-based system for the microfabrication of complex, spatially patterned tissue engineering scaffolds *J. Biomed. Mater. Res. - Part A* **77** 396–405
- [7] Du G, Fang Q and den Toonder J M J 2016 Microfluidics for cell-based high throughput screening platforms—A review *Anal. Chim. Acta* **903** 36–50
- [8] Au A K, Lee W and Folch A 2014 Mail-order microfluidics: evaluation of stereolithography for the production of microfluidic devices *Lab Chip* **14** 1294–301
- [9] Bhattacharjee N, Urrios A, Kang S and Folch A 2016 The upcoming 3D-printing revolution in microfluidics *Lab Chip* **16** 1720–42
- [10] Waheed S, Cabot J M, Macdonald N P, Lewis T, Guijt R M, Paull B and Breadmore M C 2016 3D printed microfluidic devices: enablers and barriers *Lab Chip* **16** 1993–2013
- [11] Yazdi A A, Popma A, Wong W, Nguyen T, Pan Y and Xu J 2016 3D printing: an emerging tool for novel microfluidics and lab-on-a-chip applications *Microfluid. Nanofluidics* **20** 50

- [12] Kim P, Kwon K W, Park M C, Lee S H, Kim S M and Suh K Y 2008 Soft lithography for microfluidics: a review
- [13] Chen C, Mehl B T, Munshi A S, Townsend A D, Spence D M and Martin R S 2016 3D-printed microfluidic devices: fabrication, advantages and limitations—a mini review *Anal. Methods* **8** 6005–12
- [14] Walsh III D I, Kong D S, Murthy S K and Carr P A 2017 Enabling microfluidics: from clean rooms to makerspaces *Trends Biotechnol.* **35** 383–92
- [15] Tsao C-W 2016 Polymer microfluidics: Simple, low-cost fabrication process bridging academic lab research to commercialized production *Micromachines* **7** 225

CHAPTER 7: Dissertation Summary

In this thesis, an array of new 3D printing and processing technologies were designed and developed for shaping hydrogels to generate functional devices and tools for potential applications in the fields of tissue engineering, biophotonics, microfluidic devices and single cell biology.

In chapter 2, a new HLP technology was designed and developed; HLP seamlessly combines additive crosslinking and subtractive ablation modes of femtosecond laser to achieve the printing of 3D multiscale multi-material structures using difficult-to-process hydrogel materials. Quick fabrication of multiscale structures with embedded hollow microfeatures demonstrates superior design flexibility of HLP and similar feature resolution as compared to conventional lithography methods. The ability to print multi-materials in additive-additive and additive-subtractive modes demonstrates the fabrication versatility of HLP and its potential use cases in biomedical sciences, microfluidics, soft robotics, optics, photonics and other application areas.

In Chapter 3, a new hydrogel modification phenomenon coined as ‘fs-laser induced densification’ was discovered using model GelMA hydrogels. It was found that introduction of densified line-patterns within cell-laden GelMA resulted in preferential and localized cellular alignment. This method is capable of aligning variety of encapsulated cells in user-defined

patterns, and these patterns can be introduced during ongoing cell culture experiments. This work can be used to study fundamental single cell behavior encapsulated within 3D gels.

In Chapter 4, femtosecond laser induced densification phenomenon was found to modulate the refractive index of model PEGDA hydrogels. This method was used to introduce variety of beam shapers within bulk PEGDA hydrogels. This work shows good potential for developing next-generation integrated biophotonic devices.

In chapter 5, a new strategy to rapidly design and fabricate customized hDOEs using multiscale stereolithography (additive module) was also demonstrated. This method enabled fast prototyping of hDOEs with optical performance comparable to optical devices made from conventional materials. This strategy can potentially be used to convert any photosensitive biomaterials into user defined DOEs and help advance the use of hDOEs in integrative biophotonics and optofluidic applications in the future.

Lastly, we demonstrated the feasibility of integrating a multiscale DMD-SLA with HLP technology to generate an advanced HLP platform with large print area of 6cm×3cm while maintaining the feature resolution to $\sim 1\mu\text{m}$. HLP-printed devices will potentially provide high-resolution, on-demand, and customized microfluidic devices and microparts at low-cost and without the need to have access and technical expertise to sophisticated microfabrication cleanroom facilities, thus paving the way to commercialization.

VITA

ZHENG XIONG

EDUCATION

Syracuse University 2021

Ph.D. in Biomedical Engineering (Optical Engineering Focus)

University of Chinese Academy of Sciences 2016

M.S. in Optics/Optical Engineering

Changchun University of Science and Technology 2011

B.S in Optical Information Science and Technology (Laser Optics Focus)

EXPERIENCE

1. 3D Microfluidics LLC 2020- 2021

CTO/Principal investigator of NSF SBIR Award

2. Syracuse Biomaterials Institute 2016 - 2021

PhD research assistant

3. Changchun Institute of Optics, Fine Mechanics and Physics 2012– 2016

Master research assistant

SELECTED PUBLICATIONS

1. **Z. Xiong**, et al. “In-gel volume grating realized by femtosecond laser induced densification”
(under preparation)
2. M.Y. Tan, **Z. Xiong**, et al, “Double-sided micro-optical system using image processing assisted laser 3D printing”, *Optics Letters* (under review)
3. S.P. Guo, Z.F. Lu, **Z. Xiong**, et al, “Lithographic pattern quality enhancement of DMD lithography with spatiotemporal modulated technology”, *Optics Letters* (2021)
4. **Z. Xiong**, et al., “Hydrogel based diffractive micro-optics using rapid digital photopatterning”, *Advanced Optical Materials* (2021)
5. P. Kunwar, **Z. Xiong**, et al., “Oxygen-Permeable Films for Continuous Additive, Subtractive, and Hybrid Additive/Subtractive Manufacturing”, *3D Printing and Additive Manufacturing* (2020)
6. P. Kunwar, A.J. Jannini, **Z. Xiong**, et al, “High-resolution 3D printing of stretchable hydrogel structures using optical projection lithography”, *ACS Applied Material & Interface* (2019)
7. **Z. Xiong**, et al., “Femtosecond laser induced densification within cell-laden hydrogels results in cellular alignment”, *Biofabrication* (2019)
8. Y. Zhang, J. Luo, **Z. Xiong**, et al, “User-defined microstructures array fabricated by DMD multistep lithography with dose modulation”, *Optics Express* (2019)
9. P. Kunwar, **Z. Xiong**, et al., “Hybrid laser platform for printing 3D multiscale multi-material hydrogel structures”, *Advanced Optical Materials* (2019)

10. **Z. Xiong**, et al. "Illumination uniformity improvement in DMD based scanning photolithography system", *Optics Express* (2018)
11. **Z. Xiong**, et al., "Diffraction analysis of digital micromirror device in maskless photolithography system", *Journal of Micro/Nanolithography, MEMS, and MOEMS* (2014)

AWARDS AND HONORS

- Syracuse university graduate dean excellent research award 2021
- SPIE optics and photonics education scholarship 2020
- NSF SBIR Phase I award 2020
- Syracuse university PhD dissertation award 2020
- Syracuse university PhD fellowship 2016
- Chinese national scholarship for outstanding master student 2014
- Reviewers for 20 peer-reviewed journals and 4 international conferences.

CONFERENCE PRESENTATIONS

1. **Zheng Xiong**, "Digital printing of hydrogel based diffractive optical elements", 2021 SPIE photonics west, Feb. 2020, San Francisco, CA (Oral talk and proceeding paper)
2. **Zheng Xiong**, "Hybrid Additive-Subtractive Laser Fabrication Platform for Shaping Hydrogels", 2020 SPIE photonics west, Feb. 2020, San Francisco, CA (Invited oral talk)
3. **Zheng Xiong**, "Femtosecond laser induced densification within cell-laden hydrogels results in cellular alignment", 2020 SPIE photonics west, Feb. 2020, San Francisco, CA. (Oral talk and proceeding paper)

4. Pranav Soman, Puskal Kunwar, **Zheng Xiong**, etc. "Hybrid Additive-Subtractive Laser Fabrication Platform for Shaping Hydrogels", 2019 Society of Biomaterials Annual Meeting, April 2019, Seattle, Washington.
5. **Zheng Xiong**, "3D Multiscale/Multimaterial Laser Printing Platform for Shaping Hydrogel", 2019 ECS Research Day, March 2019, Syracuse, New York. (First Place Prize in Poster & Second Place Prize in Oral)
6. **Zheng Xiong**, "Femtosecond laser induced densification within cell-laden hydrogels results in cellular alignment", 2019 Stevenson Biomaterials Lecture and Research Poster Session, March 2019, Syracuse, New York. (First Place Prize)
7. **Zheng Xiong**, "High resolution laser processing of cell-laden gelatin methacrylate", 2017 Biomedical Engineering Society Annual Meeting, October 2017, Phoenix, Arizona.
8. **Zheng Xiong**, "Two-photon laser processing of gelatin methacrylate", 2017 ECS Research Poster Competition, April 2017, Syracuse, New York.
9. **Zheng Xiong**, "Two-photon laser processing of gelatin methacrylate", 2017 Society of Biomaterials Annual Meeting, April 2017, Minneapolis, Minnesota. (STAR Award & First Place Prize)
10. **Zheng Xiong**, "Femtosecond laser processing of gelatin methacrylate hydrogel", 2017 Stevenson Biomaterials Lecture and Research Poster Session, March 2017, Syracuse, New York.